TECHNISCHE
UNIVERSITÄT
MÜNCHEN

WALTHER - MEISSNER -
INSTITUT FÜR TIEF -
TEMPERATURFORSCHUNG

BAYERISCHE
AKADEMIE DER
WISSENSCHAFTEN

Inductively Coupled Nano-Electromechanics in Flux Tunable Superconducting Resonators

Masterarbeit von
Christoph Utschick

Supervisor: Priv.-Doz. Dr. Hans Hübl
München, April 10, 2018

Contents

Chapter 1

Introduction

The importance of sensing technologies on small length scales has just been demonstrated again, with the Nobel Prize winning detection of gravitational waves at the LIGO detector in the year 2016 [1]. This laser interferometer is able to detect a length change 10 000 times smaller than an atomic nucleus [2] and confirmed Albert Einstein's prediction of gravitational waves. Besides fundamental aspects, sensors of mechanical motion in general are sensitive to displacement and acceleration and are used in a variety of applications in every day life. Whereas in the automotive industry acceleration sensors activate protective airbags in the case of an accident [3], they are also implemented into modern hand-held electronic devices allowing a rotation of the screen when the device is turned upside down [4]. Commercial applications as well as scientific research have imposed demanding requirements onto the sensing technology regarding size and versatility. While for commercial devices low-cost and robustness are the main aspects, in science the focus lies on shrinking the sensors and hereby increasing their sensitivity, resulting in nanomechanical devices. Ultra high sensitivities with the ability of sensing single molecules or even atoms [5] have been demonstrated and mass sensors with yoctogramm resolution [6, 7] have enabled an entirely new way of mass spectroscopy. This increase in sensitivity has also paved the way towards new experiments on the quantum theory of macroscopic objects as e.g. levitating masses in cryogenic environments [8, 9].

The challenge of controlling the mechanical motion and reading out its state has led to the field of optomechanics where a nanomechanical resonator is integrated into an optical cavity. In such a cavity, one of the mirrors is free to vibrate and its displacement modifies the length of the cavity. Thus the mechanical degree of freedom is coupled to the light field of the cavity enabling a light-matter interaction [10]. When used appropriately, this interaction has two effects. On the one hand the radiation pressure in the cavity exerts a force onto the mechanical element, on the other hand the displacement changes the boundary conditions of the cavity and hence the resonance frequency [11]. This mutual interaction enables a plethora of experimental methods including optical measurements, amplification and cooling of mechanical motion [10]. The interaction mechanism is versatile and can be implemented in a variety of systems e.g. whispering gallery resonators [12], photonic crystals [13], suspended or levitated nano-objects [14] and electrical resonators [15]. The latter one transforms the optomechanical approach into an electrical circuit which gives rise to the field of electromechanics, where a mechanical

element is integrated into an LC-resonator. In analogy to optomechanics the displacement of the mechanical element is coupled to the inductance or the capacitance of the LC circuit. It changes the electrical length and hence the resonance frequency. With the use of superconducting microwave (MW) resonators we can enter the size and frequency regime of nanomechanical resonators [16].
The electromechanical devices considered in this thesis are realized with superconducting coplanar waveguides in the GHz regime and mechanical resonators in the MHz regime. When operated at mK temperatures, the electrical resonator is in the ground state and the mechanical element is in a thermal state. The interaction between electrical field and mechanical element provides the possibility of controlling and reading-out the mechanical motion at the quantum limit. Hereby the coupling strength is the quantum parameter of the system and one can resolve more and more quantum features as it grows [10]. Recently, ground state cooling [17, 18], preparation of squeezed states [19–21] and measurements with quantum limited precision [22] have been demonstrated. With the ability of cooling a macroscopic mechanical resonator into its ground state it may also be suitable for the storage of quantum information and could be operated as an interface between the optical and the microwave domain [23, 24]. Coherent state transfer onto a mechanical resonator has already been shown [25, 26]. As the phenomena mentioned above have all been demonstrated with capacitively coupled systems, current research focuses on realizing them also in an inductively coupled system. Although literature [27–29] predicts that it is possible and the coupling strength is even expected to exceed the capacitive counterpart, an experimental demonstration has not been achieved to date. Nevertheless recent results from Refs. [30, 31] are very promising. The micromechanical motion of an inductively coupled resonator has been detected with a displacement sensitivity of $10\,\mathrm{fm/Hz^{1/2}}$ by using a dc-SQUID in the voltage state as magnetic flux sensor. Integrating such a system into a MW resonator and operating it in the zero voltage state is expected to finally enable the fundamental light-matter interaction.
In this thesis we are going to present an inductive coupling mechanism between mechanical resonators and superconducting flux tunable MW resonators.
We start in Chapter 2 with a theoretical introduction to mechanical string-resonators as well as flux tunable microwave resonators. The fundamental coupling strength of the coupling scheme is derived and compared. Furthermore we analyse the magnetic flux noise in our system and define demands regarding the flux resolution of our SQUIDs. In Chapter 3 we present the sample layout and describe the fabrication procedure. In Chapter 4, we present experimental results starting with characterizations of the string-resonators, the SQUIDs and the microwave resonators. Last but not least, we show measurements on a hybrid device, with the aim to quantify the electromechanical interaction. We analyse and compare all results with the theoretic models introduced in Chapter 2. Finally we summarize the results and give an outlook about further steps and improvements that can be implemented in future experiments.

Chapter 2

Theoretical Description

In this chapter we introduce the theoretical concepts required to understand and describe electromechanical hybrid systems. We will introduce the theory of nanomechanical string-resonators and MW resonators based on coplanar wave guides, separately. In addition we will show that the integration of a direct current superconducting quantum interference devices (dc-SQUID) into a MW resonator realizes a flux tunable resonator (FTR).
Further, we introduce the basic ideas and concepts of electromechanical interaction and we discuss two possibilities of realizing the optomechanical coupling in our samples. We derive the fundamental coupling strength for both systems assuming experimentally feasible parameters and compare them. Finally we provide an analysis of the requirements regarding noise and sensitivity.

2.1 Mechanical String-Resonators

We start the theoretical description by analysing the mechanical motion of a doubly clamped highly tensile stressed nanomechanical string, considering the string as a one-dimensional damped harmonic oscillator. According to Refs. [32–35], the fundamental resonance frequency of such a string is given by:

$$\Omega_{\mathrm{m}} = \frac{\pi}{l}\sqrt{\frac{\sigma}{\rho}}\,, \tag{2.1}$$

with the density of the material ρ, the length of the string l and the tensile prestress σ. The length of the string is determined by the distance between the clamping points.

The equation of motion of the nanostring with an external driving force $F_0 \exp\left(-i\Omega t\right)$ and a damping force $-m_{\mathrm{eff}}\Gamma_{\mathrm{m}}\dot{x}$ is given by [36]

$$\ddot{x} + \Gamma_{\mathrm{m}}\dot{x} + \Omega_{\mathrm{m}}^2 x = \frac{F_0}{m_{\mathrm{eff}}}\exp\left(-i\Omega t\right)\,, \tag{2.2}$$

with the effective mass of a doubly clamped string $m_{\mathrm{eff}} = m/2$, where m is its total mass.
This differential equation can be solved with the ansatz $x(t) = x_0\exp(i\Omega t)$ yielding the absolute

amplitude of the strings motion at the vibrational antinode [36]

$$x(\Omega) = \frac{F_0/m_{\mathrm{eff}}}{\sqrt{(\Omega_{\mathrm{m}}^2 - \Omega^2)^2 + (\Gamma_{\mathrm{m}}\Omega)^2}} \approx x_0 \left| \frac{\Gamma_{\mathrm{m}}}{i\,(\Omega_{\mathrm{m}} - \Omega) + \frac{\Gamma_{\mathrm{m}}}{2}} \right| , \tag{2.3}$$

$$\text{with} \quad x_0 = \frac{F_0}{2m_{\mathrm{eff}}\Gamma_{\mathrm{m}}\Omega_{\mathrm{m}}} .$$

The approximation on the right hand side of Eq. (2.3) is valid for $\Gamma_{\mathrm{m}} \ll \Omega_{\mathrm{m}}$ which is typically well satisfied.

The quality factor of the mechanical resonator Q_{m} relates the energy stored in the mechanical motion to the energy loss during one oscillation and is therefore a measure for the amount of oscillations the undriven resonator performs before the amplitude becomes negligibly small. It is defined as [37]:

$$Q_{\mathrm{m}} = \frac{\Omega_{\mathrm{m}}}{\Gamma_{\mathrm{m}}} . \tag{2.4}$$

Although the damping rate Γ_{m} was defined in the equation of motion as amplitude damping rate, it can also be used for the definition of the Q-factor in terms of energy damping as shown in Ref. [37].

When thermalized in a bath of temperature T, the mechanical motion of the string-resonator corresponds to $\bar{n}_{\mathrm{m}}$ phonons:

$$\bar{n}_{\mathrm{m}} = \frac{k_{\mathrm{B}}T}{\hbar\Omega_{\mathrm{m}}} , \tag{2.5}$$

where k_{B} is the Boltzmann constant and $\hbar$ the Planck constant.

The root-mean-square (rms) displacement of the mechanical string-resonator in a thermal state, occupied with $\bar{n}_{\mathrm{m}}$ phonons is given by [38]:

$$\sqrt{\langle x^2 \rangle} = x_{\mathrm{zpf}} \sqrt{\langle \bar{n}_{\mathrm{m}} |\, (b^\dagger + b)^2 \,| \bar{n}_{\mathrm{m}} \rangle} = x_{\mathrm{zpf}} \cdot \sqrt{2\bar{n}_{\mathrm{m}} + 1} \tag{2.6}$$

with the zero point fluctuation [10]:

$$x_{\mathrm{zpf}} = \sqrt{\frac{\hbar}{2m_{\mathrm{eff}}\Omega_{\mathrm{m}}}} . \tag{2.7}$$

Please note that Eq. (2.3) is only valid for small displacements of the string as it does not consider a non-linear response. If the string is excited with higher drive powers the strong displacement starts to affect the effective length and hence the stress in the string. It enters a non-linear regime where the restoring force depends on the amplitude and according to Ref. [39] one has to add a cubic term to the equation of motion which introduces a duffing non-linearity. The effects on the response of the string-resonator are discussed in detail in Ref. [40, 41].

2.2 Microwave Resonators

In the following we are going to introduce the planar MW resonators which are used to confine electromagnetic waves. The basis of a MW resonator is a coplanar wave guide (CPW) of length

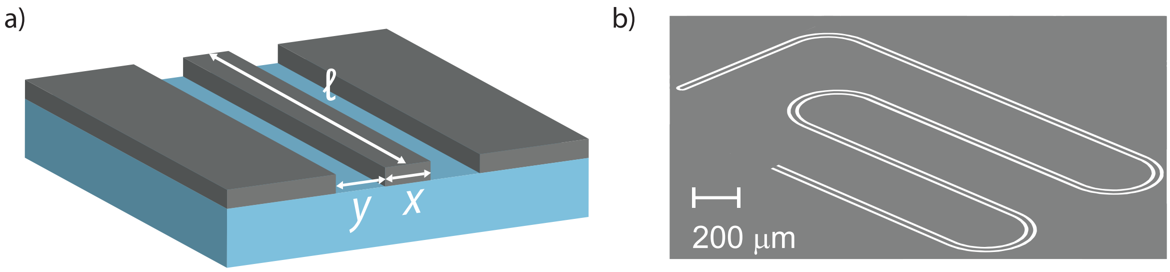

Figure 2.1: a) sketch of a coplanar wave guide on a silicon substrate. The central conductor of width x and length l is separated from the ground plane by a gap of width y. b) overview of a $\lambda/4$ MW resonator of length l_{r}.

l. It consists of a central conductor of width x which is separated from the ground plane by a gap of size y. A sketch of such a CPW together with the resulting MW resonator is depicted in Fig. 2.1. In an equivalent circuit picture a coplanar wave guide can be seen as an LC circuit with impedance $Z_0 = \sqrt{L_l/C_l}$ where L_l and C_l denote the inductance and capacitance per unit length of the wave guide [42]. They can be calculated by solving elliptic integrals as shown in Ref. [42]. By choosing appropriate parameters x and y we match the impedance of the wave guide [42] to $50\,\Omega$, being the standard of MW cables and electronics.
In such an LC-circuit, electromagnetic waves can oscillate at the characteristic frequency $\omega_{\mathrm{r}} = 1/\sqrt{LC}$, where L and C are the total inductance and capacitance respectively, creating a standing wave pattern. It is convenient to calculate the resonance frequency with an alternative formula based on the wavelength λ of the MW and the effective dielectric constant as given in Ref. [42]

$$\frac{\omega_{\mathrm{r}}}{2\pi} = \frac{c}{\lambda\sqrt{\epsilon_{\mathrm{eff}}}}\,, \tag{2.8}$$

where c is the speed of light in vacuum. The length of the MW resonator defines the boundary conditions of the standing wave with wavelength λ. Hence, the resonance frequency can be tailored by changing the length. For frequencies in the GHz regime this typically results in resonator lengths of a few cm, so it is useful to employ $\lambda/4$ resonators. In such a resonator the length is reduced to a quarter of the wavelength and one end is terminated to ground, satisfying the boundary condition of the fundamental mode which has a current anti-node at $\lambda/4$.
Here, excitations in the MW resonator are induced by coupling the resonator to a transmission line. We depict a capacitively coupled $\lambda/4$ resonator in Fig. 2.2. For comparison an equivalent circuit diagram and the actual structure are shown in panels a) and b). The coupling area and the termination to ground are indicated in green and blue respectively.
In analogy to mechanical resonators we define the electric quality factor

$$Q = \frac{\omega_{\mathrm{r}}}{\kappa}\,, \tag{2.9}$$

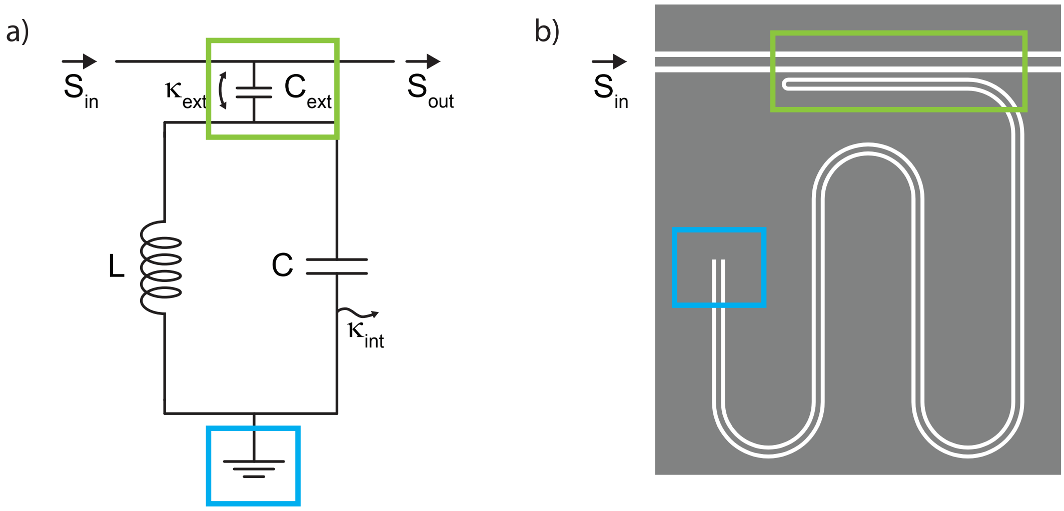

Figure 2.2: A $\lambda/4$ MW resonator coupled capacitively to a transmission line via coupling capacity C_{ext} and terminated to ground at the end. a) Equivalent LC circuit diagram and b) sketch of the actual structure. The coupling area and the termination to ground are indicated in green and blue respectively.

with κ the total energy loss rate which is the sum of internal and external losses: $\kappa = \kappa_{\text{int}} + \kappa_{\text{ext}}$. Internal losses are dominated by two-level state losses, quasiparticle losses and eddy current losses (cf. Ref. [43]). External losses depend on the coupling to the environment which can be tailored via the geometry of the coupling capacitor depicted in Fig. 2.2 b).
We write down analytic equations for both loss mechanisms [41]

$$\kappa_{\text{ext}} = \omega_{\text{r}}^2 Z_0 \frac{C_{\text{ext}}^2}{C} \quad \text{and} \quad \kappa_{\text{int}} = \frac{\alpha L_{\text{r}}}{Z_0 C}\,, \tag{2.10}$$

with C_{ext} the external coupling capacity and α the internal damping constant per length.
In cavity QED experiments one aims for the so-called overcoupled design of the resonator, i.e. $\kappa_{\text{ext}} > \kappa_{\text{int}}$. Hereby, the signal of interest being inside the resonator is dominantly emitted into the MW circuit to the detection electronics.

The power transmission spectrum of such a MW resonator is given by [41]

$$T(\omega) = 1 - \frac{(\kappa/2)^2 - (\kappa_{\text{int}}/2)^2}{(\omega - \omega_{\text{r}})^2 + (\kappa/2)^2}\,. \tag{2.11}$$

Under realistic experimental conditions, one observes besides the pure absorption of Eq. (2.11) undesired port-to-port transmission of MWs which can be modelled as complex background in addition to the expected Lorentzian lineshape [41]. Therefore a modified Lorentzian with complex background is introduced in Appendix B of Ref. [41], resulting in:

$$T^{\mathrm{meas}}(\omega) = 1 - \left| \frac{\sqrt{\kappa_{\mathrm{ext}}\kappa}/2}{\kappa/2 + i(\omega - \omega_{\mathrm{r}})} + ic_1 \right|^2 + c_2 \,. \tag{2.12}$$

We can fit Eq. (2.12) to experimental data and extract κ, κ_{int}, κ_{ext} and ω_{r}.
From an experimental point of view the power transmission is measured with a vector network analyser (VNA) by recording the complex scattering parameter S_{21}. The squared absolute value $|S_{21}|^2$ corresponds to the power transmission T. Details on the measurement method will be given in the experimental part of this thesis.
As mentioned above the aim of employing MW resonators is to study the interaction of electromagnetic waves and nanomechanical motion. In the quasi particle picture this interaction takes place between photons and phonons. In order to quantify the interaction it is necessary to know the number of photons trapped in the resonator. It depends on the drive power that is sent into the transmission line and on the strength of the external coupling [44]:

$$\bar{n}_{\mathrm{r}} = \frac{P_{\mathrm{d}}}{\hbar\omega_{\mathrm{d}}} \frac{\kappa_{\mathrm{ext}}/2}{(\kappa/2)^2 + \Delta^2} \,, \tag{2.13}$$

where P_{d} denotes the drive power at the sample input and ω_{d} the angular frequency of the drive tone. $\Delta = \omega_{\mathrm{d}} - \omega_{\mathrm{r}}$ is the detuning from the resonators resonance. P_{d} is related to the output power of the microwave source P_{source} which is typically given in decibel milliwatt by:

$$P_{\mathrm{d}}(\mathrm{mW}) = 10^{(P_{\mathrm{source}}(\mathrm{dBm}) - L_{\mathrm{p}}(\mathrm{dB}))/10} \,, \tag{2.14}$$

where L_{p} is the total signal attenuation between microwave source and sample in decibel.

2.3 Flux Tunable Microwave Resonators

In order to be able to tune the resonance frequency of the MW resonator we add a non-linear tunable inductance in form of a SQUID. In the following we first introduce the fundamental concepts of Josephson junctions and SQUIDs which belong to the field of Josephson Physics, then we describe flux tunable MW resonators.

Introduction to the Josephson Effect

The Josephson effect is a physical phenomenon based on the coherence of the superconducting state. Together with the phenomena of zero resistance, field screening and flux quantization [45, 46] it is one of the few examples where quantum effects manifest on macroscopic length scales. In the following we are going to describe the Josephson effect briefly, based on a detailed treatment that can be found in Ref. [47].

A Single Josephson Junction

A Josephson junction consists of two superconducting materials that are separated from each other by a thin insulating barrier. In the superconducting state conduction electrons around the Fermi edge condense into a phase-locked state and can be described by a single macroscopic wave function Ψ [47]. From this follows, that on both sides of the tunnel barrier macroscopic wave functions develop with a gauge invariant phase difference φ to each other. The overlap of the wavefunctions enables tunnelling of cooper pair electrons through the barrier which results in a tunnelling or Josephson current. This current across the barrier depends on φ and is described by the first Josephson equation, the current-phase relation [47]

$$I = I_\mathrm{c} \sin\varphi \,. \tag{2.15}$$

Here, I_c is the critical Josephson current which is determined by the coupling strength between the junction electrodes. In this thesis I_c is controlled via the Josephson junction area and the thickness of the tunnel barrier.
Similar to equation (2.15) one can also derive a voltage-phase relation by considering the time derivative of φ resulting in the second Josephson equation [47]

$$\frac{d\varphi}{dt} = \frac{2\pi}{\Phi_0} V \tag{2.16}$$

with the flux quantum $\Phi_0 = h/2e$.
From both Josephson equations we derive the Josephson inductance L_J of a Josephson junction

$$L_\mathrm{J} = \frac{V}{dI/dt} = \frac{\Phi_0}{2\pi I_\mathrm{c}\cos\varphi} \,. \tag{2.17}$$

The charging energy of a single electron on the Josephson junction E_C is given by [47]

$$E_\mathrm{C} = \frac{e^2}{2C} \,, \tag{2.18}$$

where C is the capacitance of the junction.
The overlap of macroscopic wave functions does not only enable tunnelling, it also causes a finite binding energy stored in the junction which is called Josephson coupling energy [47]

$$E_\mathrm{J} = \frac{\Phi_0 I_\mathrm{c}}{2\pi}\left(1-\cos\varphi\right) = E_\mathrm{J0}\left(1-\cos\varphi\right) \,. \tag{2.19}$$

This coupling energy is derived by integrating over the energy which is required to increase the current from zero to a finite current state. The stored energy can be understood as kinetic energy of the moving superelectrons [47]. Furthermore, the potential energy of the Josephson junction is given by Ref. [47]

$$E_\mathrm{pot}(\varphi) = E_\mathrm{J0}\left(1-\cos\varphi - \frac{I}{I_\mathrm{c}}\varphi\right) + c \,. \tag{2.20}$$

We plot the potential energy according to Eq. (2.20) as a function of φ in Fig. 2.3. It has

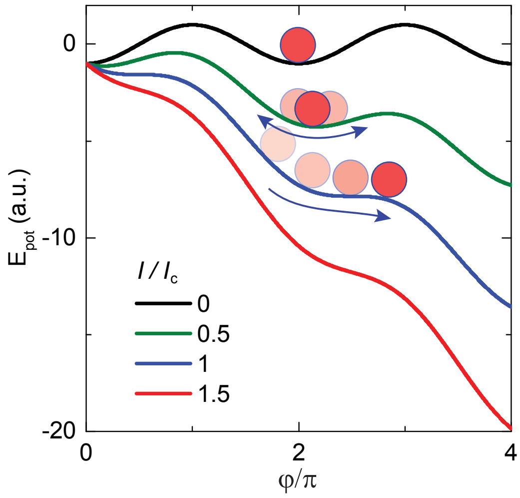

Figure 2.3: Potential energy of a Josephson junction. The state of the junction is compared to a classical particle in the potential landscape. The slope of the washboard potential depends on the current which flows through the junction. For $I = I_c$ the local minima in the potential vanish and the particle moves down the tilted potential. Further explanation is given in the main text. Figure taken from Ref. [40].

the shape of a tilted washboard and explains the dynamics of Josephson junctions. In this picture the state of the junction is compared to a classical particle. For $I < I_c$ the potential has minima at discrete phase values φ_n in which the particle is trapped, thus φ is constant in time. According to Eq. 2.16 the voltage across the junction in this state is zero. With increasing current the tilt of the washboard potential increases. For $I > I_c$ the local minima vanish and the particle moves down the tilted potential, resulting in a constant phase slip and a voltage drop across the junction. The junction is then in the voltage state with an ohmic resistance [47]. By decreasing the current through the junction the tilt of the potential decreases and the system is retrapped in a pure superconducting state as soon as the particle comes to rest in a minimum. The amount of damping is defined by the Stewart-McCumber parameter [47, 48]:

$$\beta_c = \frac{2\pi I_c R_n^2 C}{\Phi_0} = \left(2 - (\pi - 2)\frac{I_r}{I_c}\right)\left(\frac{I_c}{I_r}\right)^2 , \tag{2.21}$$

with R_n the resistance in the normal conducting state, C the capacitance of the Josephson junction and I_r the retrapping current in IU-characteristics. The right part of the equation is valid for $0.05 < I_r/I_c < 0.95$ [48]. For $\beta \gg 1$ the junction is weakly damped, for $\beta \ll 1$ the junction is strongly damped. We will use Eq. (2.21) in Sec. 4.2 to calculate the capacitance of our Josephson junctions and estimate the thickness of the insulating layer by considering the junction as a plate capacitor. In our experiments the junctions are operated solely in the zero voltage state, so the damping parameter is not significant for their performance.
To sum up, Josephson junctions can be described by an equivalent circuit diagram including a capacitive-, a resistive- and a supercurrent. It is depicted in Fig. 2.4.

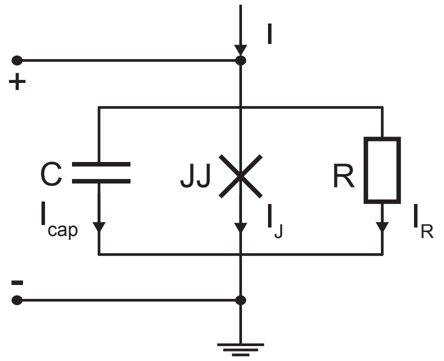

Figure 2.4: Equivalent circuit diagram of a Josephson junction including a capacitive-, a resistive- and a supercurrent. The Josephson junction is indicated by a diagonal cross

Superconducting Quantum Interference Devices

If two Josephson junctions are connected by a superconducting loop their macroscopic wavefunctions overlap and create quantum interference. In general such devices are called superconducting quantum interference devices (SQUIDs). One can connect the junctions in rf- or dc-configuration. In this thesis we consider solely the latter ones using the abbreviation SQUID. A circuit diagram of a SQUID is depicted in Fig. 2.5.

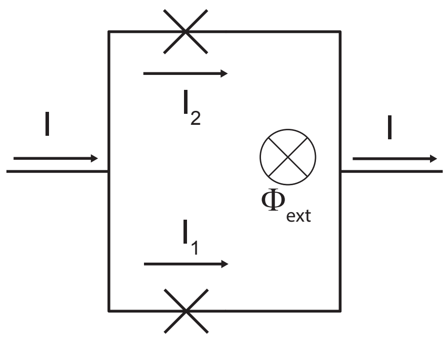

Figure 2.5: Circuit diagram of a SQUID including two Josephson junctions which are connected in a superconducting loop. A dc-current flows through the loop from the left to right hand side. Φ_{ext} describes the magnetic flux passing through the loop.

One can derive that the gauge invariant phase differences φ_1 and φ_2 are coupled to each other in order to guarantee total flux quantization in the loop [47].

$$\varphi_2 - \varphi_1 = \frac{2\pi\Phi}{\Phi_0}\,, \tag{2.22}$$

with Φ being the total magnetic flux passing through the loop. For the moment, we want to assume that $\Phi = \Phi_{\mathrm{ext}}$, exceptions are discussed later.

With Kirchhoff's law we write the supercurrent through the loop as:

$$I = I_1 + I_2 = I_{c,1} \sin\varphi_1 + I_{c,2} \sin\varphi_2\,, \tag{2.23}$$

with $I_{c,i}$ the critical currents of the Josephson junctions.
In general, the junctions are not identical resulting in $I_{c,1} \neq I_{c,2}$. According to the approaches made in Ref. [28] we define an average critical current $I_{c,0} = (I_{c,1} + I_{c,2})/2$ and an asymmetry parameter $\alpha_I = (I_{c,2} - I_{c,1})\,/\,(2I_{c,0})$ such that $I_{c,1} = I_{c,0}(1 - \alpha_I)$ and $I_{c,2} = I_{c,0}(1 + \alpha_I)$.
We spilt Eq. (2.23) into two terms, where the first one equals two symmetric junctions and the second one accounts for the asymmetry [28]:

$$I = I_{c,0}\left[(\sin\varphi_1 + \sin\varphi_2) + \alpha_I\,(\sin\varphi_1 - \sin\varphi_2)\right]. \tag{2.24}$$

With $\varphi_- = (\varphi_2 - \varphi_1)/2$ and $\varphi_+ = (\varphi_2 + \varphi_1)/2$ one can write Eq. (2.24) as:

$$I = 2I_{c,0}\left[(\cos\varphi_- \sin\varphi_+) - \alpha_I\,(\sin\varphi_- \cos\varphi_+)\right] \tag{2.25}$$

As shown in Ref. [28] one can use Eq. (2.25) to define the critical current of the asymmetric SQUID by shifting φ_+ by a phase φ_0 which satisfies $\tan(\varphi_0) = \alpha_I \tan(\varphi_-)$.
The resulting critical current through the SQUID is flux dependent and reads [28]:

$$I_s^m(\Phi_{ext}) = 2I_{c,0}\sqrt{\cos^2\left(\pi\frac{\Phi_{ext}}{\Phi_0}\right) + \alpha_I^2 \sin^2\left(\pi\frac{\Phi_{ext}}{\Phi_0}\right)}\,. \tag{2.26}$$

In the symmetric case α_I is zero and the equation simplifies to:

$$I_s^m(\Phi_{ext}) = 2I_c\left|\cos\left(\pi\frac{\Phi_{ext}}{\Phi_0}\right)\right|\,. \tag{2.27}$$

In Fig. 2.6 we plot the maximum supercurrent over external flux according to Eq. (2.26) for different values of α_I. We see that in the symmetric case the maximum current varies between 0 and $2I_{c,0}$. In the asymmetric case the minimum does not reach zero. The modulation depth is reduced to $2I_{c,0}\,(1 - \alpha_I)$.
Next, we want to derive the Josephson inductance of the SQUID. Therefore we add up the inductances of both parallel shunted Josephson junctions:

$$\frac{1}{L_{JJ}} = \frac{1}{L_{J,1}} + \frac{1}{L_{J,2}} = \frac{2\pi}{\Phi_0}\left(I_{c,1}\cos\varphi_1 + I_{c,2}\cos\varphi_2\right). \tag{2.28}$$

Again we rewrite this equation in the general case of $I_{c,1} \neq I_{c,2}$ to:

$$L_{JJ}(\Phi_{ext}) = \frac{\Phi_0}{4\pi I_{c,0}\sqrt{\cos^2\left(\frac{\pi\Phi_{ext}}{\Phi_0}\right) + \alpha_I^2\sin^2\left(\frac{\pi\Phi_{ext}}{\Phi_0}\right)}} = \frac{\Phi_0}{2\pi I_s^m(\Phi_{ext})}\,. \tag{2.29}$$

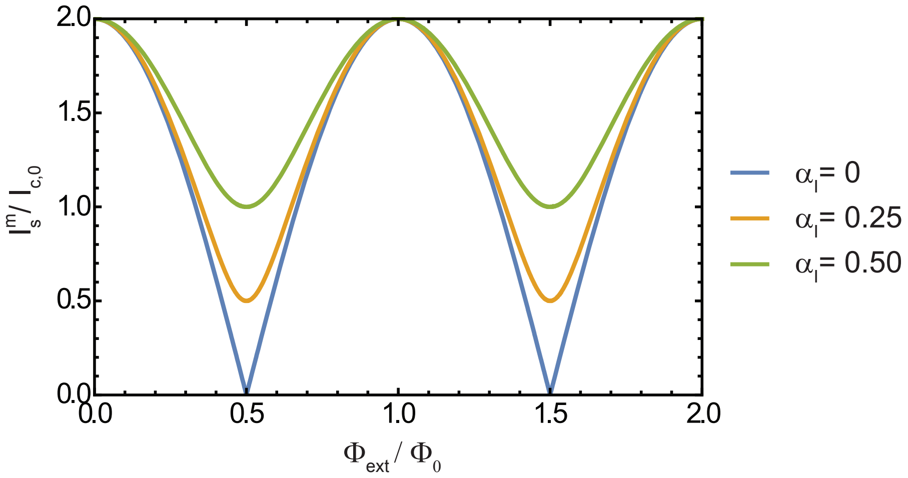

Figure 2.6: Flux dependence of the maximum supercurrent I_s^m through a SQUID for different values of the asymmetry parameter α_I according to Eq. (2.26)

For the symmetric case the Josephson inductance simplifies to [47]:

$$L_\mathrm{JJ}(\Phi_\mathrm{ext}) = \frac{\Phi_0}{4\pi I_\mathrm{c} \left|\cos\left(\pi \frac{\Phi_\mathrm{ext}}{\Phi_0}\right)\right|} \,. \tag{2.30}$$

In the above considerations we have assumed that the magnetic flux passing through the SQUID loop equals the externally applied flux. Now we want to discuss under which conditions this assumption is justified. Due to circulating currents $I_\mathrm{circ} = I_1 - I_2$ in the SQUID loop, additional flux $\Phi_\mathrm{L} = LI_\mathrm{circ}$ can be generated. The phases φ_1 and φ_2 then have to be solved self consistently for both, the dc-current and the circulating current.
We introduce the screening parameter β_L which compares the self induced magnetic flux to the magnetic flux quantum [47]:

$$\beta_L = \frac{2L_\mathrm{loop}I_\mathrm{c}}{\Phi_0} \,, \tag{2.31}$$

where L_loop is the inductance of the SQUID loop which consists of geometric and kinetic contributions.
According to Ref. [49], the kinetic inductance of a straight wire of length l_string, width w_string and thickness t_string is given by:

$$L_\mathrm{loop}^\mathrm{kin} = \mu_0 \lambda_\mathrm{L}^2 \frac{l_\mathrm{string}}{t_\mathrm{string} \cdot w_\mathrm{string}} \,, \tag{2.32}$$

where $\lambda_\mathrm{L} = 200\,\mathrm{nm}$ [50] is the London penetration depth for thin film aluminium and μ_0 the permeability constant of vacuum. The value of λ_L has been calculated by transforming Eq. (2.32) to $\lambda_\mathrm{L} = ((L_\mathrm{loop}^\mathrm{kin} \cdot t_\mathrm{string} \cdot w_\mathrm{string}/(l_\mathrm{string} \cdot \mu_0))^{1/2}$ and inserting values given in Ref. [50].
We see that the kinetic inductance is proportional to the length of the wire and inverse

proportional to its cross section.
According to Refs. [51, 52], the geometric inductance of a rectangular SQUID loop of length l_{loop}, width w_{loop}, loop diagonal $g_{\text{loop}} = (w_{\text{loop}}^2 + l_{\text{loop}}^2)^{1/2}$ and wire diameter d is given by:

$$\begin{aligned} L_{\text{loop}}^{\text{geom}} = \Big[& 0.4 \left((l+w)\log\left(4\frac{lw}{d}\right) - l\log(l+g) - w\log(w+g) \right) \\ & +0.4\,(2g + d - 2(l+w)) \Big] \cdot 10^{-6} \,. \end{aligned} \tag{2.33}$$

For reasons of simplicity we have excluded the indices in Eq. (2.33).
The total loop inductance is [50]:

$$L_{\text{loop}} = L_{\text{loop}}^{\text{geom}} + L_{\text{loop}}^{\text{kin}} \tag{2.34}$$

For $\beta_{\text{L}} \ll 1$ we neglect circulating currents in the SQUID loop and the derivations of Eqs. (2.26) and (2.29) are valid. In order to be in this regime we need small self inductance L_{loop} and a small critical current I_{c}. In section 2.5 however we will see that maximizing the electromechanical coupling strength, requires to maximize both I_{c} and L. This conflict poses a delicate optimisation problem which results in a finite $0 < \beta_{\text{L}} < 1$. Optimal parameters will be discussed in Sec 2.5. For $\beta > 1$, one observes a reduction of the modulation depth of the critical current. We will discuss the consequences of finite β_{L} on the performance of flux tunable resonators in the next section and want to emphasise here, that β_{L} is the most important parameter in the SQUID design. Additionally it has been discussed in Ref. [53] that the effects of β_{L} can also occur for $\beta_{\text{L}} \lessapprox 1$, so we aim for values significantly smaller than 1.

To sum up we have seen that the maximum supercurrent through the SQUID modulates with externally applied magnetic flux. An asymmetry in the SQUID geometry as well as a high β_{L} parameter reduce the modulation depth. The Josephson inductance L_{JJ} is inverse proportional to the critical current I_{c}.

Flux Tunable MW Resonators

Having derived the SQUID equations, we can now theoretically describe flux tunable MW resonators (FTR). Due to the influence of the SQUID inductance, which itself is tunable by applying external flux, the resonance frequency ω_{r} of the MW resonator becomes flux dependent and thus tunable.
We depict a capacitively coupled MW resonator with embedded SQUID at the current anti-node in Fig. 2.7. An equivalent circuit diagram and a sketch of the actual structure including a zoom into the SQUID are shown in panels a) and b). The inductances L_{r} and L_{sq} of the bare MW resonator and the SQUID, both contribute to the total inductance of the LC circuit. When calculating the total inductance one has to consider that the MW resonator is a distributed circuit element and the SQUID is a lumped circuit element. Meaning that the inductance of the MW resonator is distributed continuously throughout the coplanar waveguide. In Ref. [54] the effective Lagrangian of the FTR is calculated by representing the MW resonator as a chain of

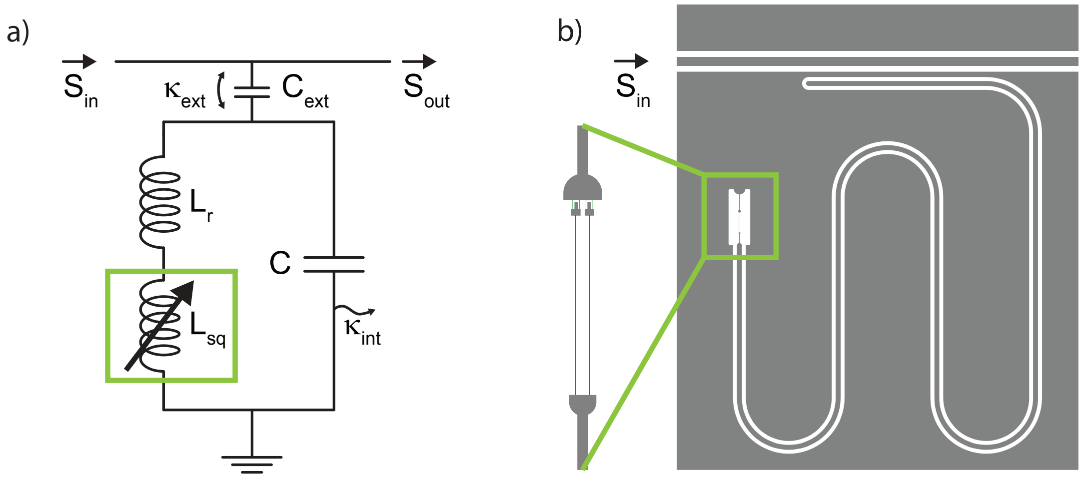

Figure 2.7: A capacitively coupled MW resonator with embedded SQUID at the current anti-node. The inductances L_r and L_sq of the bare MW resonator and the SQUID both contribute to the total inductance of the LC circuit. a) Equivalent circuit diagram and b) sketch of the actual structure including a zoom into the SQUID.

LC resonators. From the Lagrangian the wavelength dependent capacitance and inductance as well as the resonance frequency are derived. The latter one is a transcendental characteristic equation which can be Taylor expanded as shown in Ref. [55].
The resonance frequency of the FTR then reads [55]:

$$\omega_\mathrm{r}(\Phi_\mathrm{ext}) = \frac{\omega_\mathrm{r}^0}{1 + \frac{L_\mathrm{sq}(\Phi_\mathrm{ext})}{L_\mathrm{r}}}\,, \tag{2.35}$$

with ω_r^0, the resonance frequency of the bare MW resonator and $L_\mathrm{sq}(\Phi_\mathrm{ext}) = L_\mathrm{JJ}(\Phi_\mathrm{ext}) + L_\mathrm{loop}$ the total inductance of the SQUID.
We note that in Refs. [54, 55] only the Josephson inductance L_JJ of the SQUID is taken into account. In this thesis however, the SQUIDs do have very thin loop arms and the contribution of the kinetic inductance can be significant. We therefore add a general inductance L_loop which accounts for the geometric and kinetic inductance of the SQUID loop. In Fig. 2.8 we plot the tuneability of the MW resonator frequency as a function of the externally applied flux according to Eq. (2.35) assuming a typical value of $L_\mathrm{r} = 1\,\mathrm{nH}$ for different critical currents I_c and loop inductances L_loop in panels a) and b) respectively.
As one can see, the resonance frequency ω_r tunes down periodically for flux values of multiples of the half-integer flux quantum and takes its maximum value for multiples of the integer flux quantum. The maximum of ω_r is shifted to lower values compared to the bare MW resonator ($\omega_\mathrm{r}(0) < \omega_\mathrm{r}^0$).

$$\omega_\mathrm{r}(0) = \frac{\omega_\mathrm{r}^0}{1 + \left(\frac{\Phi_0}{4\pi I_{\mathrm{c},0}} + L_\mathrm{loop}\right)/L_\mathrm{r}}\,. \tag{2.36}$$

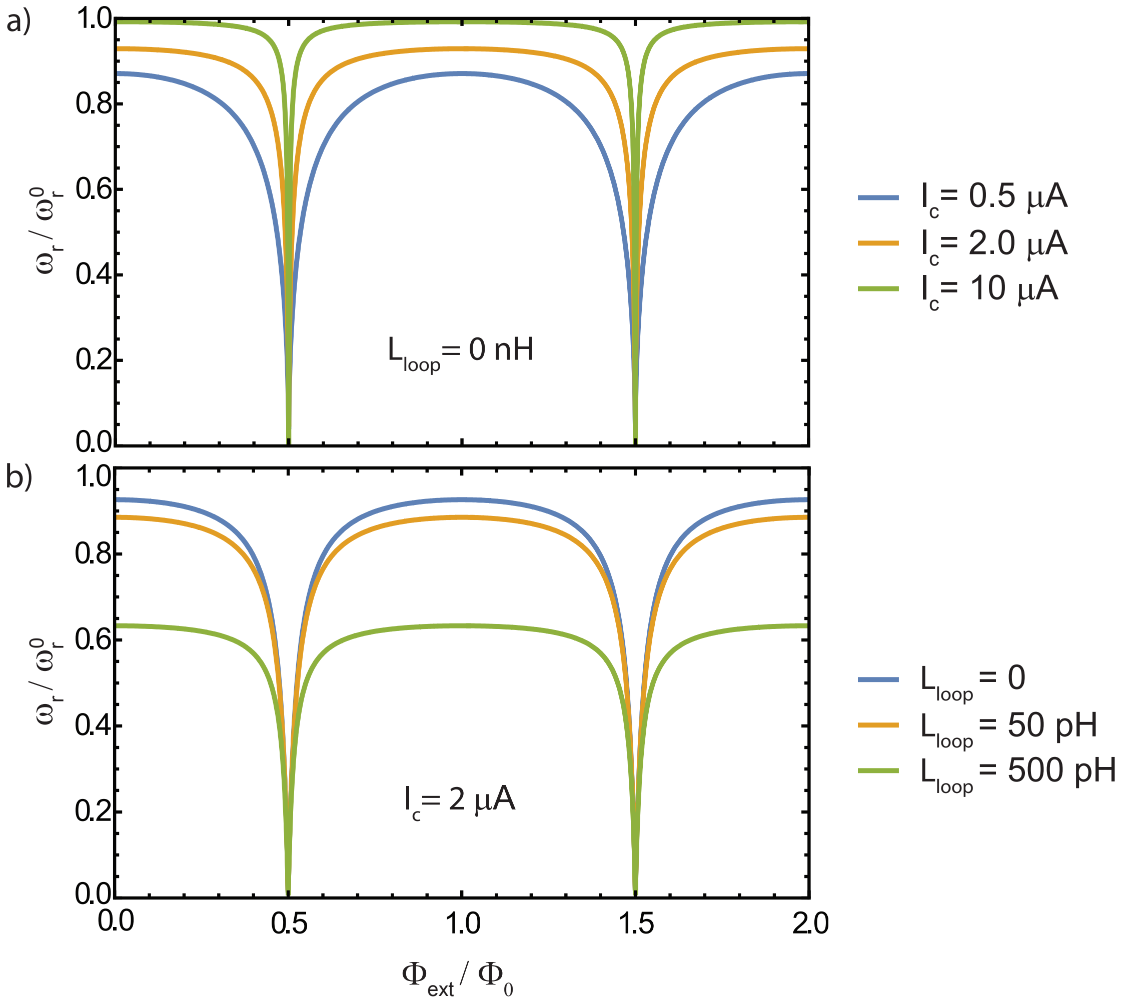

Figure 2.8: Flux tunability of a MW resonator with a symmetric SQUID embedded at the current antinode. The maximum resonance frequency is shifted to lower values compared to the bare MW resonator due to the influence of the SQUIDs inductance ($\omega_r/\omega_r^0 < 1$). The resonance frequency tunes down periodically for externally applied flux values of the half-integer flux quantum. Eq. (2.35) is evaluated for a) different values of I_c with fixed $L_{loop} = 0$ and b) different values of L_{loop} with fixed $I_c = 2\,\mu A$. While the critical current defines the shape of the curve and the frequency shift, the loop inductance only causes a frequency shift. For higher I_c, the down tuning is narrower and steeper.

The loop inductance L_{loop} causes an additional frequency shift without changing the shape of the curve significantly.
By solving this equation for I_c one can extract the averaged critical current of the Josephson junctions from transmission measurements, assuming that one knows ω_r^0, the resonance frequency without SQUID:

$$I_{c,0} = \left(\frac{4\pi}{\Phi_0}\left(L_r\left(\frac{\omega_r^0}{\omega_r(0)} - 1\right) - L_{loop}\right)\right)^{-1} \tag{2.37}$$

In Fig. 2.6 we have seen that an asymmetry in the SQUID geometry reduces the modulation depth of the maximum critical current. The Josephson inductance and following the modulation of the FTR frequency are influenced by this asymmetry as well.
In the symmetric case the Josephson inductance diverges at the half integer flux quantum and ω_r tunes to zero, in the asymmetric case the Josephson inductance does not diverge. The modulation depth is then given by:

$$\Delta\omega_\mathrm{r} = \omega_\mathrm{r}(0) - \omega_\mathrm{r}(\Phi_0/2) = \omega_\mathrm{r}(0)\left(1 - \frac{\omega_\mathrm{r}(\Phi_0/2)}{\omega_\mathrm{r}(0)}\right) , \tag{2.38}$$

By inserting Eq. (2.35) into Eq. (2.38) we find:

$$\frac{\Delta\omega_\mathrm{r}}{\omega_\mathrm{r}(0)} = \left(1 - \frac{1 + \frac{L_\mathrm{sq}(0)}{L_\mathrm{r}}}{1 + \frac{L_\mathrm{sq}(\Phi_0/2)}{L_\mathrm{r}}}\right) = \left(1 - \frac{L_\mathrm{r} + L_\mathrm{loop} + L_\mathrm{JJ}(0)}{L_\mathrm{r} + L_\mathrm{loop} + \frac{L_\mathrm{JJ}(0)}{\alpha_\mathrm{I}}}\right) , \tag{2.39}$$

with $L_\mathrm{JJ}(0) = \Phi_0/(4\pi I_\mathrm{c,0})$.
We plot the relative modulation depth as a function of the SQUID asymmetry for different critical currents and different loop inductances in Fig. 2.9. We see that the impact of the

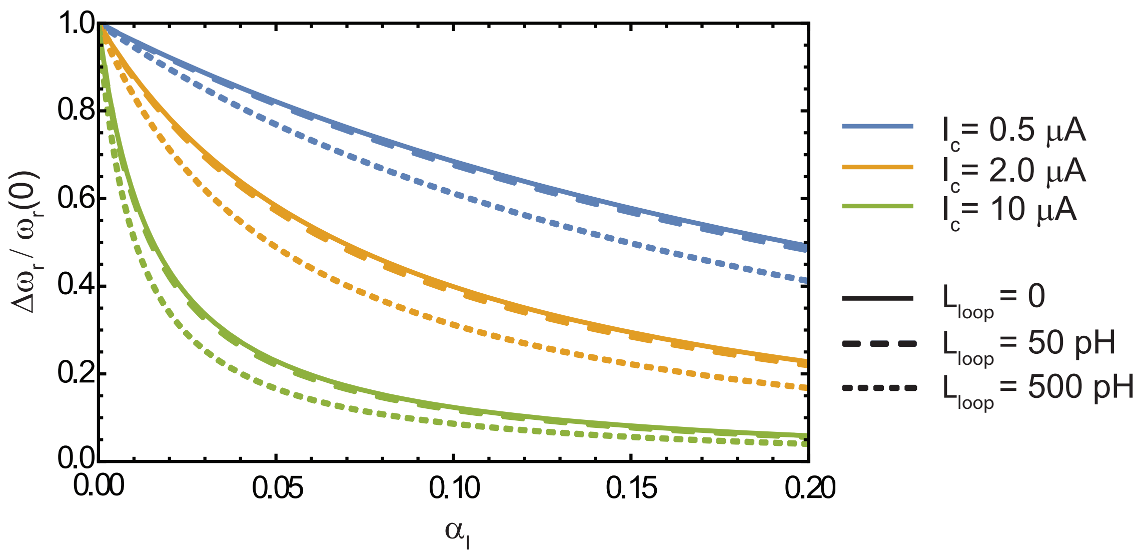

Figure 2.9: Relative modulation depth $\Delta\omega_\mathrm{r}/\omega_\mathrm{r}(0)$ of the FTR with $L_\mathrm{r} = 1\,\mathrm{nH}$ as a function of the asymmetry parameter α_I for different values of the critical current I_c (blue, orange, green) and different loop inductances L_loop (solid, dashed, dotted). If the Josephson junctions in the SQUID are asymmetric, the frequency modulation of the FTR is strongly reduced. For SQUIDs with large critical currents the impact of the asymmetry is stronger.

SQUID asymmetry on the modulation depth scales strongly with I_c. The loop inductance adds only a small correction. For large critical currents the Josephson inductance becomes small and the modulation of ω_r is suppressed even for small asymmetries ($\alpha_\mathrm{I} \ll 1$). Additionally, $\beta_\mathrm{L} = 2I_\mathrm{c,0}L/\Phi_0$ scales with I_c and flux jumps due to screening currents can occur if β_L is close to 1. In this case the full modulation depth can not be used. In order to maintain the flux tunability of the MW resonator we take care that $I_{c,0}$ and α_I are sufficiently low.

As side note we want to mention that the change of resonance frequency ω_r as a function of external flux can be considered as an effective change of the resonator length. By tuning the frequency to zero the electrical length of the resonator becomes infinitely long.
When the external flux is changed rapidly, the boundaries of the resonator move very fast, reaching a substantial fraction of the speed of light [56]. Thus they can be considered as relativistic mirrors.
The so called dynamical casimir effect predicts that such a fastly moving boundary condition can convert virtual photons into real observable ones. Virtual photons are particles that pop in and out of existence due to small fluctuations of energy at a given position in vacuum space following the uncertainty rules of Heisenberg [57]. Indeed Ref. [58] showed the creation of photons from vacuum fluctuations with a superconducting FTR.
The devices fabricated in this thesis are able to exploit the same effects since they are similar to the ones discussed in the references mentioned above. This means, the FTR could be used as photon source by operating it as a parametric amplifier [29]. Such a parametric interaction creates a squeezed resonator mode and enables control of the photon spectrum [29] which enhances the electromechanical coupling and improves the measurement noise [59].

2.4 Fundamental Concepts of Electromechanical Interaction

Having introduced mechanical string-resonators and flux tunable MW resonators, we can now discuss the fundamental concepts of the coupling mechanism between both elements. Most of the basic ideas have been adapted from the field of optomechanics. A detailed review of this field can be found in Ref. [60]. In the following we are going to present the basic relations and methods and consider two possibilities how to realize them in a hybrid sample.
Let us begin with a resonator for electromagnetic waves that is coupled to a mechanical element. The electrical length and consequently the resonance frequency of the FTR depends on the displacement of the mechanical element.
We start with the generic Hamiltonian of the system [10]:

$$\mathcal{H} = \hbar\omega_r(x)\left(a^\dagger a + \frac{1}{2}\right) + \hbar\Omega_m\left(b^\dagger b + \frac{1}{2}\right), \tag{2.40}$$

with a, $a^\dagger$ and b, $b^\dagger$ the ladder operators of the MW resonator and the mechanical string-resonator respectively.
The displacement of the mechanical resonator can be written as [10]:

$$x = x_{zpf}(b^\dagger + b), \tag{2.41}$$

with the zero point fluctuation [10]:

$$x_{\mathrm{zpf}} = \sqrt{\frac{\hbar}{2m_{\mathrm{eff}}\Omega_{\mathrm{m}}}}\,. \tag{2.42}$$

As the displacement of the mechanical resonator is small we can Taylor-expand $\omega_{\mathrm{r}}(x)$ around $x = 0$ to first order:

$$\omega_{\mathrm{r}}(x) \approx \omega_{\mathrm{r}}(0) + \frac{d\omega_{\mathrm{r}}}{dx}x\,. \tag{2.43}$$

We insert Eq. (2.43) into Eq. (2.40), define the coupling parameter $G = d\omega_{\mathrm{r}}/dx$ and simplify the Hamiltonian:

$$\mathcal{H} = \hbar\omega_{\mathrm{r}}(0)\left(a^\dagger a + \frac{1}{2}\right) + \hbar\Omega_{\mathrm{m}}\left(b^\dagger b + \frac{1}{2}\right) + \hbar G x_{\mathrm{zpf}}\left(a^\dagger a + \frac{1}{2}\right)\left(b^\dagger + b\right)\,, \tag{2.44}$$

The vacuum coupling rate $g_0 = Gx_{\mathrm{zpf}}$ defines the strength of the interaction between a single photon and a single phonon. The total electromechanical coupling strength g scales with the square root of the average number of photons in the MW resonator [60]:

$$g = g_0\sqrt{\bar{n}_{\mathrm{r}}}\,. \tag{2.45}$$

A coupled system as described above, allows to apply a wide range of experimental methods [60]. In the following we introduce the concepts of single tone and two-tone spectroscopy.

2.4.1 Single Tone Spectroscopy

One way of observing electromechanic interaction is to apply a drive tone on resonance ($\omega_{\mathrm{d}} = \omega_{\mathrm{r}}$). The inserted drive photons interact with the mechanical string-resonator and are up (down) converted to photons with higher (lower) energy by annihilation (creation) of a mechanical phonon. The scattered photons appear in the transmission spectrum as anti-Stokes (Stokes) sideband peaks at $+\Omega_{\mathrm{m}}$ ($-\Omega_{\mathrm{m}}$), as depicted schematically in Fig. 2.10.

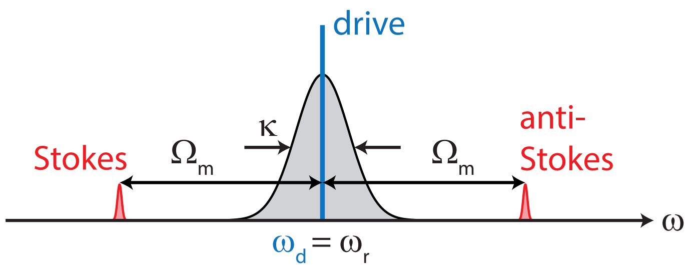

Figure 2.10: Schematic of Stokes and anti-Stokes sidebands for an undetuned drive tone. The probabilities for up and down conversion are equal, thus the total phonon number is preserved and the mechanical state is not affected by the measurement. Picture taken from Ref. [41].

In a more hand waving picture, the motion of the mechanical string-resonator results in a fluctuation of the FTRs resonance frequency which can be detected as downconverted sideband

peaks.
The detected power spectrum of the sideband peaks is proportional to the frequency fluctuation spectrum and allows direct measurement of the coupling strength [10]. Nevertheless one has to consider that the resulting coupling strength has to be calibrated by determining the transfer function $K(\omega)$ which depends on the actual setup, including all losses and amplifications in the MW lines as well as the effects of the down conversion of the MW signal.
The transfer function can be determined experimentally by applying the frequency noise calibration technique which is described for example in Ref. [61]. One injects an additional MW tone at $\Omega_{\mathrm{mod}} \approx \Omega_{\mathrm{m}}$ with a known frequency modulation depth of $\pm\Omega_{\mathrm{dev}}$ which results in additional sideband peaks close to the stokes and anti-stokes peaks depicted in Fig. 2.10. With this additional sideband peak one can calibrate the coupling strength using the following relation [41]:

$$g_0^2 = \frac{\Omega_{\mathrm{dev}}^2 \Gamma_{\mathrm{m}}}{16\bar{n}_{\mathrm{m}} \mathrm{ENBW}} \frac{S_{\mathrm{PP}}(\Omega_{\mathrm{m}})}{S_{\mathrm{PP}}^{\mathrm{mod}}}\,, \tag{2.46}$$

with Γ_{m} the linewidth of the mechanical string-resonator, $\bar{n}_{\mathrm{m}}$ the average number of thermally excited phonons, ENBW the detection bandwidth of the spectrum analyser and $S_{\mathrm{PP}}(\Omega_{\mathrm{m}})/S_{\mathrm{PP}}^{\mathrm{mod}}$ the relation of the amplitudes of the sideband peaks in the measured power spectrum.

The challenge one has to face when performing single tone spectroscopy is, that the linewidth of the sideband peak is in the order of a few Hz, while the frequency range in which it can be situated is in the order of MHz. Finding the sideband peak typically requires long measurement times and precise knowledge of Ω_{m} is crucial.

2.4.2 Two-Tone Spectroscopy

Another way of observing electromechanic interaction is to apply two MW tones to the FTR: a strong drive tone and a weak probe tone. In this case, the drive tone is applied with a detuning $\Delta = \pm\Omega_{\mathrm{m}}$ from the resonance frequency of the FTR. For positive (negative) detuning the injected photons have higher (lower) energy than the photons in the resonator. Due to scattering processes with the mechanics, the injected photons can be down (up) converted to resonator photons at ω_{r} [10]. If the condition of the resolved sideband $\Omega_{\mathrm{m}} > \kappa$ is given, then a drivetone at $\Delta = +\Omega_{\mathrm{m}}$ ($\Delta = -\Omega_{\mathrm{m}}$) results in an effective increase (decrease) of phonons and amplification (cooling) of the mechanical motion. We depict the schematics for a perfectly detuned drive tone in Fig. 2.11.
The weak probe tone is applied from a vector network analyser recording the power transmission in a frequency sweep around ω_{r}. Without a drive tone the normal transmission spectrum of the FTR according to Eq. (2.12) would be observed. With the drive tone present, however, drive photons which have been up (down) converted by the mechanics are also present in the FTR and interfere with the probe tone. Depending on the detuning of the drive tone and the sample geometry the interference is either constructive or destructive resulting in an enhanced or reduced transmission of the probe tone.
In other words, one observes an additional peak or dip inside of the resonance dip of the FTR.

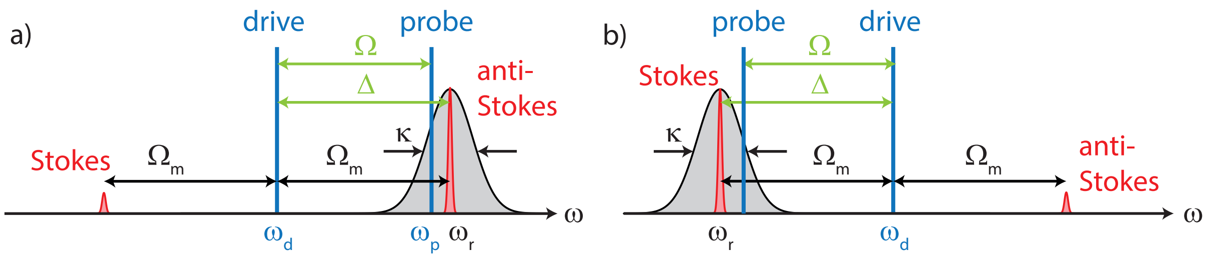

Figure 2.11: Schematic of Stokes and anti-Stokes sidebands for a perfectly detuned drive tone in the a) red sideband regime and b) blue sideband regime. The interaction process is described in the main text. In green, we define the detunings Δ and Ω used in Eq. (2.47) and (2.48). Picture taken from Ref. [41].

These features are called electromechanically induced transparency (EMIT) and electromechanically induced absorption (EMIA).
The resulting modified power transmission in the blue and red sideband regime can be described by Eqs. (2.47) and (2.48) respectively [44, 62]:

$$T = |S_{21}|^2 = \left| 1 - \frac{\kappa_{\mathrm{ex}/2}}{-i(\Delta + \Omega) + \kappa/2 + \frac{g_0^2 \bar{n}_{\mathrm{r}}}{-i(\Omega - \Omega_{\mathrm{m}}) + \Gamma_{\mathrm{m}}/2}} \right|^2, \tag{2.47}$$

$$T = |S_{21}|^2 = \left| 1 - \frac{\kappa_{\mathrm{ex}/2}}{-i(\Delta + \Omega) + \kappa/2 + \frac{g_0^2 \bar{n}_{\mathrm{r}}}{+i(\Omega + \Omega_{\mathrm{m}}) - \Gamma_{\mathrm{m}}/2}} \right|^2, \tag{2.48}$$

with $\bar{n}_{\mathrm{r}} = n_{\mathrm{drive}}(P_{\mathrm{drive}}, \Delta) + n_{\mathrm{probe}}(P_{\mathrm{probe}})$ and the detunings $\Delta = \omega_{\mathrm{d}} - \omega_{\mathrm{r}}$ and $\Omega = \omega_{\mathrm{p}} - \omega_{\mathrm{d}}$ which are shown in Fig. 2.11.
We show the expected interaction for a set of reasonable parameters in Fig. 2.12: $\kappa/2\pi = 1.0\,\mathrm{MHz}$, $\kappa_{\mathrm{ext}}/2\pi = 500\,\mathrm{kHz}$, $\Omega_{\mathrm{m}}/2\pi = 13\,\mathrm{MHz}$, $\Gamma_{\mathrm{m}}/2\pi = 10\,\mathrm{Hz}$ and $g_0/2\pi = 100\,\mathrm{kHz}$, $P_{\mathrm{probe}} = 0.5\,\mathrm{pW}$, $P_{\mathrm{drive}} = 15\,\mathrm{pW}$.
In the following we are going to present two ways of implementing such a coupling mechanism into a flux tunable resonator.

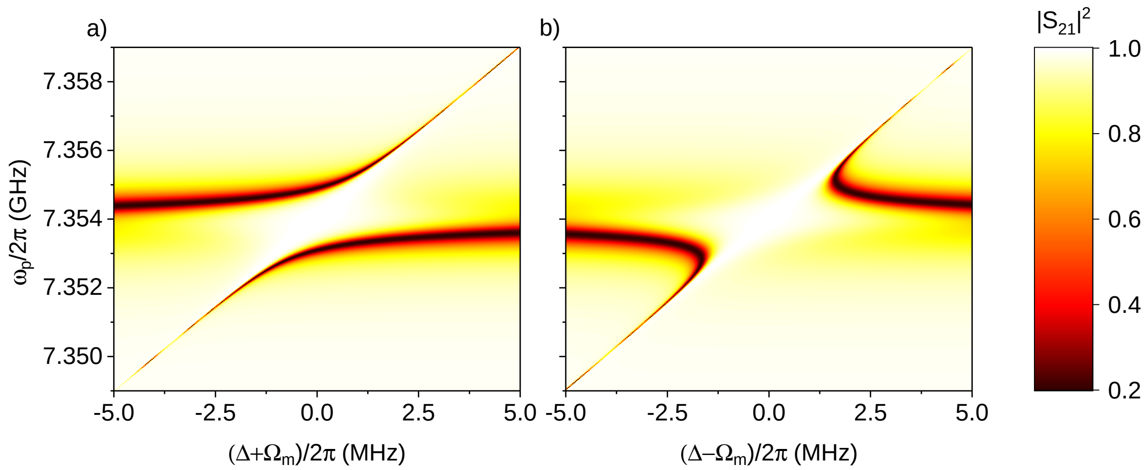

Figure 2.12: Electromechanical interaction in a two-tone spectroscopy setup in the a) red sideband regime and b) blue sideband regime. The drive tone is swept in a frequency range of ± 5 MHz around the perfect detuning. Drive photons are converted into resonator photons by electromechanical interactions in the coupled hybrid device. The converted photons interfere with a weak probe tone and are thus visible in the power transmission spectrum.

2.5 Nanostrings Inductively Coupled to Flux Tunable Resonators

Let us first consider a FTR as introduced in Sec. 2.3, a bare MW resonator with a SQUID embedded at the current anti-node. We integrate a mechanical degree of freedom into this system by replacing one side of the SQUID loop with a doubly clamped mechanical string-resonator. As depicted in Fig. 2.13 the mechanical motion of the string-resonator changes the area of the SQUID loop and subsequently the magnetic flux which passes through it.

We split the total flux into two parts, a static contribution given by length and width of the SQUID loop (Φ_p, blue) and a contribution dependent on the strings displacement ($\Phi_q(x)$, green). The latter one can be calculated by integrating over the lateral shape of the string-resonator. In Ref. [41] it has been derived that the lateral shape of the fundamental mode of a highly stressed double clamped string-resonator aligned along the y-direction and displaced along the x-direction is given by

$$x(y) = x_0 \cos\left(\pi \frac{y}{l}\right) , \tag{2.49}$$

where l is the length of the string-resonator, x_0 the maximum amplitude at $y = 0$ and the clamping points being at $y = \pm l/2$.
The integration yields $\Phi_q = B_z 2lx/\pi$. So the total flux becomes:

$$\Phi(x) = \Phi_p + \Phi_q(x) = B_z lw + B_z \beta l x\,, \tag{2.50}$$

with $\beta = 2/\pi$, B_z the component of the magnetic induction that is perpendicular to the SQUID loop and $x = x_0$ the maximum amplitude of the nanostring. We assume the displacement to be small compared to the length of the string. This assumption is justified as the displacement is

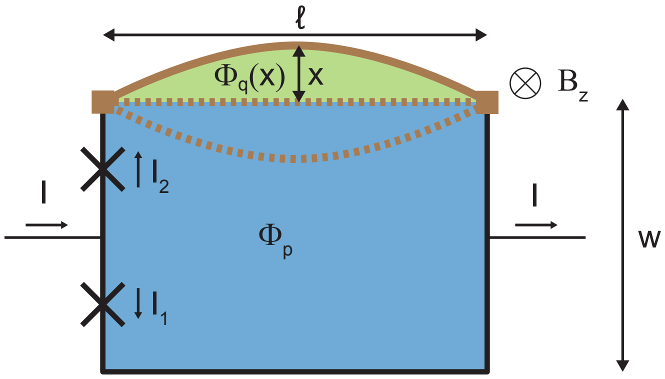

Figure 2.13: Overview scheme of a rectangular SQUID loop with inductively coupled mechanical string-resonator (brown). The mechanical string-resonator is free to oscillate in plane of the SQUID loop and thus modulates its area. In blue we depict the static area given by length and width of the SQUID loop. In green we depict the area modulation due to the nanostrings motion where x is the displacement of the nanostring from its equilibrium position. The magnetic flux passing through the SQUID loop $\Phi = A_{\mathrm{loop}} \times B_{\mathrm{z}}$ is split into a static part Φ_{p} and a contribution $\Phi_{\mathrm{q}}(x)$ modulated by the nanostring.

typically not exceeding a few nm (see Sec. 4.1) while the length is in the order of micro meters.

In the last section we have derived in Eq. (2.35) that the resonance frequency of a FTR depends on the amount of flux that passes through the SQUID loop. Now the flux itself depends on the displacement of the mechanical resonator which results in a direct relation between the resonance frequency of the FTR and the displacement of the mechanical resonator: $\omega_{\mathrm{r}}(\Phi(x))$. We develop $\omega_{\mathrm{r}}(\Phi(x))$ in a Taylor-series around $x = 0$ to first order:

$$\begin{aligned} \omega_{\mathrm{r}}(\Phi(x)) \approx \omega_{\mathrm{r}}|_{x=0} + \left.\frac{\partial \omega_{\mathrm{r}}}{\partial x}\right|_{x=0} x &= \omega_{\mathrm{r}}(\Phi_{\mathrm{p}}) + \left.\frac{\partial \omega_{\mathrm{r}}}{\partial \Phi}\right|_{\Phi=\Phi_{\mathrm{p}}} \frac{\partial \Phi}{\partial x} x \\ &= \omega_{\mathrm{r}}(\Phi_{\mathrm{p}}) + \left.\frac{\partial \omega_{\mathrm{r}}}{\partial \Phi}\right|_{\Phi=\Phi_{\mathrm{p}}} B_{\mathrm{z}} \beta l x \,. \end{aligned} \tag{2.51}$$

By plugging Eq. (2.51) into Eq. (2.40) we simplify the Hamiltonian, as shown for the general case. We find the electromechanical vacuum coupling strength g_0 for inductively coupled string-resonators embedded into the SQUID loop:

$$g_0 = \frac{\partial \omega_{\mathrm{r}}}{\partial \Phi} B_{\mathrm{z}} \beta l x_{\mathrm{zpf}} \,. \tag{2.52}$$

In the Taylor-series we have only considered first order terms. The resulting coupling mechanism is called radiation pressure coupling. If one considers second order terms the so called cross-Kerr coupling becomes apparent [28]. The latter one scales with x^2 and is normally much weaker than the radiation pressure coupling and therefore not observable. In asymmetric SQUIDs however the radiation pressure vanishes at the half integer flux quantum and the cross-Kerr term can become dominant [28].

The aim of this thesis is to observe a high single photon-phonon coupling, ideally entering the strong coupling regime where the vacuum coupling strength exceeds the total loss rate of the MW resonator $g_0 > \kappa$. Furthermore, one can possibly observe the cross-Kerr coupling in asymmetric SQUIDs.
For both, the vacuum coupling strength has to be maximized. The parameters which control the coupling strength became evident in Eq. (2.52). In Refs. [29, 40] a set of experimentally feasible parameters has been proposed which possibly enable access to the strong coupling regime. They will be revised in the following:

Slope of the flux tunable resonator ($g_0 \propto \partial\omega_r/\partial\Phi$):
The electromechanical coupling strength is proportional to the slope of the resonance frequency which means that the working point of the MW resonator controls the coupling strength as shown in Fig. 2.14. For applied flux equal to the integer flux quantum, the resonance curve becomes totally flat i.e. the coupling is switched off. For flux values approaching the half-integer flux quantum the slope becomes infinitely steep in the case of ideal identical Josephson junctions. The ability of switching the coupling on and off makes the device suitable for quantum information processing and phonon lasing applications as discussed in Ref. [25, 63].
In the experiment however, tuning the resonator to very low frequencies is not desired, as at low frequencies, the MW resonator becomes populated with photons. In addition, there are constraints imposed by the measurement apparatus. The cold amplifiers in the experimental setup can only be operated in the range of 2 GHz to 8 GHz. Furthermore screening currents in the SQUID loop ($\beta_L \neq 0$) and asymmetries in the SQUID geometry reduce the modulation depth, so the achievable steepness of the slope is limited. So, for optimal results β_L should be significantly smaller than 1 and asymmetries in the Josephson junctions should be avoided. In previous measurements slopes of $2\pi \times 59\,\mathrm{GHz}/\Phi_0$ have been reported [40].

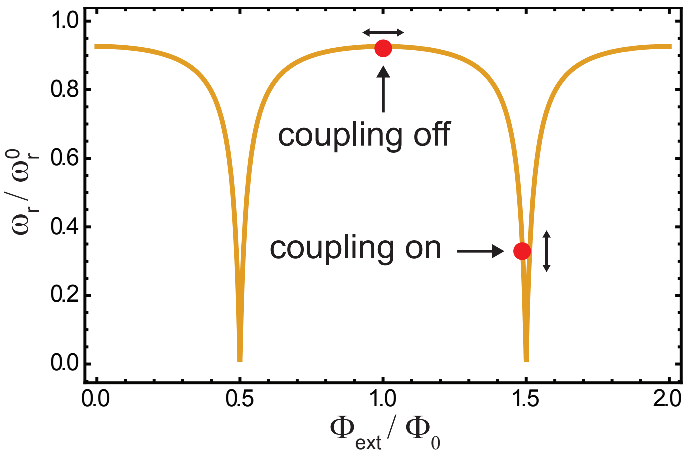

Figure 2.14: The electromechanical coupling can be switched on and off by tuning the FTR. The coupling is strong if the FTR is tuned close to the half integer flux quantum where the slope $\partial\omega_r/\partial\Phi$ is steepest. The coupling is off if the FTR is tuned to the sweet spot at an integer flux quantum where the slope $\partial\omega_r/\partial\Phi$ is flat.

Strength of the magnetic field ($g_0 \propto B_z$):
The coupling strength is proportional to the externally applied static magnetic field B_z which is limited by the critical field of superconducting thin film aluminium. In Ref. [41] it was determined experimentally that the superconductivity in aluminium MW resonators breaks down at 2.2 mT. Furthermore the linewidth κ of the MW resonators increases with magnetic field as shown in Ref. [64]. In order to operate in a regime well below the critical field we intend to apply a maximum magnetic field of $B_z = 1\,\mathrm{mT}$. Higher fields are in principle possible if one applies the magnetic field in plane of the thin film.

Length of the nanomechanical string ($g_0 \propto l$):
The coupling strength is proportional to the length of the nanomechanical strings i.e. the longer the string the stronger the coupling. However, the experiments envisaged in this thesis require the resolved sideband regime: $\Omega_m > \kappa$. With $\Omega_m \propto 1/l$ the maximum length of the string is limited by κ. When designing the SQUID one must additionally consider that the length of the nanostring influences the inductance of the SQUID loop. Increasing the length of the nanostrings leads to an increase in β_L. In order to study the influence of the length on the coupling strength and on β_L we intend to fabricate samples with the length of the nanostrings ranging from 15 µm to 60 µm.

Zero point fluctuation of the nanomechanical string ($g_0 \propto x_{zpf}$):
The coupling strength is proportional to the zero point fluctuation of the nanomechanical strings. We have seen in Eq. (2.7) that the zero point fluctuation becomes large for small mass and small resonance frequency of the nanostring. As the mass depends on l and the resonance frequency on $1/l$, the length of the strings cancels out and x_{zpf} depends only on width, thickness and material parameters. Strings with widths of 80 nm have been successfully fabricated [41, 65]. The thickness is limited to 110 nm due to restraints imposed by the shadow evaporation technique, resulting in effective beam masses of $m_{eff} \approx 1\,\mathrm{pg}$.

For string widths of 80 nm we expect a zero point fluctuation of $x_{\mathrm{zpf}} \approx 58\,\mathrm{fm}$.

With the assumptions made above we estimate the maximum vacuum coupling strength to be:

$$\frac{g_0}{2\pi} \approx 59\,\mathrm{GHz}/\Phi_0 \cdot 1\,\mathrm{mT} \cdot \beta \cdot 60\,\mathrm{\mu m} \cdot 58\,\mathrm{fm} = 65.8\,\mathrm{kHz} \tag{2.53}$$

2.6 Magnetic Force Microscopy Cantilevers Coupled to Flux Tunable Resonators

Above we have introduced the idea of coupling mechanical motion to a MW field by integrating a mechanical string-resonator into a FTR. We discuss in the following an alternative method of inductive coupling. Instead of integrating the mechanical string-resonator into the FTR, in this approach a commercial cantilever with a ferro-magnetic tip is mounted on top of the FTR.
The magnetic dipole at the tip of the cantilever causes a magnetic dipole field which scales with the distance as $1/|r|^3$. The amount of flux passing through the SQUID loop thus depends on the distance between cantilever tip and SQUID.
As the cantilever vibrates up and down at a given frequency Ω_{m}, the magnetic flux in the SQUID loop is modulated and results in a frequency shift of the FTR identical to the case of embedded mechanical string-resonator discussed above. In the following we derive the coupling strength of an inductively coupled cantilever and compare it to the one of an embedded string-resonator.
A schematic drawing of the system is depicted in Fig. 2.15.

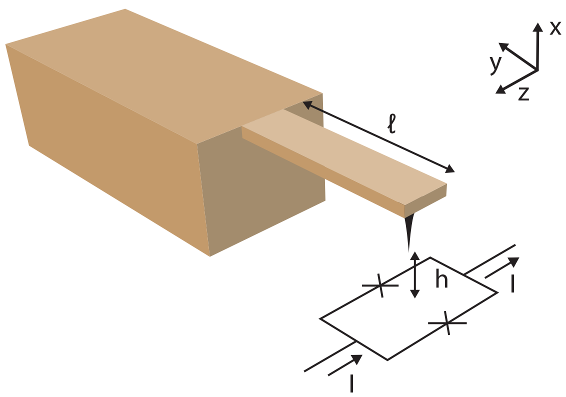

Figure 2.15: Schematic drawing of an inductively coupled cantilever with magnetic tip. The cantilever is mounted onto a FTR with the tip beeing placed over the SQUID loop at a height h. The magnetic dipole moment of the cantilever tip induces a magnetic field in the SQUID loop plane with an $1/h^3$ dependence, where h is the distance between dipole and SQUID loop. Vibration of the cantilever arm results in flux change in the SQUID loop and following a shift of the resonance frequency of the FTR.

We start our discussion by calculating the magnetic field of the dipole in a steady state. The shape is identical to the field of an electrical dipole and reads in spherical coordinates [66]:

$$\vec{B}(\vec{r}) = \frac{\mu_0|\vec{m}|}{4\pi|\vec{r}|^3}(2\cos\theta \cdot \hat{r} + \sin\theta \cdot \hat{\theta})\,, \tag{2.54}$$

with $\vec{m}$ the magnetic moment and $\vec{r}$ the position relative to the dipole. In cartesian coordinates the magnetic field in the x-z plane is given by:

$$\vec{B}(z{,}x) = \frac{\mu_0|\vec{m}|}{4\pi(x^2+z^2)^{3/2}}(3\cos\theta\sin\theta \cdot \hat{z} + 2(\cos^2\theta - \sin^2\theta)\hat{x})\,, \tag{2.55}$$

with $\theta = \arctan z/x$.
We plot Eq. (2.55) in figure 2.16 and note that only the $\hat{x}$ component of $\vec{B}$ contributes to the magnetic flux in the SQUID loop which is indicated by a red line.

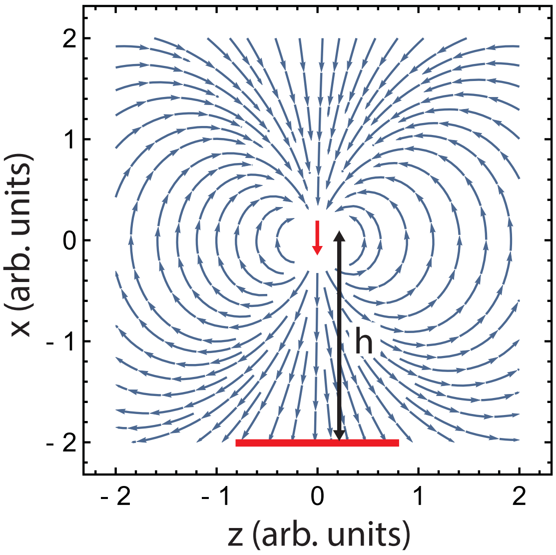

Figure 2.16: Magnetic field of a dipole (red arrow) in the x-z plane. The cross section of the SQUID loop is indicated by a red line

The SQUID loops considered here have a rectangular shape, extended in z direction ($\approx 60\,\mu$m) and very narrow in the y direction ($\approx 2\,\mu$m). We therefore consider the magnetic field being constant in y direction and calculate the total magnetic flux per width, by integrating $B_x(z{,}x)$ over the length of the SQUID loop for a given height $x = h$:

$$\begin{aligned}\frac{\Phi(x)}{w_s} &= \int_{-l_s/2}^{l_s/2} B_x(z{,}x)dz = \int_{-l_s/2}^{l_s/2} \frac{\mu_0|\vec{m}|}{2\pi(x^2+z^2)^{3/2}}\left[\cos^2\left(\arctan\left(\frac{z}{x}\right)\right) - \sin^2\left(\arctan\left(\frac{z}{x}\right)\right)\right]dz \\ &= \frac{\mu_0|\vec{m}|}{6\pi x^2(x^2+z^2)^{3/2}}\left(z\left(z^2+3x^2\right)\right)\Big|_{-l_s/2}^{l_s/2} = \frac{\mu_0|\vec{m}|l_s}{6\pi x^2\left(\frac{l_s^2}{4}+x^2\right)^{3/2}}\left(\frac{l_s^2}{4}+3x^2\right)\,, \end{aligned} \tag{2.56}$$

with w_s and l_s the length and the width of the SQUID loop.

With Eq. (2.56) we have calculated how the magnetic flux in the SQUID loop depends on the height of the cantilever.
For $x \gg l_\mathrm{s}$ all dimensions are small compared to x and the magnetic field can be considered being constant over the whole SQUID loop (far field approximation). Equation (2.56) then simplifies to:

$$\Phi(x) = w_\mathrm{s} \cdot l_\mathrm{s} \cdot \frac{\mu_0 |\vec{m}|}{2\pi x^3} , \tag{2.57}$$

To compare the near field calculation to the far field approximation we plot both models for typical parameters of a commercial magnetic force microscopy cantilever in Fig. 2.17 a). The assumed parameters of the cantilever are presented in Tab. 2.1 and the area of the SQUID loop was assumed to be $A_\mathrm{loop} = 2 \times 60\ \mu\mathrm{m}^2$. We see that for small distances between cantilever and SQUID loop ($x < 40\,\mu\mathrm{m}$) the far field approximation starts to deviate.

parameter	value
h	$100\,\mu\mathrm{m}$
$\|\vec{m}\|$	$1 \cdot 10^{-16}\,\mathrm{A/m^2}$
Ω_m	$70\,\mathrm{kHz}$
k	$3\,\mathrm{N/m}$
m_eff	$2.66 \cdot 10^{-10}\,\mathrm{kg}$
x_zpf	$1.6\,\mathrm{fm}$

Table 2.1: Typical parameters of a commercial magnetic force microscopy cantilever.

Furthermore we have seen in Sec. 2.5 that the vacuum coupling strength is given by:

$$g_0 = \frac{\partial \omega_\mathrm{r}}{\partial \Phi} \frac{\partial \Phi}{\partial x} x_\mathrm{zpf} . \tag{2.58}$$

To maximize the coupling strength we have to tune the setup, such that the derivative $\partial\Phi(x)/\partial x$ is maximized. In Fig. 2.17 a) we see that the slope of $\Phi(x)$ becomes steep for small distances between cantilever and SQUID loop. Therefore, in order to achieve strong coupling the tip of the cantilever should be brought to the SQUID loop as close as possible. We plot the derivative of the near field calculation in Fig. 2.17 b) and observe that for distances $x < 20\,\mu\mathrm{m}$ the slope becomes significantly steep.
We assume that $x = 10\,\mu\mathrm{m}$ is the smallest experimentally feasible distance and evaluate the coupling strength for this value according to Eq. (2.58):

$$\frac{g_0}{2\pi} = 59\,\mathrm{GHz}/\Phi_0 \cdot 27.3\,\Phi_0/\mathrm{m} \cdot 1.6\,\mathrm{fm} = 2.6\,\mathrm{mHz} . \tag{2.59}$$

The coupling strength achievable with a cantilever is 7 orders of magnitude smaller than the one of an embedded string-resonator. The reason for this big discrepancy is that the magnetic moment of the cantilever tip is small and so the change in magnetic flux induced by the vibration of the tip is small as well.
In the case of the embedded string-resonator the value of $\partial\Phi/\partial x$ scales with the externally applied magnetic field and can therefore be ramped up strongly. Furthermore the string-resonators in the embedded design are optimized for large zero point fluctuations resulting in $x_\mathrm{zpf} = 58\,\mathrm{fm}$,

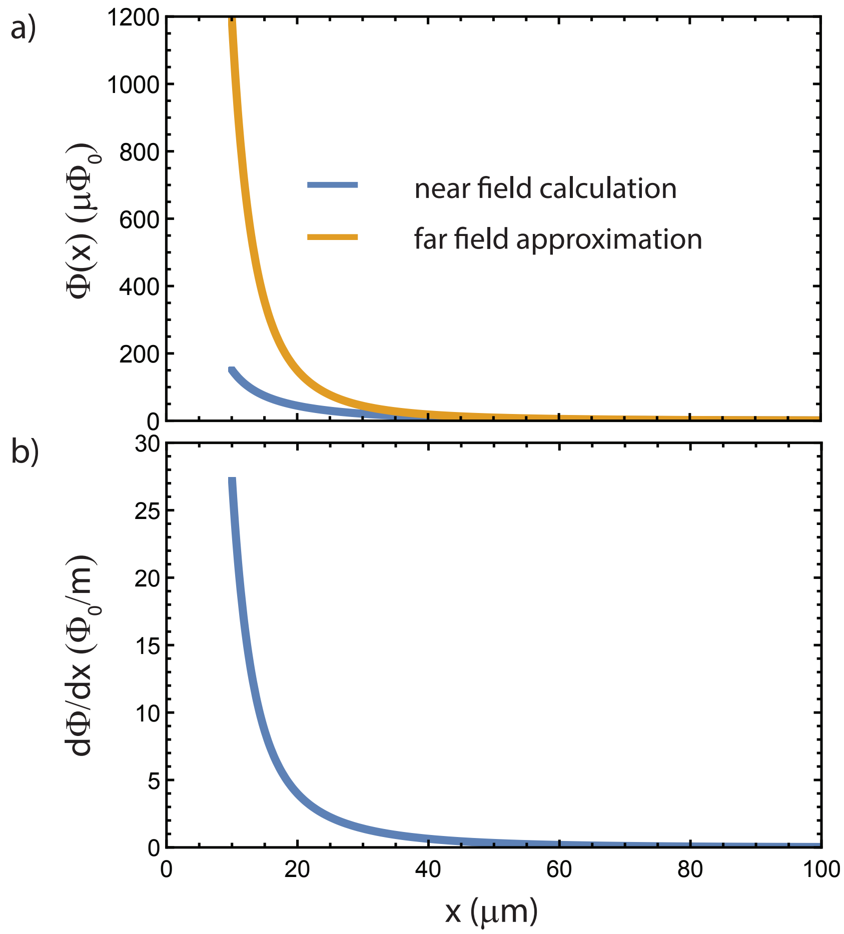

Figure 2.17: Magnetic flux induced in a SQUID loop of dimensions $A_{\text{loop}} = 2 \times 60\ \mu\text{m}^2$ by a commercial magnetic force microscopy cantilever positioned over the SQUID loop at height x. In panel a) the near field calculation according to Eq. (2.56) is compared to the far field approximation according to Eq. (2.57) in the range $10\,\mu\text{m} < x < 100\,\mu\text{m}$. The far field approximation deviates for heights $x < 40\,\mu\text{m}$. In panel b) we plot the derivative of Eq. (2.56) and see that for strong inductive coupling the distance between cantilever and SQUID loop should be small ($g_0 \propto \partial\Phi/\partial x$).

whereas the one of the cantilever is ≈ 35 times smaller.
An additional problem arises as the mechanical resonance frequency $\Omega_{\text{m}} = 70\,\text{kHz}$ is smaller than the linewidth of the FTR. The necessary condition of the resolved sideband regime ($\Omega_{\text{m}} > \kappa$) is not given which reduces the variety of experimental methods that can be applied.

The arguments presented above show that the performance of an embedded string-resonator outruns the one of a cantilever. Therefore we have focused in the experimental part of this thesis on the fabrication of the design shown in Sec. 2.5.

2.7 Detection of Electromechanical Interaction - Noise Analysis

A fundamental aspect for the success of this thesis is whether or not the sensitivity of the SQUID is sufficient to detect the mechanical motion of the string-resonator. To answer this question we compare the flux changes expected from the mechanical motion with the typical noise performance of the SQUID.
In Sec. 2.5 we have shown that the effective flux change in the SQUID loop is given by $\delta\Phi = B_z\beta l\delta x$. According to Eq. (2.6) the rms displacement δx of the string-resonator in a thermal state $\bar{n}_m$, is given by:

$$\delta x = x_{\mathrm{zpf}} \cdot \sqrt{2\bar{n}_{\mathrm{m}} + 1}\,. \tag{2.60}$$

At 100 mK a mechanical string-resonator with length $l = 60\,\mu$m, $\Omega_{\mathrm{m}}/2\pi = 3.44\,$MHz and $x_{\mathrm{zpf}} = 58\,$fm is occupied by $\bar{n}_{\mathrm{m}} = 605$ phonons resulting in the rms noise amplitude $\delta x = 2\,$pm. At $B_z = 1\,$mT the strings thermal motion results in a flux change of $\delta\Phi = 38\,\mu\Phi_0$. The total flux change is distributed over the Lorentzian mechanical response spectrum. We estimate the necessary flux sensitivity $\delta\Phi/(\Gamma_{\mathrm{m}}/2\pi)^{1/2} \approx 12\,\mu\Phi_0/\mathrm{Hz}^{1/2}$, assuming $\Gamma_{\mathrm{m}}/(2\pi) = 10\,$Hz.
The flux resolution of low temperature dc-SQUIDs is known to be close to the quantum limit [67]. In Ref. [68] it has been shown that sensitivities of $0.01\,\mu\Phi_0/\mathrm{Hz}^{1/2}$ are theoretically possible. This implies that the sensitivity of a state of the art SQUID is sufficient to resolve the mechanical motion in our device. In the year 2008 it has indeed been demonstrated experimentally in Ref. [30] that detection of motion of a string-resonator embedded into a dc-SQUID is possible. The device which is used in the reference is similar to ours, reporting a flux resolution of $10\,\mu\Phi_0/\mathrm{Hz}^{1/2}$.
We can sum up that the flux modulation induced by the mechanical string-resonator in our device is close to the resolution limits of typical flux detectors presented in literature. If our SQUID provides similar performance, a detection of the mechanical motion is challenging but should be in principle possible.

In the following we are going to analyse the noise sources being present in our setup. Hereby one has to distinguish between white noise and spectral noise. White noise arises from thermal fluctuations in the SQUID loop as well as in the electronics which are used to amplify the signal. It contributes equally to all frequencies. Spectral noise can arise from background magnetic fields emitted e.g. by hand-held mobile devices. Generally speaking we are able to detect the mechanical motion of our string-resonator if the resulting spectral signal is bigger than the sum of all noise contributions. Additionally the sensitivity of the SQUID must be sufficient to resolve the signal.
We start the discussion with the sensitivity of the SQUIDs.
The dc-SQUIDs discussed in Refs. [30, 68] are operated in the voltage state, i.e. they are biased by a current $I > 2I_{\mathrm{c}}$. In contrast, our device is operated in the zero voltage state. In the following we are going to discuss the differences between the voltage and the zero voltage state.

In the voltage state the SQUID produces an output voltage that depends on the externally applied magnetic flux [47]. A small change of magnetic flux results in a change of voltage, which can be read out. The performance of the SQUID is determined by the flux-to-voltage transfer function [47]:

$$H_{\mathrm{V}} = \left| \left(\frac{\partial V}{\partial \Phi_{\mathrm{ext}}} \right) \right| , \tag{2.61}$$

which relates the power spectral densities of voltage and magnetic flux [47]:

$$S_{\Phi\Phi}(\Omega) = \frac{S_{\mathrm{vv}}(\Omega)}{H_{\mathrm{V}}^2} . \tag{2.62}$$

The sensitivity increases with H_{V}, i.e. small flux changes result in large voltage changes if H_{V} is large. For dc-SQUIDs in the voltage state the flux-to-voltage transfer function is proportional to the product $I_{\mathrm{c}}R_{\mathrm{n}}$ and best performance can be achieved by choosing the parameters of the SQUID such that $\beta_{\mathrm{L}} \simeq 1$ and $\beta_{\mathrm{c}} \simeq 1$ [47].
In a typical setup the voltage modulation is amplified and then detected at room temperature. In the supplementary material of Ref. [31] for example, it is stated that for their setup $H_{\mathrm{V}} = 1.7\,\mu\mathrm{V}/\mu\Phi_0$ and they record a voltage noise floor of $\sqrt{S_{\mathrm{VV}}} = 4.1\,\mu\mathrm{V}/\mathrm{Hz}^{1/2}$ after the amplifiers. According to Eq. (2.61) this results in a spectral flux sensitivity of $S_{\Phi\Phi} = 5.8\,\mu\Phi_0/\mathrm{Hz}^{1/2}$.

In the zero voltage state the current through the SQUID is smaller than $2I_{\mathrm{c}}$. The SQUID does not produce an output voltage. Limitations for the magnetic field resolution in the superconducting state are rarely discussed in the literature and are going to be analysed in the following.
In our device a change of flux produces a frequency shift of the FTR. Therefore we introduce the flux-to-frequency transfer function

$$H_{\Phi} = \left| \left(\frac{\partial \omega}{\partial \Phi_{\mathrm{ext}}} \right) \right| , \tag{2.63}$$

which relates the power spectral densities of magnetic flux and frequency:

$$S_{\Phi\Phi}(\Omega) = \frac{S_{\omega\omega}(\Omega)}{H_{\Phi}^2} \tag{2.64}$$

The transfer function equals the slope of the FTR and therefore the flux sensitivity is limited by I_{c}, α_{I} and β_{L}. The transfer function is connected to those parameters as we have seen in Sec. 2.3.

Let us now discuss different sources of noise which are present in our setup. First, the SQUID itself can be a source of noise. In literature [48], in principle two types of noise are considered as the main contribution in SQUIDs: thermal noise and $1/f$ noise. As the mechanical modes of interest are in the order of MHz, the $1/f$ noise is negligible in our case.
Thermal noise generally speaking leads to fluctuations of the current around its mean value. It is gaussian distributed and contributes equally to all frequencies (white noise). According to the Nyquist theorem the junction resistance produces a noise voltage of [48]:

$$S_{\mathrm{v}}(f) = 4k_{\mathrm{B}}TR . \tag{2.65}$$

The resistance is considered as noisy element and according to Refs. [48, 69] the resulting voltage across the SQUID and the current noise around the SQUID are partially correlated. For practical dc-SQUIDs, especially high T_c, operated in the voltage state, this is a big issue and imposes limits upon the inductance of the SQUID loop. In order to avoid the suppression of macroscopic quantum interference the SQUID inductance should be significantly smaller than $L_F = (\Phi_0/2\pi)^2/k_B T$. At 4 K this condition is easily met if the loop inductance is in the order of a few pH.
According to the theory presented in Refs. [48, 69], the thermal noise contributions are only relevant in the resistive voltage state. In particular, fluctuations of the current which flows across the SQUID do not result in flux noise if the SQUID is in the zero voltage state. Only circulating currents could limit the sensitivity, as they directly create flux in the SQUID loop. We assume that for $\beta_L \ll 1$ circulating currents are suppressed.
To sum up, the fact that our device is entirely operated in the zero voltage state could imply an increase in sensitivity compared to the operation of an equivalent device in the voltage state.

Second, environmental background noise which threads the SQUID loop can be a source of noise. In Ref. [70] it has been shown that natural and man-made terrestrial noise in the MHz regime is not negligible. To avoid unwanted environmental noise, the sample chamber should be properly shielded. Furthermore, the intended experiments involve applying an external magnetic field by a superconducting coil. Fluctuations of the magnetic field result in flux noise in the SQUID loop. The coil however acts as a low pass filter and fluctuations in the MHz regime become negligible.

Third, the amplifier and the read out electronics can be a source of noise. One can analyse this source of noise by tuning the FTR to the sweet spot, where the flux-to-frequency transfer function is zero. In this state the SQUID is switched off and the setup is not sensitive to the two sources of noise mentioned above.

In the following we are going to introduce two methods of quantifying the noise.
In our system, magentic flux fluctuations of any sort (noise and signal) at a frequency ω_{fluct} result in fluctuations of the FTR resonance frequency. They are detected using a homodyne detection scheme and appear in the measured power spectral density as peaks at $\pm\omega_{\mathrm{fluct}}$. White noise, being frequency independent, consequently increases the noise floor of the measured power spectral density.
The measured power spectrum of the mechanical sidebands is connected to the frequency fluctuation spectrum by [41]:

$$S_{\mathrm{pp}}(\Omega) = \frac{2K(\Omega)}{\Omega^2} S_{\omega\omega}(\Omega) = \frac{2K(\Omega)H^2}{\Omega^2} S_{\Phi\Phi}(\Omega)\,, \tag{2.66}$$

where $K(\Omega)$ is the MW transfer function [41] introduced in Sec. 2.4.1:

$$K(\Omega_{\mathrm{mod}}) = 2 \cdot \mathrm{ENBW} \cdot S_{\mathrm{pp}}^{\mathrm{mod}} \cdot \frac{\Omega_{\mathrm{mod}}^2}{\Omega_{\mathrm{dev}}^2}\,. \tag{2.67}$$

At Ω_{mod}, $K(\Omega_{\text{mod}})$ can be determined experimentally employing a calibration tone with a known frequency modulation depth Ω_{dev}. The amplitude of the measured sideband peak $S_{\text{PP}}^{\text{mod}}$ allows the calibration as explained in Ref [61]. With knowledge of both transfer functions one can calibrate the flux sensitivity of the setup. The transfer function can be plugged into Eq. (2.66) and yields the calibrated flux noise for ($\Omega \approx \Omega_{\text{mod}}$):

$$S_{\Phi\Phi}(\Omega) = \frac{\Omega_{\text{dev}}^2}{4\text{ENBW} \cdot H^2} \frac{S_{\text{pp}}^{\text{noise}}}{S_{\text{pp}}^{\text{mod}}} , \tag{2.68}$$

where $S_{\text{pp}}^{\text{noise}}$ is the noise floor of the measured power spectrum and $S_{\text{pp}}^{\text{mod}}$ the amplitude of the sideband peak introduced by the injected modulation.

Another method of quantifying the flux noise is to analyse how the linewidth of the FTR depends on the flux-to-frequency transfer function H. At working points with $H = 0$, the FTR is not sensitive to flux modulations. At working points with $H \neq 0$, the resonance frequency ω_{r} fluctuates with flux noise leading to a linewidth broadening in time averaged measurements. Consequently one can analyse the sensitivity of the SQUID by comparing the linewidth of the FTR at $H = 0$ and $H \neq 0$.
With this method however, one can not determine at which frequency the fluctuation occurs. As long as the fluctuation of the magnetic flux is significantly faster then the measurement time, any noise in the frequency spectrum contributes to the linewidth broadening. It is therefore challenging to give the appropriate value in typical units of $\Phi_0/\text{Hz}^{1/2}$ and requires further studies.

From a general point of view we summarize that resolution limits can arise from:

- the read out electronics, in particular the noise floor of amplifiers between sample and detector, also considered as imprecision noise.
- the sensitivity of the SQUID which is defined by the flux-to-frequency transfer function and noise sources in the SQUID itself.
- environmental background noise which threads the SQUID loop.

All in all our setup is well optimized and comparable with state of the art experiments reported in literature.

Chapter 3

Sample Layout, Fabrication and Experimental Setups

In this chapter we are going to present the sample layout of our nanomechanical hybrid system, the fabrication procedure which we have developed during this masters thesis and the experimental setups which have been used to characterize the fabricated samples. We start with the discussion of the sample layout.

3.1 Sample Layout

An overview of the final sample layout with all its components is shown in Fig. 3.1. In the following we give an introduction to the sample layout, then we explain each component as well as the parameters in detail.
On the edges of the chip, we have two RF contacts which are connected by a straight coplanar waveguide. We will refer to this structure as 'transmission-line' or 'feed-line'. By attaching bond wires to these contacts we can later connect the transmission-line to an external MW source and send microwaves through the chip.
Next to the feed-line we place six CPW $\lambda/4$ MW resonators which are capacitively coupled to the feed-line and have different lengths, hence different frequencies. We terminate 4 of the MW resonators with an aluminium SQUID. One arm of each SQUID loop is underetched, so that these arms are free to vibrate and form the mechanical string-resonators.
Furthermore, eight gold contact-pads for precharacterisation of SQUIDs and a test pattern of mechanical string-resonators are situated at one side of the chip.
We deposit alignment markers at the corners of the chip. With the help of these markers we align the sample with nanometre precision in each fabrication step.
In the following we describe the components in detail.

3.1.1 Transmission-Line and MW Resonators

In Fig 3.2 a) we depict an overview of the the transmission-line and the MW resonators. The central conductor of the transmission-line has a width of 18 µm and a gap to the groundplane of

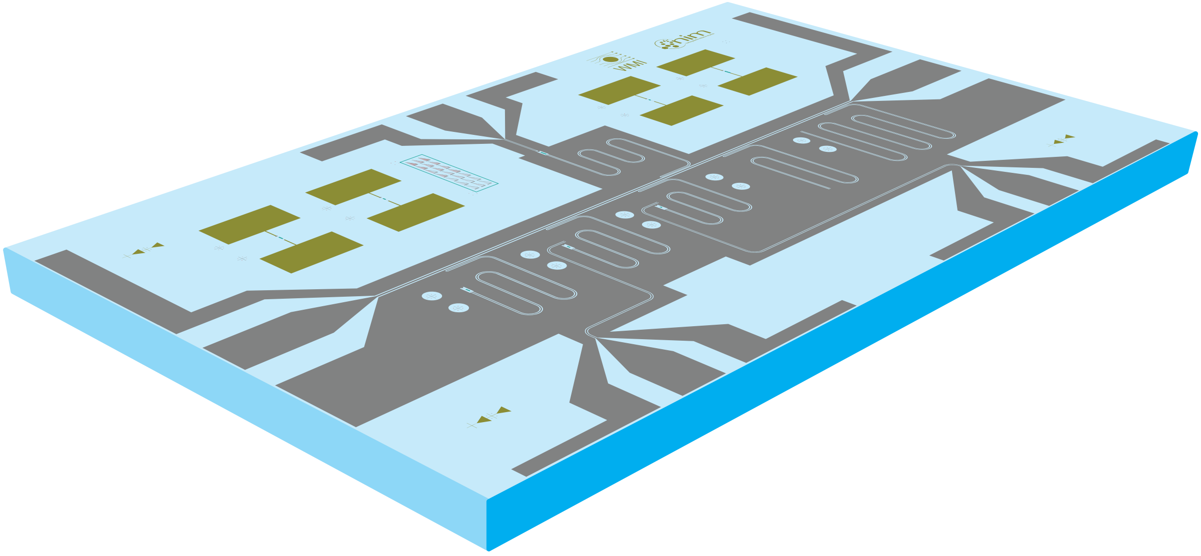

Figure 3.1: Overview of the sample layout with all components on the $6 \times 10\,\mathrm{mm}^2$ silicon substrate.

$12\,\mu\mathrm{m}$ which results in an impedance of $Z_0 \approx 50\,\Omega$. The $\lambda/4$ CPW MW resonators are aligned along the transmission line and for clarity we associate the MW resonators with names. Starting in the bottom line on the left hand side we call the first resonator FTR1 the second one FTR2, the third one FTR3. The fourth and the fifth resonator are named MWR2 and MWR1. In the upper half of the layout there is one resonator which is named FTR4 (compare Fig. 3.2 a)). In Fig. 3.2 b) we depict exemplary a zoom into MW resonator FTR1. For all the MW resonators the width of the central conductor is $10\,\mu\mathrm{m}$ and the gap to the ground plane is $8\,\mu\mathrm{m}$ corresponding to an impedance of $Z_0 \approx 50\,\Omega$ as well. The gap between the central conductor of each MW resonator and the transmission-line is designed to be $45\,\mu\mathrm{m}$. The MW resonators differ in length resulting in resonance frequencies ranging from 4 GHz to 8 GHz. We have fabricated samples with two different versions of the layout, where in the second version the lengths of the MW resonators have been changed according to the outcomes of the first layout.
Four of the MW resonators (FTR1, FTR2, FTR3 and FTR4) have an embedded SQUID at their current anti-node and are therefore flux tunable. The other two MW resonators do not contain a SQUID and are used to determine the dielectric coefficient ϵ_{eff} of the substrate.
For additional flux pumping in the squid loop FTR2, FTR3 and FTR4 are equipped with an antenna.
The lengths of all MW resonators as defined in the layouts are given in Tab. 3.1. We write down the resonance frequency of the bare resonators as given by equation (2.8) assuming $\epsilon_{\mathrm{eff}} = 6.45$ [40]. For those resonators which have an embedded SQUID we have considered that the length of the resonators is elongated by $114\,\mu m$ (length of the squid loop + contact striplines), the effect of the SQUID inductance is not considered in ω_{r}^0. Depending on the critical currents of the SQUIDs, the measured resonance frequencies of FTR1 to FTR4 will differ from ω_{r}^0 as predicted by Eq. (2.35) due to the additional SQUID inductance.

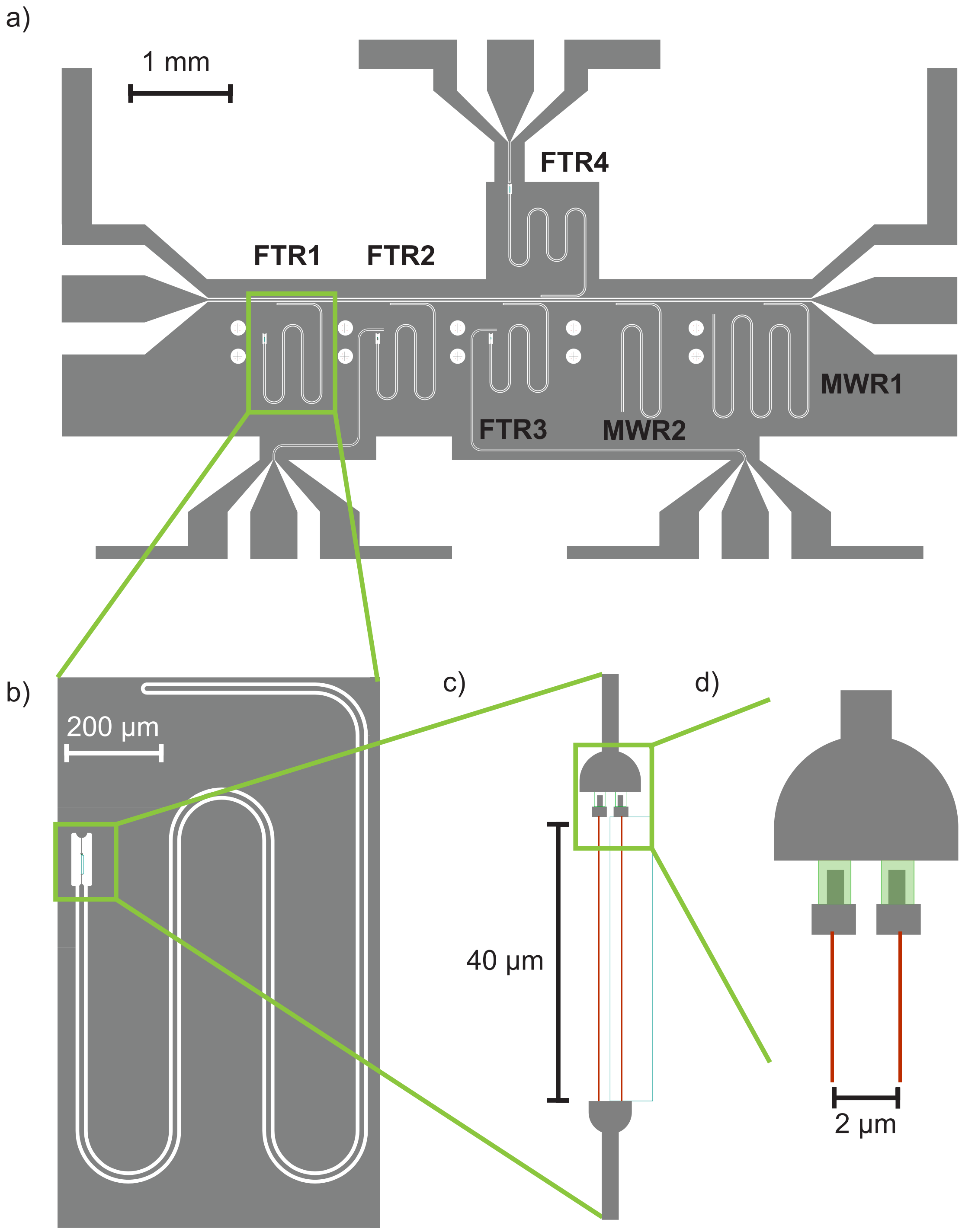

Figure 3.2: Aluminium structures that are going to be deposited on the substrate. From a) to d) detail level increases with a) the whole sample b) a single microwave resonator, c) a single SQUID including two Josephson junctions and two arms that build the SQUID loop, d) detailed zoom into the shadow evaporation mask for Josephson junctions.

	layout #1		layout #2	
MW resonator	l_{r} (mm)	$\omega_{\mathrm{r}}^0/2\pi$ (GHz)	l_{r} (mm)	$\omega_{\mathrm{r}}^0/2\pi$ (GHz)
FTR1	4.221	6.991	4.191	7.046
FTR2	3.883	7.604	4.027	7.333
FTR3	3.573	8.264	3.719	7.940
FTR4	4.219	6.999	4.367	6.762
MWR1	5.380	5.485	7.384	4.000
MWR2	3.741	7.894	3.741	7.894

Table 3.1: Design parameters and calculated resonance frequencies of the 6 MW resonators on the chip. Two layouts have been used during this thesis. In the first column of each layout we give the length l_{r} of the MW resonators as defined in the layout. In the second column we calculate the resonance frequency $\omega_{\mathrm{r}}^0/2\pi$ of the bare resonators as given by Eq. (2.8) for $\epsilon_{\mathrm{eff}} = 6.45$. For resonators FTR1 to FTR4 an elongation of the resonator length by 114 μm due to the length of the SQUID loop and the contact striplines is taken into account. Frequency shifts due to the SQUID inductance are not taken into account.

3.1.2 SQUIDs and Mechanical String-Resonators

As mentioned above, SQUIDs are embedded into FTR1, FTR2, FTR3 and FTR4 at the current anti-node, as depicted in Fig. 3.2 b) and c). Furthermore we have duplicated these SQUIDs and connected them to contact pads outside of the MW circuit for dc-measurements. We depict an overview of the sample where all SQUIDs are indicated and associated with unique names in Fig. 3.3.

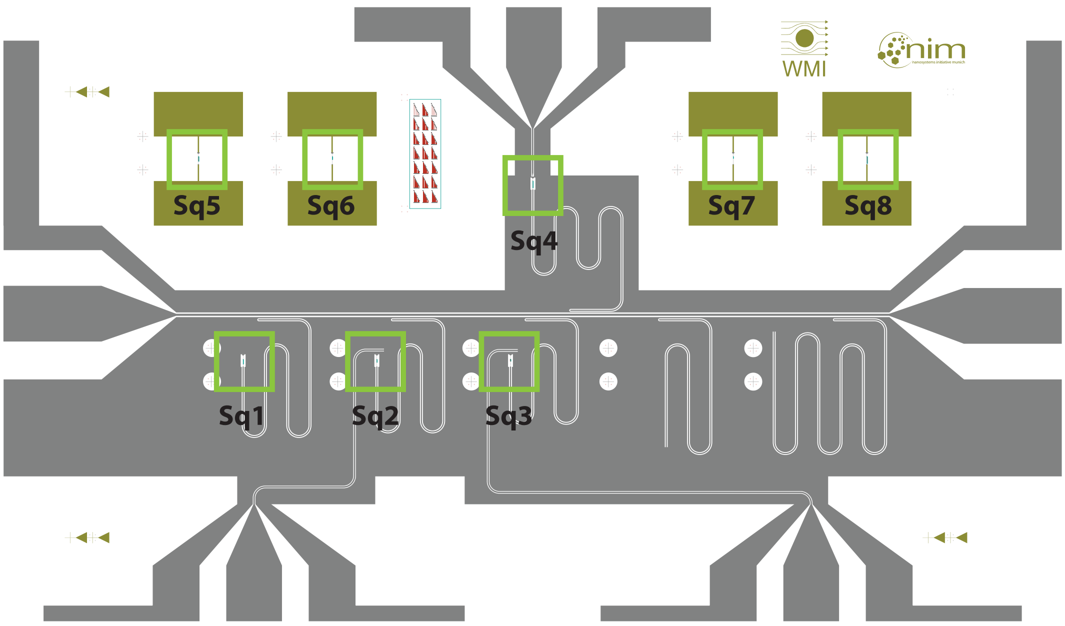

Figure 3.3: Overview of the sample layout. All SQUIDs are indicated by green rectangles and associated with unique names. The SQUIDs (Sq1,...,Sq4) are embedded into the MW resonators (FTR1,...,FTR4) respectively. The SQUIDs (Sq5,...,Sq8) are duplicates of (Sq1,...,Sq4) outside of the MW circuit, used for dc-measurements.

Important parameters of SQUIDs are the length of the strings which define the length of the SQUID loop l_{loop}, also called SQUID arms and the distance between the SQUID arms, which defines the width of the SQUID loop w_{loop}. These parameters define the SQUID loop-area $A_{\text{loop}} = l_{\text{loop}} \cdot w_{\text{loop}}$ and so, the amount of magnetic flux that is caught by the SQUID loop. Parameters of the SQUIDs vary from Sq1 to Sq4 and are shown in Tab. 3.2.
Additionally, one has to define the parameters of the Josephson junctions in the SQUIDs. By setting the junction width one controls the junction area and finally the critical current that can flow through the junction. The width of the junctions is $w_{\text{JJ}} = 2\,\mu\text{m}$ in layout #1 and $w_{\text{JJ}} = 0.5\,\mu\text{m}$ in layout #2. The length of the junctions is defined by the shadow evaporation process and is $L_{\text{JJ}} \approx 235\,\text{nm}$. On each SQUID, both Josephson junctions except for one case are identical in terms of the design parameters. Only in Sq4 we have realized an asymmetric SQUID with $\alpha_{\text{I}} = 1/3$ where the left junction has a design width of 333 nm and the right one of 666 nm.

Last but not least, we give the parameters of the mechanical string-resonators, which are the length l_{string}, the width w_{string} and the thickness t_{string}. As explained at the beginning of this chapter, the string-resonators are realised by underetching one arm of each SQUID loop. Consequently, the length of the string-resonator equals the length of the SQUID loop ($l_{\text{string}} = l_{\text{loop}}$). We discussed the influence of the nanostring parameters on the electromechanical coupling in detail in section 2.5. Although it is possible to fabricate free standing doubly clamped mechanical string-resonators with lengths of 80 µm, we restrict ourselves to $l < 60\,\mu\text{m}$ in order to keep β_{L} small. The thickness of the string-resonators is defined by the thickness of the evaporated aluminium layer and is fixed to $t_{\text{string}} = 110\,\text{nm}$. Parameters of the strings, the resulting loop area, the loop inductance and the β_{L} parameter are given for all SQUIDs in Tab 3.2. The fabrication of nanostrings is a demanding task and the yield is only good if all

SQUID	w_{string} (nm)	l_{loop} (µm)	w_{loop} (µm)	A_{loop} (µm^2)	L_{loop} (pH)	β_{L}
Sq1	80	40	1.7	68	304	0.31
Sq2	100	25	2	50	165	0.16
Sq3	150	15	2	30	77	0.08
Sq4	80	60	2	120	448	0.45

Table 3.2: Parameters of the SQUIDs including mechanical string-resonators. The length of the string-resonator defines the length and the area of the SQUID loop. In order to keep β_{L} small, the string length is limited by $l < 60\,\mu\text{m}$. The loop inductance is calculated according to Eqs. (2.32) and (2.33) for the given parameters. For the calculation of β_{L} we have assumed a typical critical current of $I_{\text{c}} = 1\,\mu\text{A}$.

parameters in the fabrication process are optimized. Releasing the mechanical system is the last step in the fabrication procedure and if an embedded string-resonator breaks this destroys the corresponding FTR. Therefore in the progress of finding best fabrication parameters one needs sufficiantly many nanostrings to have good statistics about the yield. We have added an array of 3×7 test patterns to the layout, whereas each pattern contains ten nanostrings with lengths ranging from 10 µm to 100 µm. One of these test patterns is schematically displayed in Fig. 3.4 a) next to microscope pictures of the fabricated structures in Fig. 3.4 b).

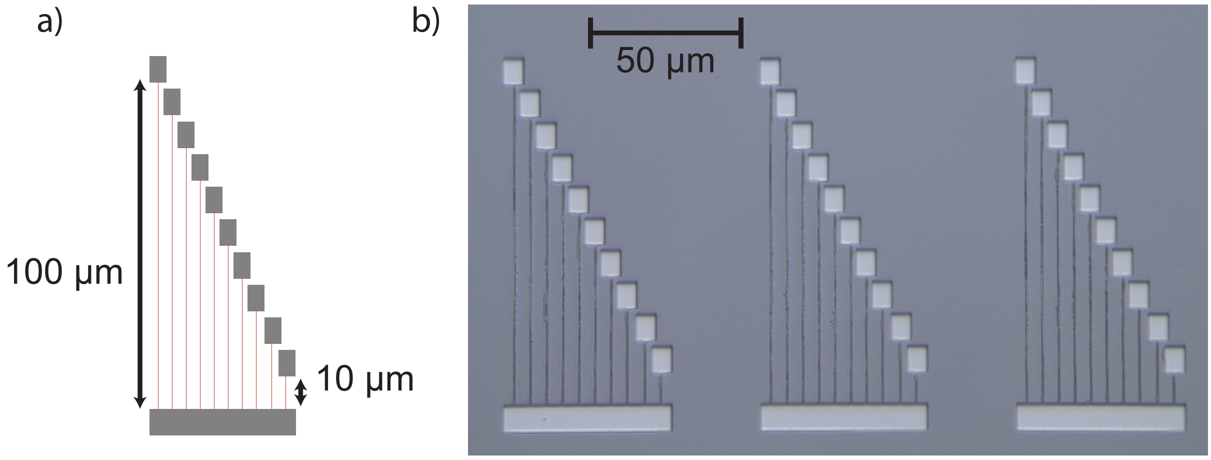

Figure 3.4: Test pattern to optimize the fabrication process of double clamped nanostrings. In panel a) the pattern is schematically displayed. The strings have lengths ranging from 10 µm to 100 µm in 10 µm steps. In panel b) a microscope picture of the fabricated structure is shown.

3.2 Fabrication

The samples investigated in this thesis are fabricated on a silicon substrate. Even though the fabrication procedures for all the components are well established at the Walther-Meißner-Institut, we had to face the demanding challenges of each component individually. We developed a fabrication procedure such that fabrication steps are not in conflict with each other.
We start the fabrication procedure by cleaning a commercial highly resistive $6 \times 10\,\mathrm{mm}^2$ silicon substrate in an ultrasonic bath (Martin Walther Ultraschalltechnik: Powersonic). In two fabrication steps, the components defined in Sec. 3.1 will be deposited onto the substrate by using a thin film evaporation technique. The two steps differ in the choice of material. While in the first step the deposited components are made out of gold, in the second step all aluminium components are deposited.
After the deposition, the mechanical string-resonators are released by using an isotropic etching process.
In the following we describe the fabrication in detail. For further information all fabrication parameters can be found in the Appendix.

3.2.1 Gold Deposition (Alignment Markers and Contact Pads)

In the first step we fabricate the alignment markers and the contact pads. We coat the chip with photoresist (Allresist AR-P 617.08) and pattern the resist using a NanoBeam Limited nB5 Electron Beam Lithography System. After exposure, the resist is developed in Allresist Ar600-56 for 60 s and then in isopropanol for 120 s. The development is stopped by rinsing the sample with destilled H_2O. As we use a positive photoresist, the development removes the resist where it was exposed to the electron beam. Hence the substrate is covered with an evaporation mask.

In an evaporation chamber we deposit a 4 nm layer of titanium as surfacer and 26 nm of gold on the substrate under ultra high vacuum conditions. With the thin layer of titanium we increase the adhesion of gold on silicon. After evaporation we apply a lift-off process. By putting the sample into aceton and heating it to 70°C, we dissolve the photoresist and thus remove the evaporation mask together with the excess material.

3.2.2 Aluminium Deposition (MW Circuit, SQUIDs, String-Resonators)

After completion of the alignment markers and the contact pads we continue by depositing the electronic circuit elements in one single fabrication step. This includes the transmission-line, the microwave resonators with embedded SQUIDs and the mechanical string-resonators. As explained in section 2.5 one of the key factors in this thesis is the quality of the MW resonators. In Ref. [71] it has been shown that aluminium MW resonators with internal Q factors above a million can be fabricated. In contrast to previous work where niobium MW resonators were used here we use aluminium to avoid dominant loss channels at the SQUID-resonator interface [43]. Also the mechanical string-resonators are fabricated in a pure aluminium process in contrast to previous work where Al-SiN string-resonators have been used. As the mechanical quality and frequency scales with the tensile stress of the string and $\sigma_{\mathrm{Al}} < \sigma_{\mathrm{Al\text{-}SiN}}$ [40] this seems contra intuitive. Though we benefit from a simplified fabrication procedure and better electrical quality. Further when going to mK temperatures the stress is enhanced due to the high thermal expansion ratio of Al on Si as explained in Sec. 2.1. It was recently shown that the quality of such resonators exceeds 100000 at mK temperatures [72].

The fabrication procedure of aluminium deposition is similar to the procedure of gold deposition described in Sec. 3.2.1. The aluminium is deposited onto the substrate which is coated by a photoresist mask in an evaporation chamber under ultra high vacuum conditions. As the step involves the fabrication of Josephson junctions, we need to apply a shadow evaporation technique. This technique has been studied in detail in [40, 65, 73, 74]. In the following we want to sketch the process of shadow evaporation without going deep into detail.
Two aluminium layers with a thin insulating oxide layer in between are evaporated under different angles. The first Al layer has a thickness of 40 nm, the second layer has a thickness of 70 nm and creates an overlap over the first layer.
In Fig. 3.2 d) we show a close-up of the evaporation mask for Josephson junctions in top view. The depicted pattern is written into a double layer system of positive resists using electron beam lithography. The bottom layer consists of very sensitive positive photoresist (Allresist AR-P 617.08), the top layer consists of four times less sensitive positive photoresist (Allresist AR-P 679.02). First, one writes the actual shape of the junction, which is coloured grey in Fig. 3.2 d), with a high exposure dose. The high dose guaranties that both layers become soluble to the photoresist developer. Then the area which is coloured green in Fig. 3.2 d) is written with a small exposure dose which is only 20% of the first dose. The second dose is optimized such that it makes the bottom layer soluble to the photoresist developer but the top layer remains insoluble. When developed, a free standing bridge above an undercut is created.
By evaporating two layers of aluminium under different angles (±17°) nanoscale overlapping

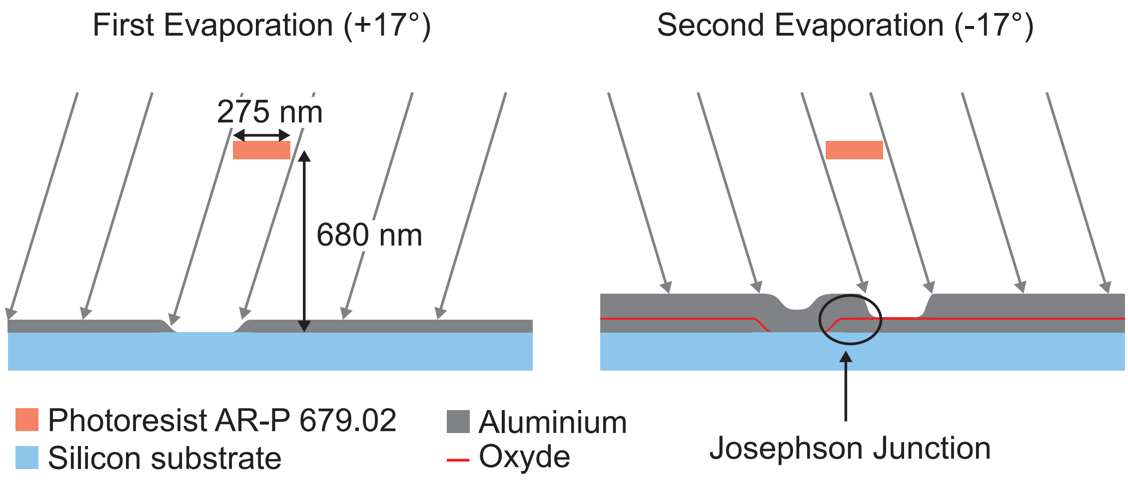

Figure 3.5: Schematic drawing of the shadow evaporation process used to create a Josephson junction. On the left (right) hand side the first evaporation step under an angle of +17° (−17°) is depicted. In red we show the insulating Al_2O_3 layer which separates the aluminium layers. The Josephson junction is indicated by a black circle. The overlap area between the aluminium layers is called Josephson junction area.

structures can be created. But before evaporating the second layer which creates the overlap, the first layer is exposed to oxygen so that a thin insulating Al_2O_3 layer is embedded in between the two aluminium layers. In Fig. 3.5 we depict the shadow evaporation process geometrically. The shadow cast of the free standing resist bridge creates a gap in both current conducting aluminium layers. As the two layers are evaporated under different angles the gaps are situated at different positions which implies that the current in one layer has to change over to the other layer. The oxidized interface between the two aluminium layers where the transition takes place can be associated as Josephson junction and is marked by a black circle in Fig. 3.5.
To sum up, the presence of Josephson junctions demands for the shadow evaporation technique on a double layer resist. We evaporate all current conducting structures in one fabrication step expecting a significant increase in electrical quality factors compared to [40] where the MW resonators consist of niobium and loss channels exist at the Al-Nb interface [43].
After the evaporation, we apply a lift-off process which removes the evaporation mask and all the excess material. The desired structures remain on the chip.
In Fig. 3.6 we show a microscope picture of FTR1 and FTR2 after the lift off.

In order to create a tensile stress in the aluminium nano string the sample is annealed at 350 °C in vacuum for 30 minutes [41] after the deposition.

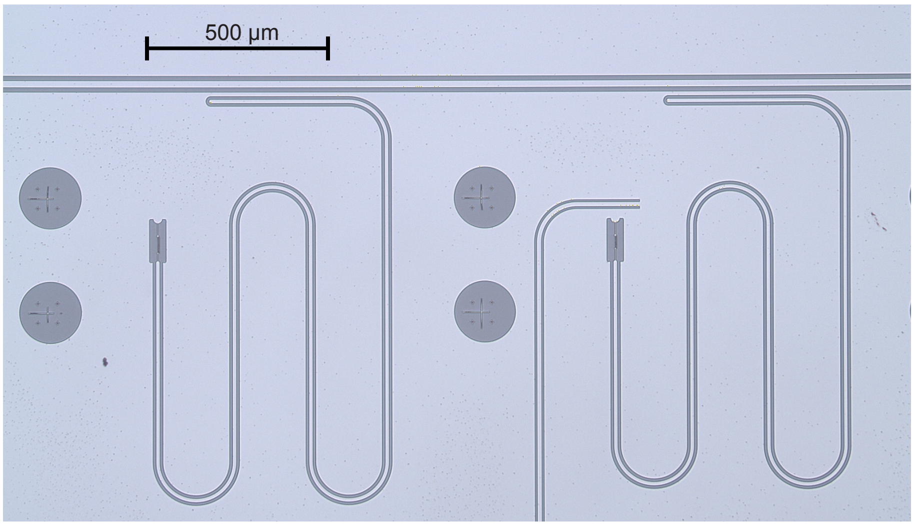

Figure 3.6: Microscope picture of FTR1 and FTR2 on sample IM7-4 after the lift-off process

3.2.3 Release of the Mechanical System

In the last step we release the mechanical string-resonators by underetching one arm of the SQUID loop in a reactive ion etching process (RIE). Two etching recipes have been used. One includes a high acceleration voltage and offers anisotropic etching deep into the substrate, the other one has no acceleration voltage at all, is therefore isotropic and enables us to underetch the aluminium string. From recent work [40] we expected that both processes, the isotropic and the anisotropic one, would be necessary to fabricate a free standing mechanical string-resonator. However, we found out, that the isotropic etching process etches sufficiently deep when applied for a longer period of time. Etching times of 50 minutes showed very good results. By avoiding the anisotropic etching process, one circumvents high acceleration voltages in the etching chamber and so one reduces the risk of destroying the Josephson junctions due to electrostatic discharge. Before the etching, we coat the sample with a mask of photoresist that exposes the nanostrings to the etching while the rest of the sample is protected.

After the actual etching we have to remove the photoresist from the sample. Due to the fact that the mechanical string-resonators are now underetched, they are very fragile and can stick to the bordering walls due to surface tension. The removal of the photoresist is done as in the previous steps by putting the sample into aceton at 70 °C. To avoid residues of photoresist around the nanostring the sample is then rinsed several times with aceton and then with isopropanol. Due to the fragility of the nano strings, the sample cannot be dried with a nitrogen blow. When the liquid vaporizes forces act on the string-resonator due to surface tension. The collapse of nanostructures in the drying process has been studied for example in [75] and can be avoided by reducing the surface tension during the drying process. A suitable approach is to use supercritcal carbon dioxide. Beyond the critical point liquid and vapour states become indistinguishable and the carbon dioxide is in a fourth, supercritical fluid state which has intermediate properties between liquid and gas. In this state an interface between liquid and gas does not exist, which implies that the surface tension equals zero [76]. We exploit this technique by transferring the wet sample into a bath of pure ethanol and then to a fully automatic drying machine called

critical point dryer (Leica EM CPD300). One must take care that the sample is always wetted after removal of the photoresist. The drying then takes place in the critical point dryer as follows:
The CPD replaces the ethanol by CO_2 in several cycles of flooding and gas out phases. The temperature and the pressure are increased to bring the CO_2 into the supercritical phase. At sufficiently high temperature the pressure is then reduced by exhausting the gas. As soon as room pressure is reached, the chamber can be opened and the dry sample can be taken out.
To sum up, by circumventing the critical point in the phase diagram, liquid CO_2 can be vaporized without going through a phase transition and so the surface tension in the drying process is zero, following no forces act on the nanomechanical system leading to a high yield in fabrication.
In Fig. 3.7 we show scanning electron microscope pictures of the aluminium structures after the release of the mechanical string-resonators. In panels a) and b) the underetched test pattern of string-resonators, in panel c) a zoom into the Josephson junctions and in panel d) the complete SQUID where one arm of the SQUID loop is underetched and forms a string-resonator is shown.

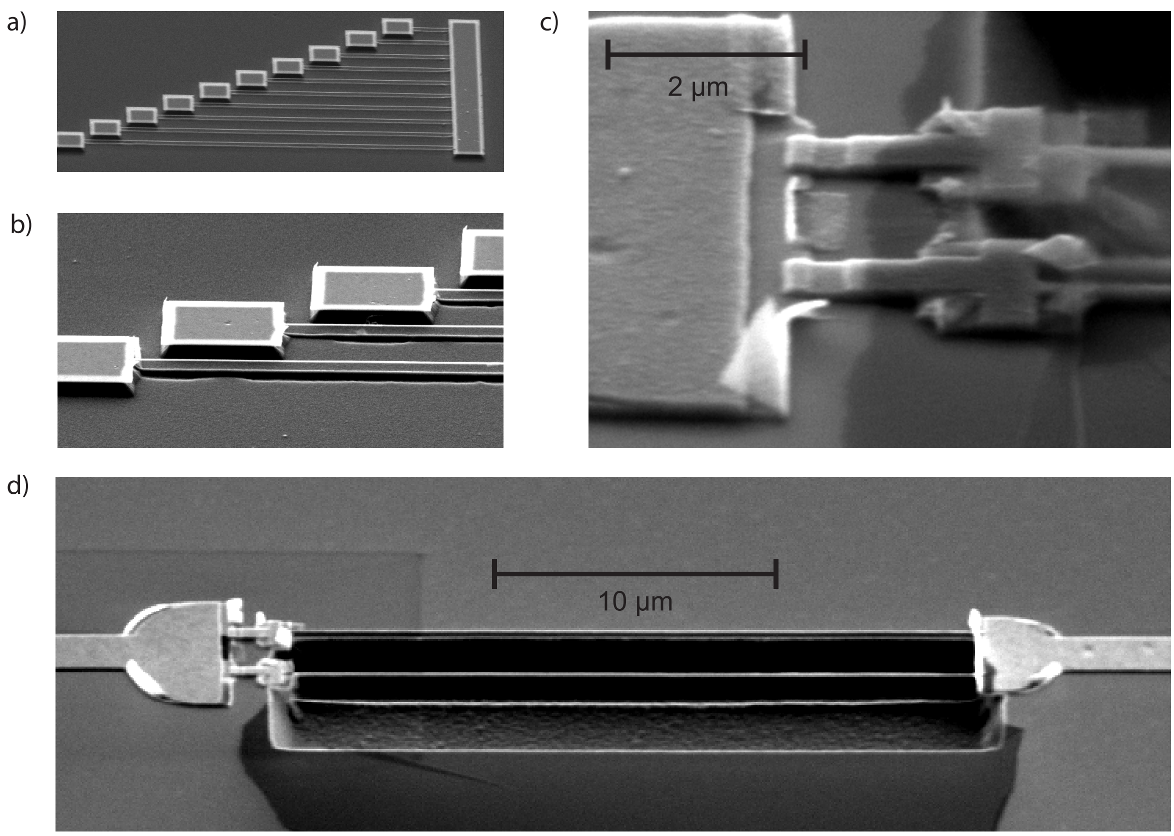

Figure 3.7: Scanning electron microscope pictures of aluminium structures after releasing the mechanical system. In panel a) and b) the underetched test pattern of string-resonators, in panel c) a zoom into the Josephson junctions and in panel d) a complete SQUID where one arm of the SQUID loop is underetched and forms a mechanical string-resonator is shown

3.3 Experimental Setups

For the characterization of the fabricated samples, optical experiments at room temperature, as well as electronic setups at mK temperatures have been used.
In the following we are going to present the experimental setups of the optical interferometer and three cryostats with different performance goals which have been used during this thesis.

3.3.1 Optical Interferometry at Room Temperature

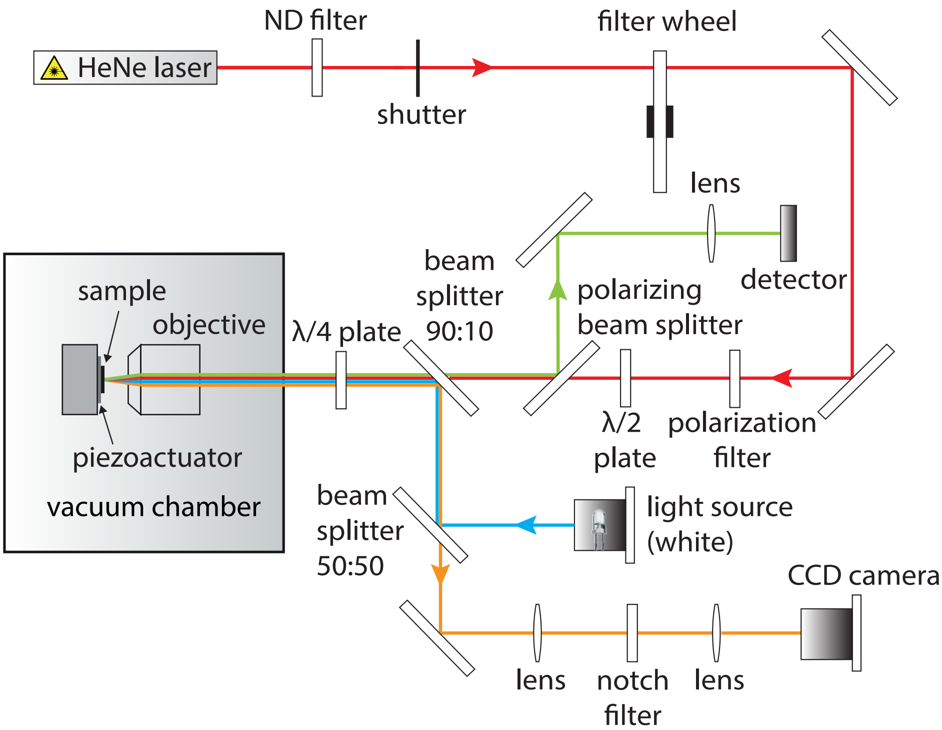

Figure 3.8: Overview of the optical interferometer used to precharacterize nanomechanical strings at room temperature. The sample is mounted in the vacuum chamber, on a piezoactuator which excites mechanical motion of the naostrings. The motion of the nanostrings is readout by detecting the intensity of the reflected laser beam as explained in the text. The positioning of the laser spot on the sample can be observed in-situ via a CCD camera.

For precharacterization of nanomechanical strings an optical Fabry-Pérot interferometer was used. An overview of the setup including all components is depicted in Fig. 3.8. For detailed information on the setup and the working principle of the interferometer please refer to Ref. [40]. In the following we give a brief introduction to the instrument and the measurement method. The sample is mounted onto a piezoactuator and placed in a vacuum chamber which has optical access through a glass window. The piezoactuator is driven by the output voltage U_{drive} of a vector-network-analyser (VNA). The motion of the piezoactuator excites motion of the string-resonators when the resonance condition is met. From a laser source, a beam is guided to the sample and focused by an objective resulting in a laser spot of $\approx 2\,\mu\mathrm{m}$ in diameter. The laser

beam is reflected by the sample and guided to a detector by a polarizing beam splitter. The intensity of the reflected beam is modulated by the vibrations of the mechanical string-resonator due to interference effects. The resulting photo voltage at the detector is fed back into the VNA as input voltage U_{in}.
In general a VNA records the ratio of outgoing power to incoming power $|S_{21}|^2 = P_{\mathrm{in}}/P_{\mathrm{out}}$ where $S_{21} = U_{\mathrm{in}}/U_{\mathrm{out}}$ is the complex scattering parameter. Here the output power drives the piezo actuator and is considered as P_{drive}. During the measurement of one amplitude spectrum, the drive power is constant and the squared amplitude of the scattering parameter is directly proportional to the input power at the VNA: $|S_{21}|^2 \cdot P_{\mathrm{drive}} = P_{\mathrm{in}}$.
As the mechanical amplitude of the string-resonator is proportional to the photovoltage U_{in} [34]:

$$x = c_{\mathrm{calib}} \cdot U_{\mathrm{in}} \,, \tag{3.1}$$

we can fit the squared mechanical amplitude to the measured power spectrum:

$$x^2 = c_{\mathrm{calib}}^2 U_{\mathrm{in}}^2 = c_{\mathrm{calib}}^2 |S_{21}|^2 P_{\mathrm{drive}} = \tilde{c}|S_{21}|^2 \,. \tag{3.2}$$

In Sec. 2.1 we derived the mechanical amplitude spectrum in Eq. (2.3). Further, the squared amplitude including a complex background is given by:

$$x(\Omega)^2 = x_0^2 \left| \frac{\Gamma_{\mathrm{m}}}{i\left(\Omega_{\mathrm{m}} - \Omega\right) + \frac{\Gamma_{\mathrm{m}}}{2}} + ic_1 \right|^2 + c_2 \,. \tag{3.3}$$

By fitting Eq. (3.3) to the measured response spectrum of a string-resonator we can extract its characteristics, including the mechanical resonance frequency Ω_{m}, the linewidth of the resonance peak Γ_{m} and following the quality factor Q_{m}.

By applying this optical spectroscopy method we are able to identify immediately if a string-resonator is broken or sticks to the substrate.

3.3.2 500 mK Cryostat

The 500 mK cryostat is used to precharacterize SQUIDs in four-terminal sensing. The sample stick of the cryostat contains 8 pairs of twisted dc cables which enable us to measure 4 independent SQUIDs in one cooldown. Additionally we have mounted a superconducting coil on top of the sample holder in order to study the SQUIDs response to externally applied magnetic field.
For the measurements we need to reach the mK regime, so cooling with ^{4}He evaporation which only reaches a temperature of typically 1.3 K is not sufficient [77]. The cryostat used here reaches a temperature of 500 mK by ^{3}He evaporation cooling. The sample is placed inside of a closed pot which is filled with ^{3}He. The ^{3}He pot is pre-cooled by liquid ^{4}He to 4.2 K, then it is isolated from the bath. With a Joule-Thomson-cooler the temperature in the pot is reduced to 1.5 K and the ^{3}He condenses. Slowly the liquefied ^{3}He evaporates and cooles the sample stage further until it reaches its base temperature of 500 mK. For further information on the working principle please refer to Ref. [77].

With the help of this cryostat we can check if the critcal current of the fabricated SQUIDs matches the expected value.

3.3.3 20 mK Cryostat ("Kermit" and "Triton")

For characterization of the MW circuits we used two cryostats which allow the connection of MW lines to the sample. They are called "Kermit" and "Triton" and can reach temperatures of about 20 mK. Both cryostats are dilution fridges based on the principle that a ^{4}He/^{3}He-mixture undergoes a spontaneous phase separation at ≈ 800 mK. A forced phase transition from the concentrated ^{3}He phase to the diluted phase in the mixing chamber absorbs the mixing heat from the environment [77]. The base temperature of the cryostats is limited by heat channels like MW cables which act as thermal conductor from room temperature into the fridge. Additionally during the measurement the cryostats are heated by the power of the measurement signal. Typical temperatures during the experiments were around 100 mK.
While "Kermit" must be pre-cooled with liquid nitrogen and liquid helium and the gas handling which controls the ^{4}He/^{3}He mixture must be operated by hand, the "Triton" is a fully automatized cryogen free fridge where the ^{4}He/^{3}He mixture is precooled by commercial pulse tube coolers. The latter one runs very stable and is suitable for long term measurements. It is typically operated for longer than 2 weeks what makes quick sample exchange difficult.
For a quick analysis of a new sample we therefore typically use the "Kermit" fridge which has a cycle time of a few days. During this thesis, we exchanged the mixing chamber of the "Kermit" cryostat which had a leak. The "Triton" cryostat was out of order for several months due to renovation work at the lab.
The microwave wiring inside of the cryostats is depicted schematically for "Triton" including all MW components in Fig. 3.9. The wiring in "Kermit" is similar and not depicted.
In "Triton" the sample is placed in the sample chamber at the 50 mK stage. It is shielded from external magnetic fields by μ-metal and superconducting shields. The transmission line of the sample is connected to the input and output lines. The antennas of the sample are connected to the pump line for additional magnetic flux pumping. The input lines lead a MW signal from room temperature to the sample at the 50 mK stage, so in order to avoid thermal noise at the sample the signal is attenuated at each temperature stage. For "Triton" the signal attenuation has been calibrated in Ref. [72]. Considering attenuators along the input line and the attenuation due to losses in the MW cables one finds a total attenuation of 53.5 dB. In "Kermit" the signal attenuation along the input is line bigger and the total attenuation is about 70 dB.
The output signal passes through circulators which avoid the intrusion of thermal noise on the output line and is amplified by a HEMT amplifier (LNF-LNC4_8A) which adds thermal noise of 2 K at the 4 K stage.
Additionally, the setup contains several dc-cables which are used for temperature sensors at each temperature stage and for a superconducting coil which is mounted on top of the sample box in order to apply magnetic field to the sample.
The wiring outside of the cryogenic differs from experiment to experiment. For the characterization of FTRs one needs a current source in order to apply magnetic fields and a VNA which records the power transmission spectrum through the sample. The VNA has been connected

to the input and output lines of the cryostat depicted in Fig. 3.10 by MW cables (TrueBlue: 262-0248-1000 and 90-221-5MTR). The current source which has been used to apply the current to the superconducting coil was a YOKOGAWA GS200. For the detection of electromechanical interaction we apply the methods of single tone and two-tone spectroscopy with the MW wiring depicted in Fig. 3.10.

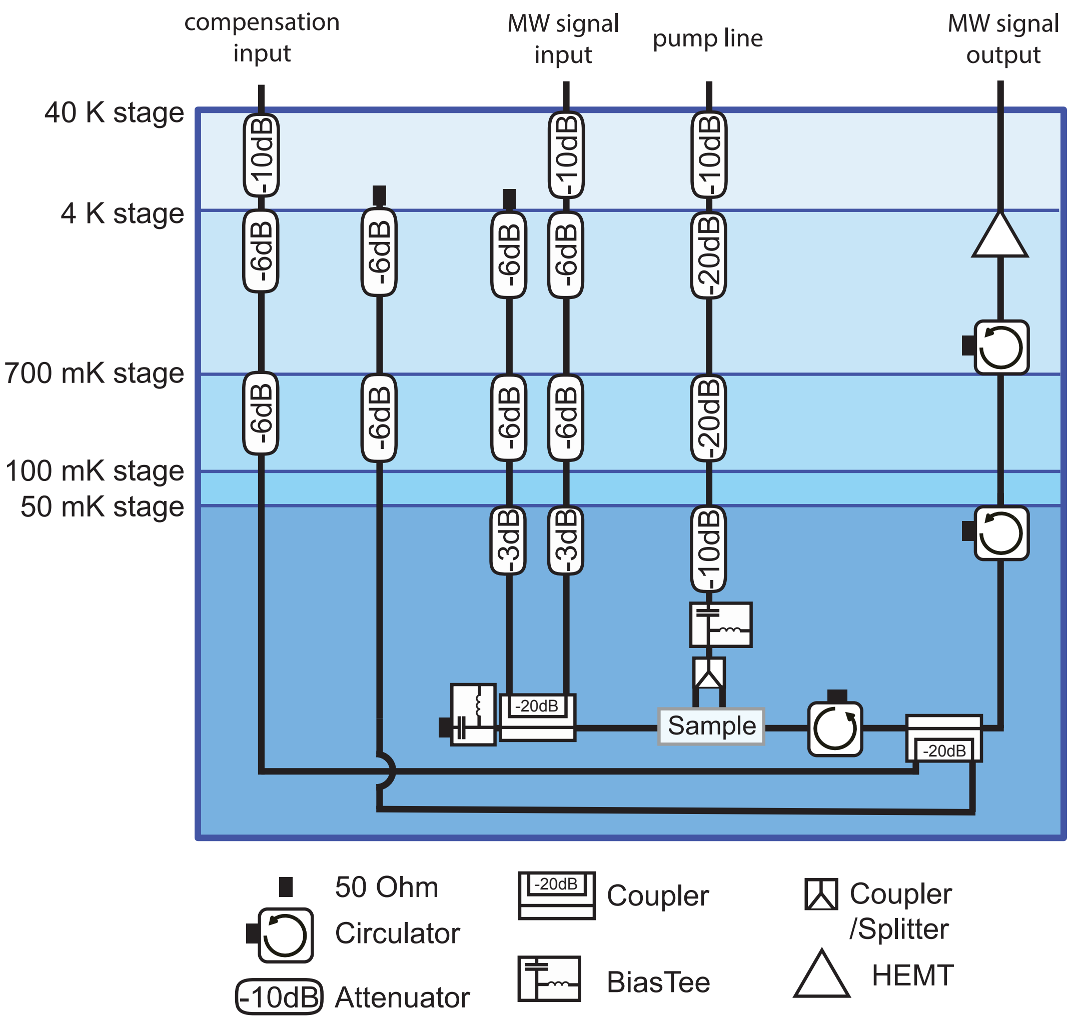

Figure 3.9: Schematic overview of MW wiring in the ”Triton” cryostat. Temperature decreases from top to bottom. The sample is connected from input to output line to perform transmission measurements. Additionally two antennas of the sample are connected to a pump line for magnetic flux pumping. To avoid thermal noise, the input lines are attenuated, while the output signal passes through circulators and is amplified by a HEMT amplifier before reaching room temperature again. The compensation line was not used during this thesis but is shown for completeness.

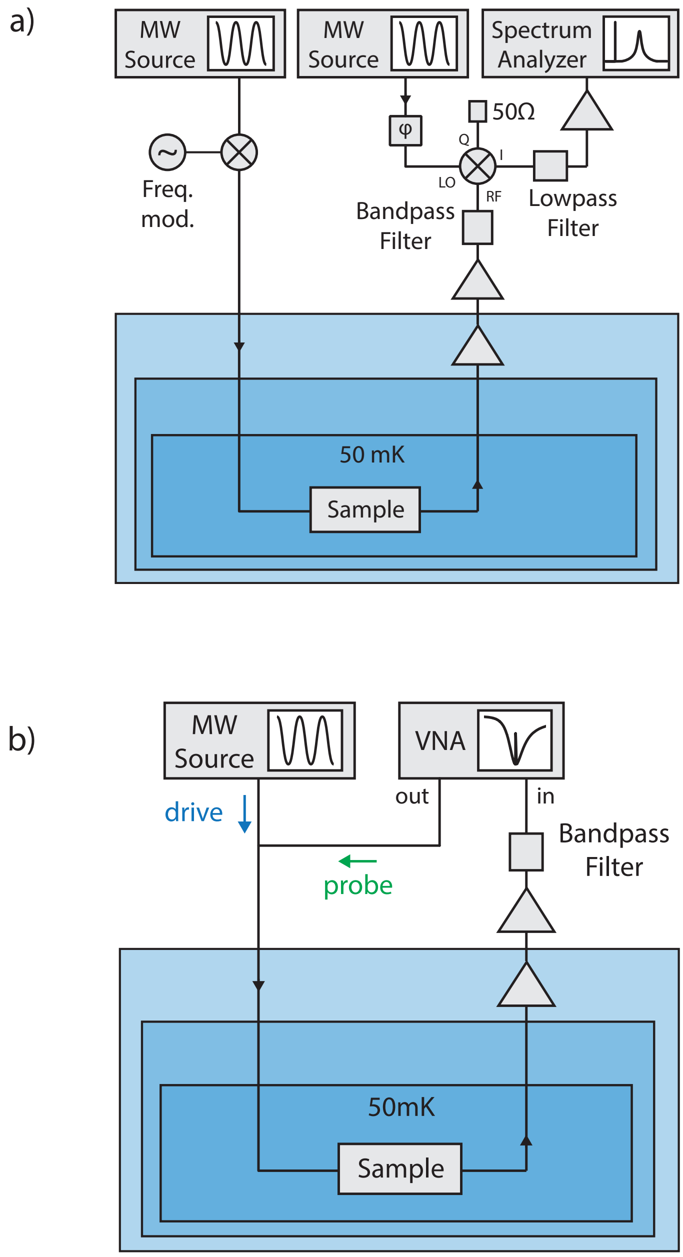

Figure 3.10: MW wiring outside of the cryogenic environment for the detection of electromechanical interaction. The setups for single tone and two tone spectroscopy are shown in panels a) and b) respectively. Picture taken from Ref. [41].

Chapter 4

Characterization of the Nanomechanical Hybrid Sample

In this chapter we present experimental results obtained on electro-mechanical hybrid samples which we have fabricated according to Sec. 3.1. The samples consist of three main components. These are mechanical string-resonators, superconducting MW resonators and SQUIDs. In order to realize the inductive coupling all three components must be functional and matched up to each other. We show measurements on the individual parts as well as on the embedded system. With the results from precharacterizations, the parameters of the system have been optimized. We successfully fabricated a final device where all necessary components are functional. Detection of the inductive coupling however remains open.

4.1 Precharacterization of Mechanical String-Resonators at Room Temperature

First, the mechanical string-resonators on sample IM5-2 are characterized at room temperature using optical interferometry as depicted in Sec. 3.3.1.
We have shown in Sec. 3.3.1 that the power spectrum recorded by the VNA is directly proportional to the squared amplitude spectrum of the mechanical string-resonator. To determine the figures of merit for our inductive coupling, i.e. the resonance frequency Ω_m and the mechanical linewidth Γ_m, we do not require to calibrate the amplitude of the mechanical motion. However, we demonstrate the calibration procedure exemplarily for one string using the duffing nonlinearity, as described in Refs. [34, 40]. The calibrated data will reveal the absolute displacement of the string resonator.
We have recorded the power transmission spectra of several string-resonators with lengths ranging from $15\,\mu$m to $100\,\mu$m. By fitting the amplitude spectra with Eqs. (3.2) and (3.3) we extract Ω_m and Γ_m for each string, as we have shown this in Fig. 4.1 a) exemplarily for a string of $l_\mathrm{string} = 25\,\mu$m. The characteristic values of all strings are displayed in Tab. 4.1. The values in the upper part of the table correspond to strings which are situated in a test array next to the actual electrical circuit. They have been used to optimize the fabrication process during this

thesis. Additionally they are characterized to determine σ_{Al}. The values in the lower part of the table correspond to strings which are embedded into SQUIDs for further measurements via inductive coupling. We note here that the fabrication of string-resonators inside of the SQUID geometry is much more challenging due to the constraints in space. Furthermore, during the electron beam lithography the surrounding structures influence the embedded strings due to proximity effects. The quality factors range from 3700 to 10500. Unfortunately two of the

position on sample IM5-2		l_{string} (μm)	$\Omega_{\mathrm{m}}^{\mathrm{RT}}/2\pi$ (MHz)	$\Gamma_{\mathrm{m}}/2\pi$ (Hz)	Q_{m}
test array		20	7.0277	1880	3700
		30	4.4523	620	7200
		40	3.2499	385	8400
		50	2.5793	246	10500
		60	2.1541	253	8500
		70	1.8077	287	6300
		80	1.5359	336	4600
		90	1.3625	254	5400
		100	1.2039	175	6900
embedded into	FTR3	15	8.4427	22000	158
	FTR2	25	5.2672	554	9500
	FTR1	40	3.5102	50000	168

Table 4.1: Resonance frequency, linewidth and quality factor of double clamped string resonators on sample IM5-2. The values are extracted from transmission spectra measured at room temperature at a drive power of $-18\,\mathrm{dBm}$. The upper part of the table corresponds to strings which are situated in a test array next to the actual electrical circuit (compare Fig. 3.4). The lower part of the table corresponds to strings which are embedded into SQUIDs and can be further utilized for measurements on inductive coupling. One of them shows a very small linewidth and following excellent quality while the other two are worse.

embedded strings have low quality factors. We assume that due to the small area of the etching windows, remains of photoresist from the etching mask damp the mechanical motion.
However, the sample IM5-2 has three vibrating embedded string-resonators and will be further characterized.
We plot the resonance frequency over the length of the string-resonators in Fig. 4.1 b) and fit the data with Eq. (2.1) in order to extract the pre-stress σ_{Al} at room temperature yielding $\sigma_{\mathrm{Al}} = (187 \pm 5)\,\mathrm{MPa}$.

In Fig. 4.1 b) we observe a small deviation from the fit for long strings. We conclude that these strings have less stress then the short ones.

Now we calibrate the actual amplitude of the strings motion x_0 to the measured photovoltage U_{in}. Therefore we analyse the duffing behaviour of one string-resonator. We choose the string of length $l = 25\,\mu\mathrm{m}$ which is embedded into FTR2 and shows a quality factor of 9500.
At high drive powers, the response spectrum of the string-resonator becomes non-linear and the maximum shifts to higher frequencies with a sharp cut off, taking the shape of a shark fin. Spectra of the string for different drive powers are depicted in Fig. 4.2 a). The critical amplitude

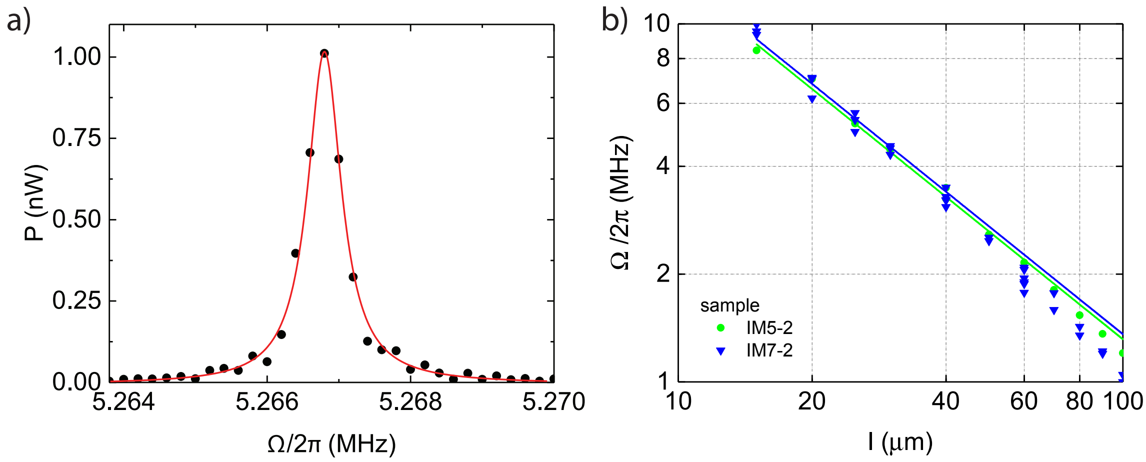

Figure 4.1: Mechanical properties of double clamped string-resonators on sample IM5-2 and sample IM7-2. a) Power transmission spectrum of a 25 μm long string-resonator at a drive power of -18 dBm. The Lorentzian fit according to Eq. (3.3) yields $\Omega_\mathrm{m}/(2\pi) = 5.2668$ MHz and $\Gamma_\mathrm{m}/(2\pi) = 554$ Hz. b) Double logarithmic plot of resonance frequency vs. length for several string-resonators on two different samples with lengths ranging from 15 μm to 100 μm. The fit according to Eq. (2.1) yields $\sigma_\mathrm{Al} = (187 \pm 5)$ MPa for sample IM5-2 and $\sigma_\mathrm{Al} = (200 \pm 5)$ MPa for sample IM7-2.

of the motion at the cut off frequency is connected to the frequency shift as shown in Refs. [34, 40]:

$$x_\mathrm{c}^2 = \frac{8}{3}\frac{\Omega_m m_\mathrm{eff}}{\alpha}\left(\Omega_\mathrm{eff} - \Omega_\mathrm{m}\right) , \tag{4.1}$$

with $\alpha = m_\mathrm{eff}\pi^4 E_\mathrm{Al}/(4l^4\rho_\mathrm{Al})$ the duffing parameter.
We replace the critical amplitude by $x_\mathrm{c}^2 = U_\mathrm{c}^2 \cdot c_\mathrm{calib}^2$ and solve for the calibration constant:

$$c_\mathrm{calib} = \left(\frac{U_\mathrm{c}^2}{\Omega_\mathrm{eff} - \Omega_\mathrm{m}}\frac{3\alpha}{8\Omega_\mathrm{m} m_\mathrm{eff}}\right)^{-1/2} . \tag{4.2}$$

The slope $U_\mathrm{c}^2/(\Omega_\mathrm{eff} - \Omega_\mathrm{m}) = 1.457 \pm 0.066 \cdot 10^{-9}\,\mathrm{V}^2/\mathrm{Hz}$ can be determined by plotting the critical voltage over the cut-off frequency as shown in Fig. 4.2 b). Inserting all values into Eq. (4.2) results in $c_\mathrm{calib} = 2.442$ nm/mV.
With the calibration constant we calibrate the measured amplitude spectra and show the actual displacement of the string-resonator in nanometer on the right vertical axis of Fig. 4.2 a).
We see in Fig 4.2 a) that by applying moderate drive powers slightly below the onset of the non-linearity, the string-resonator can be excited to amplitudes around 2 nm which corresponds to 40 000 zero point fluctuations. As the flux modulation scales with the displacement of the string-resonators, it could be significantly increased by mounting a piezo actuator into the cryogenic environment.

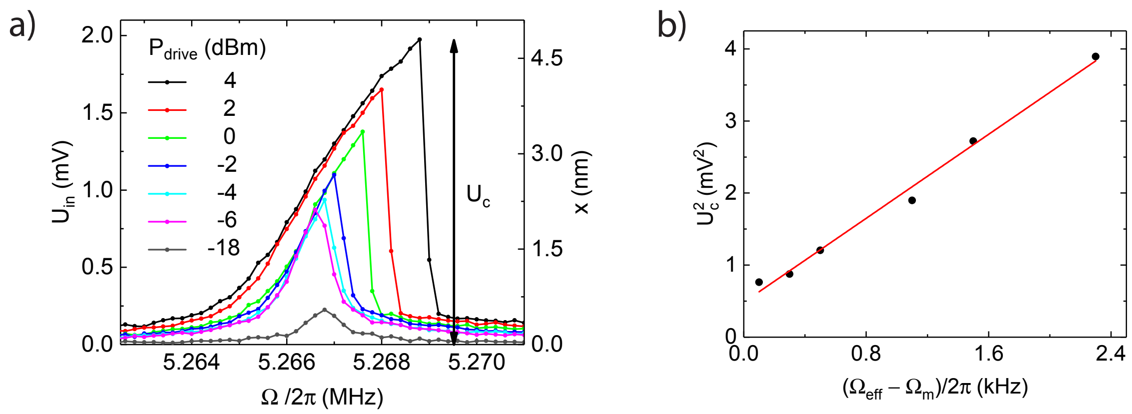

Figure 4.2: Analysis of an embedded string-resonator of length $l_{\mathrm{string}} = 25\,\mu\mathrm{m}$ in the non-linear duffing regime for several drive powers ranging from $-6\,\mathrm{dBm}$ to $4\,\mathrm{dBm}$. a) With increasing drive power the amplitude spectra become non-linear and take the form of a shark fin. The amplitude of the strings motion is calibrated as explained in the main text. b) Squared critical voltage of each shark fin plotted over the cut-off frequency. A linear fit yields the slope which can be inserted into Eq. (4.2) in order to determine the calibration constant which relates voltage and amplitude.

From an experimental perspective, Ω_{m} is temperature dependent. The optical measurements of Ω_{m} presented above are performed at room temperature and are not possible in cryogenic environments. Therefore in the following we estimate $\Omega_{\mathrm{m}}^{\mathrm{mK}}$ at mK temperature.

When exposed to a temperature change dT a material expands or contracts due to thermal expansion. The amount is given by the temperature dependent thermal expansion coefficient $\alpha(T)$ of the material. Here, however, the nanostring is fixed to the substrate at both clamping points resembling a boundary condition. If the nanostring contracts stronger than the substrate, stress is induced in the nanostring. According to Ref. [78] the stress in an aluminium thin film on a silicon substrate can be resolved into an intrinsic component σ_{Al} and a thermal component σ_{th}:

$$\sigma = \sigma_{\mathrm{Al}} + \sigma_{\mathrm{th}}\,. \tag{4.3}$$

We assume that the derivations from Ref. [78] are equally valid for continuous thin films and geometrically shaped structures.

Then, in our case the intrinsic stress is the measured stress of the double clamped aluminium string-resonator at room temperature which has been induced in the system by the annealing. The thermal stress for an infinitesimal change in temperature is given by [78]:

$$d\sigma_{\mathrm{th}} = \frac{E_{\mathrm{Al}}}{1-\nu_{\mathrm{Al}}}\left(\alpha_{\mathrm{Al}}(T) - \alpha_{\mathrm{Si}}(T)\right) dT\,, \tag{4.4}$$

with $E_{\mathrm{Al}} = 70\,\mathrm{GPa}$ [33] the Young's Modulus of aluminium and $\nu_{\mathrm{Al}} = 0.345$ [78] the Poisson's ratio of aluminium.

Integrating this equation over the range of temperature change yields the thermal stress σ_{th}

$$\sigma_{\mathrm{th}}(T) = \frac{E_{\mathrm{Al}}}{1-\nu_{\mathrm{Al}}}\left(\frac{\Delta l_{\mathrm{Al}}}{l_{\mathrm{Al}}} - \frac{\Delta l_{\mathrm{Si}}}{l_{\mathrm{Si}}}\right)\,, \tag{4.5}$$

where $\int_{293}^{T} \alpha_{\mathrm{i}}(T')dT' = \Delta l_{\mathrm{i}}/l_{\mathrm{i}}$ the relative change of length for both materials was introduced. We note that Eq. (4.5) is particularly independent of the length of the string-resonator. Furthermore we considered the string-resonator due to its dimensions (long and thin) as a one dimensional object. Following, geometric contributions as the exact shape of the string design do not contribute in Eq. (4.5).
Thermal expansion at low temperatures has been studied in literature [79]. We present the temperature dependent expansion coefficients of aluminium and silicon and the resulting thermal stress in Fig. 4.3:

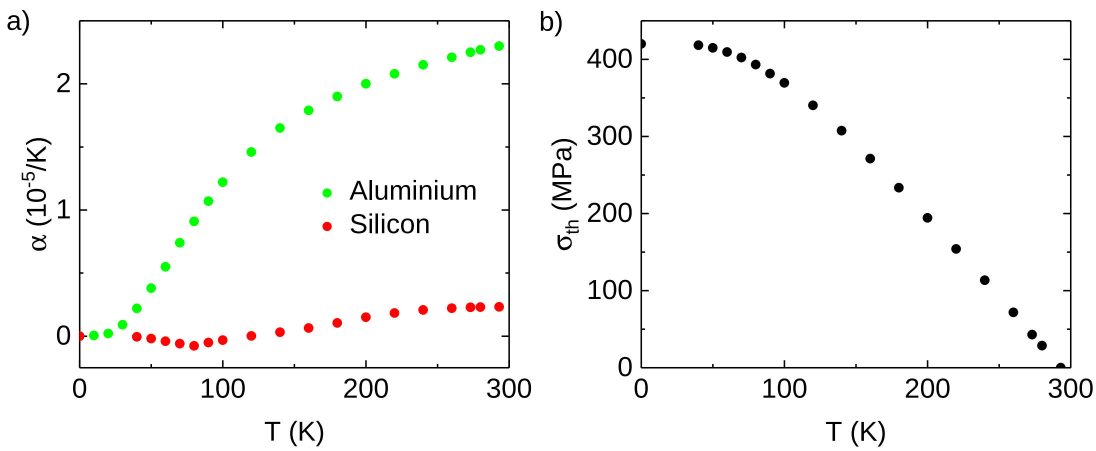

Figure 4.3: a) temperature dependent thermal expansion coefficients $\alpha(T)$ of aluminium and silicon and b) Thermal stress of a doubly clamped aluminium string-resonator on a silicon substrate when cooled from room temperature to a few mK, according to Eq. (4.5). The thermal expansion coefficients $\alpha_{\mathrm{i}}(T)$ and the resulting relative changes of length $\Delta l_{\mathrm{i}}/l_{\mathrm{i}}$ for both materials are taken from Ref. [79].

The additional stress induced by cooling the sample from room temperature to mK temperatures is:

$$\sigma_{\mathrm{th}} = \frac{E_{\mathrm{Al}}}{1-\nu_{\mathrm{Al}}}\left(\frac{\Delta l_{\mathrm{Al}}}{l_{\mathrm{Al}}} - \frac{\Delta l_{\mathrm{Si}}}{l_{\mathrm{Si}}}\right) = \frac{70\,\mathrm{GPa}}{1-0.345}\cdot 3.93\times 10^{-3} = 420\,\mathrm{MPa}\,. \tag{4.6}$$

In Ref. [41] the thermal stress for an equivalent string-resonator has been determined experimentally to be $\sigma_{\mathrm{th}} = 407\,\mathrm{MPa}$. The calculation agrees well with the experimental result from Ref. [41] and allows us to estimate $\Omega_{\mathrm{m}}^{\mathrm{mK}}$ with Eq. (2.1) by assuming a total stress $\sigma_{\mathrm{Al}}^{\mathrm{mK}} = \sigma_{\mathrm{Al}}^{\mathrm{RT}} + \sigma_{\mathrm{th}} = 607\,\mathrm{MPa}$. We show the estimates in Tab. 4.2.

length (μm)	$\Omega_m^{RT}/2\pi$ (MHz)	$\Omega_m^{mK}/2\pi$ (MHz)
15	8.4427	15.8
25	5.2672	9.5
40	3.5102	5.9

Table 4.2: The resonance frequencies of embedded string-resonators have been determined at room temperature with an optical interferometer. When the sample is cooled down to mK temperatures additional stress is induced due to thermal contraction as explained above. The resonance frequency at mK temperatures is calculated with Eq. (2.1) for an estimated total stress of $\sigma_{Al}^{mK} = 607\,\mathrm{MPa}$.

4.2 Precharacterization of SQUIDs

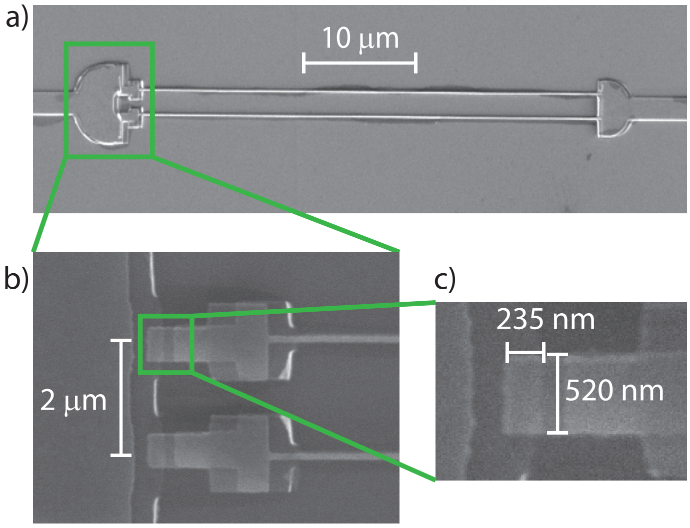

Figure 4.4: Scanning electron microscope picture of a fabricated aluminium SQUID on a silicon substrate. From panel a) to c) the detail level increases. a) Overview of the complete SQUID including the SQUID loop and the Josephson junctions. b) Josephson junctions at the ends of the SQUID loop arms. Both aluminium layers from the shadow evaporation process are visible. c) Detailed zoom into one Josephson junction. Hight and width of the junction area are indicated.

Besides mechanical string-resonators, we have precharacterized the behaviour of SQUIDs. When embedded into a MW resonator they act as a non-linear tunable inductance and define the flux-tunability of the FTR. In Sec. 2.3 we have highlighted the important parameters which need to be optimized in order to realize measurements on inductive coupling. In particular, the critical current is the most important parameter as it defines the frequency tuning and hence the coupling strength.

In Fig. 4.4 we show a scanning electron microscope picture of a SQUID with increasing detail level from panel a) to panel c).

In this section we analyse the parameters of the SQUIDs (Sq5,...,Sq8) on different samples in the 500 mK cryostat in dc-configuration.

We will present an overview of the critical currents on three samples in Tab. 4.3 and a detailed

analysis of all parameters for Sq5, Sq6 and Sq7 on sample IM3-4 in Tab. 4.4.
The properties of our SQUIDs are measured by recording U-I characteristics with four-terminal sensing technique. The SQUID is biased with a current from a current source and we measure the voltage drop across it. We show exemplary measurement data of a U-I characteristic for a SQUID of string length $l_{\text{string}} = 25\,\mu\text{m}$ on sample IM3-4 in Fig. 4.5 a).
Starting from zero current, the SQUID is in the superconducting "zero voltage" state. At the maximum supercurrent I_s^m the SQUID switches into the normal conducting "voltage" state with a gap voltage U_g and a normal resistance R_n. Where $E_g = eU_g$ corresponds to the necessary energy to break up cooper pairs. When reducing the current back to zero one observes a hysteretic behaviour. The SQUID switches back into the "zero voltage" state at a retrapping current $I_r < I_s^m$, which shows that the SQUID is underdamped ($\beta_c > 1$). In Sec. 2.3 we have

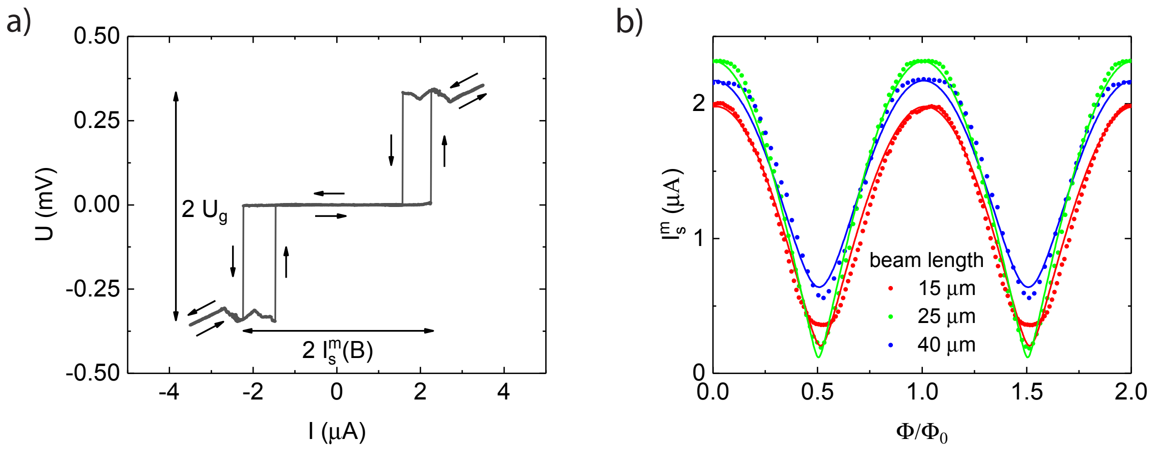

Figure 4.5: Examplary measurement data obtained by characterization of SQUIDs in four-terminal sensing. In panel a) we show the U-I characteristic of a single SQUID. Arrows indicate the sweep direction of the bias current. At the maximum supercurrent I_s^m, the SQUID switches into the "voltage" state. Hysteretic behaviour indicates that the Josephson junctions are underdamped. From the data we extract the gap voltage U_g and the normal resistance R_n. In panel b) we show the magnetic flux dependence of the maximum supercurrent for three different SQUIDs on sample IM3-4 with the same junction area but different loop areas. Fitting Eq. (2.26) to the data yields the critical current I_c as well as the asymmetry factor α_I.

derived that the maximum supercurrent through a SQUID is flux dependent. Recording the flux dependence of our SQUIDs was done by applying external magnetic flux via a coil. At each flux point the maximum supercurrent was extracted. This behaviour is shown in Fig. 4.5 b) exemplarily for three different SQUIDs of sample IM3-4. By fitting the data with Eq. (2.26) we determine the critical current of a single Josephson junction I_c as well as the asymmetry parameter α_I. We note that both parameters β_L and α_I reduce the modulation depth of the maximum supercurrent. Whereas in literature it is usually assumed that either α_I or β_L is negligible, here both quantities are significant and self consistent numerical simulations for each flux point would be necessary in order to obtain both parameters simultaneously [48].
We can however use the experimental data to give an upper limit for both quantities by determining one under the assumption that the other one is negligible, and vice versa.

By fitting Eq. (2.26) to Fig. 4.5 b) we have already determined α_{I} for $\beta_{\mathrm{L}} = 0$. Additionally we determine β_{L} from the modulation depth $\Delta I_{\mathrm{s}}^{\mathrm{m}} = (I_{\mathrm{s}}^{\mathrm{m}}(0) - I_{\mathrm{s}}^{\mathrm{m}}(\Phi_0/2))$ by neglecting the influence of α_{I} as shown in Ref. [48].
Both results are presented in Tab. 4.4 and compared to the theoretic value of β_{L} calculated from I_{c} and L_{loop}.

The performance goal for our SQUIDs is a high critical current with $\beta_{\mathrm{L}} \ll 1$. The loop inductances calculated in Sec. 3.2.2 suggest that critical currents around $I_{\mathrm{c}} = 2\,\mu\mathrm{A}$ optimize all SQUIDs on the sample. Fabrication procedures from previous work [40, 74] have shown that critical current densities in the order of $I_{\mathrm{c}}/A_{\mathrm{JJ}} \approx 350\,\mathrm{A/cm^2}$ are typically achieved, resulting in a necessary Josephson junction width of $w_{\mathrm{JJ}} = 2\,\mu\mathrm{m}$. After fabrication of the first samples however, it turned out that under present fabrication conditions the critical current density is higher. We have observed critical current densities of $I_{\mathrm{c}}/A_{\mathrm{JJ}} = 977\,\mathrm{A/cm^2}$, $I_{\mathrm{c}}/A_{\mathrm{JJ}} = 606\,\mathrm{A/cm^2}$ and $I_{\mathrm{c}}/A_{\mathrm{JJ}} = 755\,\mathrm{A/cm^2}$ on three different samples. We therefore have reduced the critical current by reducing the width of the Josephson junctions. We show an overview of the measurement results in Tab. 4.3. We note that on sample ST3 only Sq7 and on sample IM3-1 only Sq5 were functional. These SQUIDs have different loop inductances, so we can not compare them with respect to the β_{L} parameter. Therefore we assume that all SQUIDs on each of these two samples have the same critical current and calculate β_{L} in Tab. 4.3 for Sq8. This SQUID has the the biggest loop inductance and gives an upper limit to the acceptable critical current.

sample-SQUID	w_{JJ} (μm)	A_{JJ} (μm^2)	I_{c} (μA)	J_{c} (A/cm^2)	β_{L}
ST3-Sq7	2	0.55	5	977	2.23
IM3-1-Sq5	2	0.55	3.1	606	1.39
IM3-4-Sq(5,6,7)	0.5	0.143	1.08 ± 0.12	755 ± 84	0.48

Table 4.3: Parameters of SQUIDs on three different samples. The width of the Josephson junctions w_{JJ} and the resulting junction area A_{JJ} are design parameters, the critical current is experimentally determined from U-I characteristics as explained in the main text. Under present fabrication conditions the critical current density is higher than expected from previous work and fluctuates in between different samples. We successfully reduced the critical current to $I_{\mathrm{c}} = 1\,\mu\mathrm{A}$ by reducing the Josephson junction area on sample IM3-4. β_{L} is calculated for Sq8 on each sample by using the experimentally determined value of I_{c}.

Although all samples have been fabricated with the same fabrication parameters, the critical current density fluctuates in between different samples by $\pm 25\,\%$. At a critical current of $I_{\mathrm{c}} = 1\,\mu\mathrm{A}$, the screening parameter β_{L} is smaller than 0.5 for all SQUIDs. Therefore the junction width of sample IM3-4 seems to be reasonable and we chose to fabricate future samples just like that. With the reduction of the junction width, the yield on sample IM3-4 has been increased to 3 out of 4 compared to a yield of 1 out of 4 on samples ST3 and IM3-1. For sample IM3-4 we give the averaged value of I_{c} with standard deviation in Tab. 4.3. Further details on the individual SQUIDs are given in Tab. 4.4.

In the following, we explain how the values presented in Tab. 4.4 have been determined.

SQUID	R_n (Ω)	I_c (μA)	U_g (μV)	C_{JJ} (fF)	L_{JJ} (pH)	β_c	α_I	β_L	$\beta_L^{analytic}$
Sq5	128	1.09	350	46	150	2.57	≤ 0.29	≤ 0.35	0.33
Sq6	99	1.16	335	81	137	2.92	≤ 0.05	≤ 0.15	0.19
Sq7	100	0.99	310	58	160	1.80	≤ 0.10	≤ 0.22	0.08

Table 4.4: Detailed analysis of three SQUIDs on sample IM3-4. All presented values except for $\beta_L^{analytic}$ are determined experimentally from dc-measurements as shown exemplarily in Fig. 4.5. All SQUIDs are designed for the same Josephson junction area of $A_{JJ} = 0.143\,\mu\text{m}^2$ but the SQUIDs differ in loop design. We present the normal resistance R_n, the critical current I_c, the gap voltage U_g, the asymmetry parameter α_I and the screening parameter β_L. For comparison $\beta_L^{analytic}$ is calculated using the analytically determined value of L_{loop} from Tab. 3.2 and the experimentally determined values of I_c. The capacitance and inductance of the Josephson junctions and the Stewart-McCumber parameter β_c are calculated using equations presented in Sec. 2.3.

The normal resistance R_n, the critical current I_c, the retrapping current I_r and the gap voltage U_g can be directly extracted from the U-I-characteristic presented examplarily in Fig. 4.5. The β_C parameter is calculated according to the right hand side of Eq. (2.21). We calculate the capacity of the Josephson junction by transforming Eq. (2.21) into: $C_{JJ} = \beta_c\Phi_0/(2\pi I_c R_n^2)$. The Josephson inductance L_{JJ} is calculated according to Eq. (2.29). α_I and β_L are estimated from the fit in Fig. 4.5 as explained in the text above and $\beta_L^{analytic}$ is calculated according to Eq. (2.31).
Now we analyse the results presented in Tab. 4.4.
Even though the SQUIDs are equal in junction area, we observe a small fluctuation in I_c of $\pm 11\,\%$. The gap voltage U_g is a material parameter and independent of the SQUID design. The measured values are in good agreement with the literature value $U_g = 340\,\mu$V [80].
The capacity of the Josephson junctions is comparable to the total capacity of the MW resonators ($C_{JJ}/C_r \approx 10\,\%$), however, when embedded into the MW resonator we do not expect an influence on the resonance frequency, as the electrical field gradient at the position of the SQUID is very low (current anti-node). We use C_{JJ} and the area of the Josephsopn junctions to estimate the thickness of the insulating Al_2O_3 layer by approximating the junction as a plate capacitor. With the permittivity $\epsilon_{Al_2O_3} = 9.3$ [81] the thickness is $d_{Al_2O_3} = \epsilon_0\epsilon_{Al_2O_3}A_{JJ}/C_{JJ} \approx 2\,\text{Å}$.
Last but not least, the analytic value of β_L is within or very close to the upper bound which is set by the experimentally determined value, so the values of L_{loop}, calculated according to Eqs. (2.32) and (2.33) seem reasonable.

To sum up, we have found optimal fabrication parameters for the SQUIDs which can be embedded into our MW resonators. We have reduced the critical current to $I_c = 1\,\mu$A which ensures $\beta_L < 0.5$ for all SQUIDs. The experimentally determined values of β_L are consistent with the analytic values, which proves that the calculated loop inductances are reasonable. In the next section we are going to show the performance of SQUIDs embedded into MW resonators

4.3 Characterization of Flux Tunable Resonators

The last key components in our system are the MW resonators. They act as a cavity for electromagnetic signals and enable the interaction with the mechanics. In the following we are going to analyse their characteristics on three different samples. Samples IM2-4 and IM2-3 have been fabricated with layout #1, simultaneously with exactly the same parameters and are therefore well comparable. Sample IM5-2 has been fabricated later with layout #2 including improvements, e.g. a reduced Josephson junction size as discussed in the previous section.

Resonance Frequency, Linewidth and Q-factor

We characterize the MW resonators by recording power transmission spectra through the transmission line via a VNA. Dips in the spectra correspond to the resonance frequencies of the resonators as explained in Sec. 2.2. A typical power transmission spectrum is depicted in Fig. 4.6.

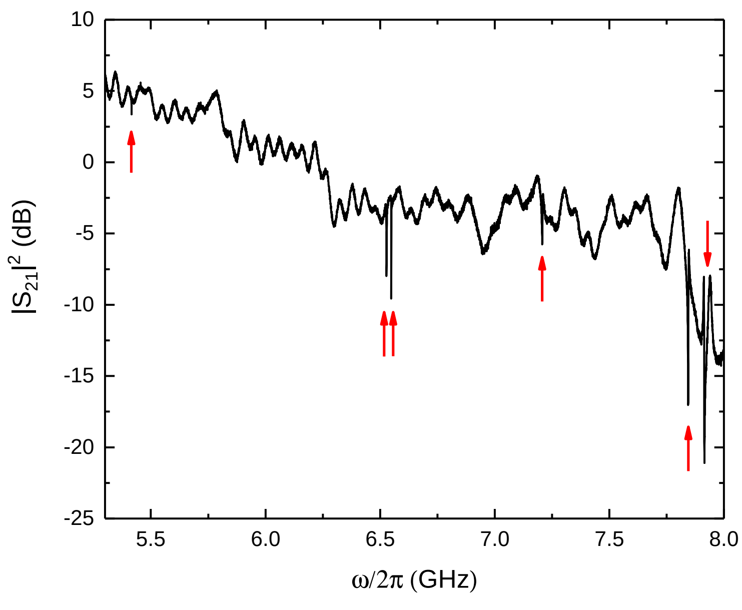

Figure 4.6: Power transmission spectrum of sample IM2-3 in the range between 5.3 and 8.0 GHz. Capacitively coupled MW resonators cause a dip in the spectrum when the frequency of the probe tone matches the resonance frequency of a resonator. Resonance frequencies of all 6 resonators are indicated by red arrows.

In order to provide an overview for the following discussions, we present the resonance frequencies of all measured resonators in Tab. 4.6.

In Chap. 3 we designed 6 MW resonators with different lengths and frequencies according to Eq. (2.8) by assuming an effective dielectric constant $\epsilon_{\text{eff}} = (\epsilon_{\text{Si}} + \epsilon_{\text{vac}})/2 = 6.45$, with $\epsilon_{\text{Si}} = 11.9$ [82]

and $\epsilon_{\mathrm{vac}} = 1$.
In the first step, we analyse the resonance frequencies of bare MW resonators (without SQUID) and determine ϵ_{eff} experimentally as this sets the backbone of our system. We compare the resonance frequencies of MWR1 and MWR2 on three different samples to the theoretically expected values in Tab. 4.5.

resonator	sample	layout	$l_{\mathrm{r,design}}$ (mm)	$\omega^0_{\mathrm{r,design}}/2\pi$ (GHz)	$\omega^0_{\mathrm{r,meas}}/2\pi$ (GHz)
MWR1	IM2-3	#1	5.380	5.485	5.415
	IM2-4	#1	5.380	5.485	5.397
	IM5-2	#2	7.384	4.00	3.995
MWR2	IM2-3	#1	3.741	7.894	7.844
	IM2-4	#1	3.741	7.894	7.848
	IM5-2	#2	3.741	7.894	7.850

Table 4.5: Comparison of theory and experiment. The lengths of MWR1 and MWR2, on layout #1 and #2 as well as the expected resonance frequencies have been defined in Chap. 3 and are reproduced here to simplify reading. We compare the expected to the measured frequencies on three different samples. For the calculation of $\omega^0_{\mathrm{r,design}}$ in Chap. 3 an effective dielectric constant $\epsilon_{\mathrm{eff}} = 6.45$ has been assumed. The results are discussed in the main text.

The resonances of MWR1 and MWR2 appear approximately at the calculated positions. We emphasise that the length of MWR1 differs between layout #1 and #2. The design of MWR2 is identical on both layouts.
On layout #1 we observe for MWR1 a deviation between theory and experiment of $\approx 80\,\mathrm{MHz}$. This deviation is reproducible on samples IM2-3 and IM2-4. On layout #2 the measured resonance frequency of MWR1 matches the theory perfectly.
The measured frequency of MWR2 deviates from the theory by $\approx 45\,\mathrm{MHz}$ on all three samples. The reproducibility of the differences between theory and experiment show, that the deviations arise from uncertainties in the design of the resonator length. A deviation of $1\,\mu\mathrm{m}$ on a length scale of $3\,\mathrm{mm}$ already results in a frequency change of $2\,\mathrm{MHz}$.
Nevertheless we recalibrate the effective dielectric constant ϵ_{eff} for our samples by fitting the measured data from all three samples with Eq. (2.8). The fit yields $\epsilon_{\mathrm{eff}} = (6.54 \pm 0.02)$, which is slightly larger than the theoretic value of $\epsilon_{\mathrm{eff}} = 6.45$. All in all we have shown that we can predict the resonance frequencies of our MW resonators without applying extensive finite element simulation programs. For the following we use the recalibrated ϵ_{eff} and assume that the calculated frequencies of (FTR1,...,FTR4) have a similar precision as shown above for MWR1 and MWR2. The biggest deviation between theory and experiment for the values presented in Tab. 4.5 is $\Delta f/f = 5\,‰$.
Furthermore we mention that $\epsilon_{\mathrm{Si}}(T)$ is temperature dependent. In Ref. [64] a significant temperature dependence of the resonance frequency has been reported. The measurements presented in this section are all taken at the same temperature of $T \approx 100\,\mathrm{mK} \ll T_{\mathrm{c}}$. We therefore do not expect to observe effects of changing temperature in our measurement data.

In the next step, we analyse the quality factors of the resonators. Therefore we have recorded power transmission spectra of each resonator around the resonance. We fit the data with Eq. (2.12), extract κ and calculate the corresponding quality factors at a probe power of $P_{\mathrm{probe}} = -110\,\mathrm{dBm}$. We show exemplarily the power transmission spectrum of FTR1 on sample IM2-4 including the fit according to Eq. (2.12) in Fig. 4.7. Results for all measured resonators are presented in Tab 4.6.

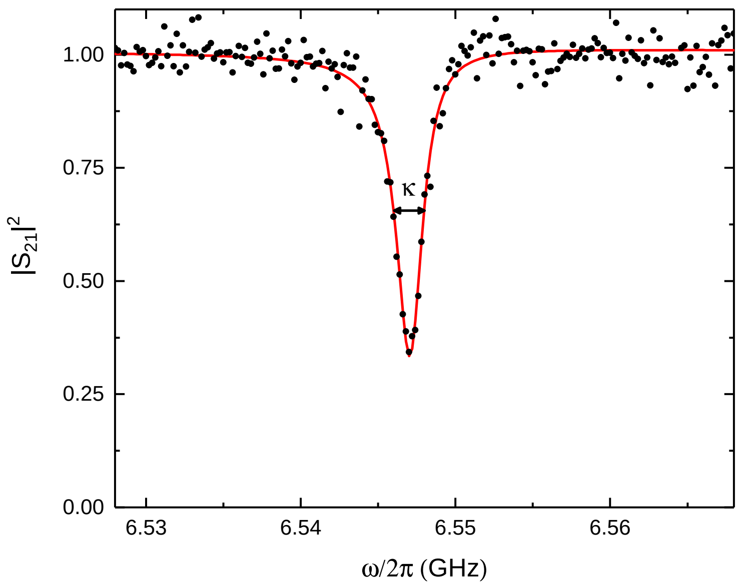

Figure 4.7: Power transmission spectrum of of FTR1 on sample IM2-4 including the fit according to Eq. (2.12). The values of κ presented in Tab. 4.6 correspond to the FWHM of the Lorentzian dip as indicated in the figure.

Quality factors of the resonators vary in a broad range with the best being at about $Q = 11000$ and the worst at $Q = 1500$ (c.f. Tab. 4.6). However, the necessary condition of the resolved sideband regime $\Omega_{\mathrm{m}}^{\mathrm{mk}} > \kappa$ is fulfilled for typical mechanical frequencies in the MHz regime.

Tunability of FTRs

We check if the FTRs are tunable by applying external magnetic flux. We drive a dc-current through a superconducting coil which is mounted on top of the sample box and create a homogeneous magnetic field perpendicular to the sample plane.

The yield of tunable resonators was 0 out of 4 on sample IM2-4 and 1 out of 3 on samples IM2-3 and IM5-2. On both of the two latter samples, we note a lift-off problem in the SQUID loop of FTR4. So these designed FTRs are broken in the sense that the SQUID arms are shorted, omitting the operation of the SQUID. The other ones however show no observable damage and should be tunable. In the following we discuss possible explanations for the non tunability.

	MWR1	FTR1	FTR2	FTR3	FTR4	MWR2
			$\omega_r/2\pi$ (GHz)			
IM2-4	5.397	6.547	-	7.908	6.581	7.849
IM2-3	5.415	6.545	7.206	7.915	6.528	7.844
IM5-2	3.995	6.750	7.060	7.600	6.405	7.850
			$Q/1000$			
IM2-4	5.44	3.19	-	3.21	2.06	4.92
IM2-3	10.99	10.31	2.33	2.52	3.57	4.31
IM5-2	2.10	4.43	3.64	1.9	2.52	1.65
			$\kappa/2\pi$ (MHz)			
IM2-4	0.99	2.05	-	2.46	3.19	1.59
IM2-3	0.49	0.63	3.09	3.14	1.82	1.82
IM5-2	1.90	1.52	1.94	4.0	2.54	4.76

Table 4.6: Resonance frequencies, quality factors and linewidths of all measured resonators on three different samples. Detailed values of κ_{int} and κ_{ext} are given in the appendix.

- The superconducting coil which generates the external magnetic field could be broken
- The electrical connection between MW resonator and SQUID could be damaged
- The SQUID loop could be broken, especially the SQUID arm which is underetched and forms the mechanical resonator
- The Josephson junctions could be damaged (short-cut around the junction or impurities in the insulating layer)

During the first cooldown, where none of the resonators was tunable, we checked whether or not the coil was broken, by ramping up the coil current to strong magnetic fields. We observed the characteristic linewidth broadening of the resonators at high magnetic field and concluded that the coil was functional and the resonators indeed did not respond to the magnetic field.
The fact that the resonators are visible in the transmission spectrum suggests, that the electrical connection from the end of the resonators to the SQUID arms, through the Josephson junctions and onto the ground plane is functional. Otherwise the boundary conditions would shift the frequency to $2\omega_r$. If one of the SQUID arms was broken, this would remove the condition of flux quantization in the SQUID loop and all the current would flow through a single Josephson junction. Investigation of the samples with a scanning electron microscope (SEM) however revealed that all SQUID arms remained in the designed geometry. Furthermore, we can check with the SEM whether or not the junction area looks as depicted in Fig. 4.4 and if there are any short-cuts around the junctions due to remains of aluminium from the lift-off process or broken resist bridges before the aluminium evaporation. The actual thickness of the insulating layer is however not visible, impurities where the insulation may be broken can not be spotted by microscopy and remain as possible issue.
Additionally, the junctions can be destroyed by electrical discharges when applying high electrical fields (e.g. in the etching process or in the SEM). On the contrary, the Josephson junctions of

sample IM2-3 as well as all samples presented in Sec. 4.2 have been investigated with the SEM before the measurements. The fact that many SQUIDs on these samples worked, shows that the Josephson junctions are not destroyed when exposed to an electron beam with 10 keV.

We gain further insight by analysing the resonance frequencies of the FTRs. To facilitate reading we reproduce the resonance frequencies ω_{r}^{0} of all FTRs from Tab. 3.1 and compare them to the measured resonance frequencies from Tab. 4.6) in Tab. 4.7. We remind the reader that in ω_{r}^{0} the influence of the SQUID inductance is not taken into account. The resonance shift $\delta\omega$ from ω_{r}^{0} to the measured ω_{r} allows calibration of the SQUID inductance by transforming Eq. 2.35 into

$$L_{\mathrm{sq}} = \frac{L_{\mathrm{r}}\delta\omega_{\mathrm{r}}}{\omega_{\mathrm{r}}}\,, \tag{4.7}$$

with $\delta\omega_{\mathrm{r}} = \omega_{\mathrm{r,design}}^{0} - \omega_{\mathrm{r,meas}}$.

sample	resonator	$\omega_{\mathrm{r,design}}^{0}/2\pi$ (GHz)	$\omega_{\mathrm{r,meas}}/2\pi$ (GHz)	$\delta\omega_{\mathrm{r}}$ (MHz)
IM2-4	FTR1	6.991	6.547	444
	FTR2	7.604	-	-
	FTR3	8.264	7.908	356
	FTR4	6.999	6.581	418
IM2-3	FTR1	6.991	6.545	446
	FTR2	7.604	7.206	398
	FTR3	8.264	7.915	349
	FTR4	6.999	6.528	471
IM5-2	FTR1	7.046	6.750	296
	FTR2	7.333	7.060	273
	FTR3	7.940	7.600	340
	FTR4	6.762	6.405	357

Table 4.7: Influence of the SQUID inductance on the resonance frequencies of all FTRs. $\omega_{\mathrm{r,design}}^{0}$ is the designed frequency without the SQUID inductance. $\omega_{\mathrm{r,meas}}$ is the measured resonance frequency including the SQUID inductance. The frequency shift $\delta\omega_{\mathrm{r}}$ allows calibration of the SQUID inductance as shown in Eq. (4.7)

Due to the influence of the SQUID inductance all resonance frequencies of FTRs have shifted to lower frequencies compared to the bare MW resonator ($\omega_{\mathrm{r}} < \omega_{\mathrm{r}}^{0}$). The SQUID inductance consists of the Josephson inductance L_{JJ} as well as the loop inductance $L_{\mathrm{loop}} = L_{\mathrm{loop}}^{\mathrm{geom}} + L_{\mathrm{loop}}^{\mathrm{kin}}$. We determine the total SQUID inductance experimentally for all SQUIDs with Eq. (4.7) and compare the results in Tab. 4.8 to the expected values according to the design.
Interestingly the total SQUID inductance is much smaller than expected from the theory. We analyse the results in the following:

- The SQUID inductance yields a clear dependence on the geometric loop inductance. For Sq3 the measured values of $L_{\mathrm{sq,meas}}$ match perfectly to the designed $L_{\mathrm{loop,design}}^{\mathrm{geom}}$. With increasing loop size in Sq2, Sq1 and Sq4 also the measured value of $L_{\mathrm{sq,meas}}$ increases.
- For some reason, the kinetic loop inductance and the Josephson inductance are not

observable in this measurement. In particular, the Josephson junctions on sample IM2-3 are by a factor of 4 bigger than on sample IM5-2, which should result in a reduction of the critical current and hence an increase in the Josephson inductance by the same factor. The measured inductances on both samples however, do not show a difference.

sample	SQUID	$L_{\mathrm{sq,meas}}$ (pH)	$L^{\mathrm{geom}}_{\mathrm{loop,design}}$ (pH)	$L^{\mathrm{kin}}_{\mathrm{loop,design}}$ (pH)	$L_{\mathrm{JJ,design}}$ (pH)
IM2-4	Sq1	45	63	241	40
	Sq2	-	41	124	40
	Sq3	26	24	52	40
	Sq4	42	92	355	40
IM2-3	Sq1	45	63	241	40
	Sq2	34	41	124	40
	Sq3	25	24	52	40
	Sq4	48	92	355	40
IM5-2	Sq1	28	63	241	160
	Sq2	23	41	124	160
	Sq3	26	24	52	160
	Sq4	39	92	355	160

Table 4.8: The total SQUID inductance of all measured SQUIDs is determined experimentally according to Eq. (4.7) and compared to the design values of the loop inductance and the Josephson inductance. Interestingly the SQUID inductance is much smaller than expected from the theory and yields a clear dependence on the geometric loop inductance. The kinetic loop inductance and the Josephson inductance are not observable in this measurement. $L^{\mathrm{geom}}_{\mathrm{loop,design}}$, $L^{\mathrm{kin}}_{\mathrm{loop,design}}$ and $L_{\mathrm{JJ,design}}$ are calculated according to Eqs. (2.33), (2.32) and (2.29) respectively.

At this point the reader might conclude that the Josephson inductance is not observable because the junctions are broken, but things become complicated as Sq1 in FTR1 on sample IM2-3 and Sq3 in FTR3 on sample IM5-2 are indeed functional. When applying magnetic field the resonance frequencies of these FTRs tune and hence there must be a finite Josephson inductance included in the measured total SQUID inductance.

We sum up that the measured total SQUID inductance is smaller than expected and the comparison to the theory suggest that $L_{\mathrm{sq,meas}}$ depends on the geometry of the SQUID loop. As $L_{\mathrm{sq}} = L_{\mathrm{loop}} + L_{\mathrm{JJ}}$, the Josephson inductance of the functional SQUIDs therefore must be very small. According to Eq. (2.29) a small Josephson inductance implies large critical currents which is contradictive to the dc-precharacterizations shown in Sec. 4.2.
We have to consider two possibilities:

- On the one hand, it could be possible that the assumed equivalent circuit diagram shown in Fig. 2.7 is not sufficient to describe our system consisting of geometric-, kinetic- and Josephson inductances. Possibly one has to find more complex equations to describe the system properly.

- On the other hand, the measured frequency shift $\delta\omega_{\mathrm{r}}$ is in the order of a few 100 MHz for all FTRs and corresponds without doubt to a small SQUID inductance. We therefore also should consider the possibility that the Josephson inductances are small and the critical currents are high.

At this point we want to guide the readers attention to the design of the wires which form the SQUID loop. In the final device one arm of the SQUID loop acts as mechanical string-resonator and for symmetry reasons the other arm has the same dimensions. The race for strong electromechanical coupling has pushed the design to very thin and light strings in the order of 100 nm, 1 pg (compare Tab. 3.2). When two superconducting materials are connected by a thin wire with spatial dimensions below the coherence length ($\xi_{\mathrm{BCS}}^{\mathrm{Al}} = 170\,\mathrm{nm}$ in aluminium [83]), the thin wire acts as a weak link [84] and quantum effects similar to those observed in Josephson tunnel junctions appear [85]. In literature these thin and short wires are called nano-bridges and show much higher critical currents than tunnel junctions [86]. In Ref. [87] characteristic properties of nanobridges have also been observed in long Pb wires with lengths up to 20 µm ($\xi_{\mathrm{BCS}}^{\mathrm{Pb}} = 90.5\,\mathrm{nm}$ in lead [88]). In Ref. [87] it is also mentioned that only a small part of the samples (5%) have good pronounced Josephson effects.
Consequently we consider the possibility that the thin wires in the SQUID loop act as additional Josephson junctions and interfere with the tunnel junctions or even dominate the system. On sample IM5-2 only the SQUID with the thickest and shortest SQUID arms ($w_{\mathrm{string}} = 150\,\mathrm{nm}$, $l_{\mathrm{string}} = 15\,\mu\mathrm{m}$) was tunable.
For further projects we propose that width and thickness of the string-resonators should not approach a substantial fraction of the coherence length in the chosen material.
As the coupling strength is inverse proportional to the mass $g_0 \propto 1/m$ this restraint would reduce the achievable coupling strength.

Having discussed possible reasons for the non-tunability of FTRs, we now analyse the characteristics of those FTRs which are tunable.
In order to characterize the behaviour of a FTR we record the power transmission spectrum around the resonance frequency and sweep the magnetic field. The sample IM2-3 has been characterized in the "Triton" setup as shown in Sec. 3.3.3. Results for FTR1 are shown in Fig. 4.8.
We analyse Fig. 4.8 and note that in the depicted frequency range two resonators are visible: FTR1 and FTR4. FTR4 is not tunable and appears in the spectrum at a constant frequency of $\omega_{\mathrm{r}}^{\mathrm{FTR4}} = 6.528$. FTR1 tunes with externally applied magnetic field in a frequency range between 6.48 GHz and 6.545 GHz resulting in a relative modulation depth of $\Delta\omega/\omega_{\mathrm{r}} = 0.01$. At the lowest point of the tuning range the frequency jumps back up due to additional flux in the SQUID loop, induced by screening currents. In order to investigate electromechanical coupling we have to tune the resonator to a steep flux point in the lower part of the tuning range. At such a point our system was unstable, repeatedly flux jumps occurred.
Nevertheless we calculate the slope $d\omega_{\mathrm{r}}/d\Phi = 2\pi \cdot 0.75\,\mathrm{GHz}/\Phi_0$ at the steepest point which was reachable. The FTRs shown in previous work [40] are two orders of magnitude steeper. This shows that the strong hysteretic behaviour is a real show-stopper on the way to strong electromechanical coupling. For further samples we reduced the Josephson junction area as explained in Sec. 4.2. This should reduce the screening parameter β_{L} and prevent such flux

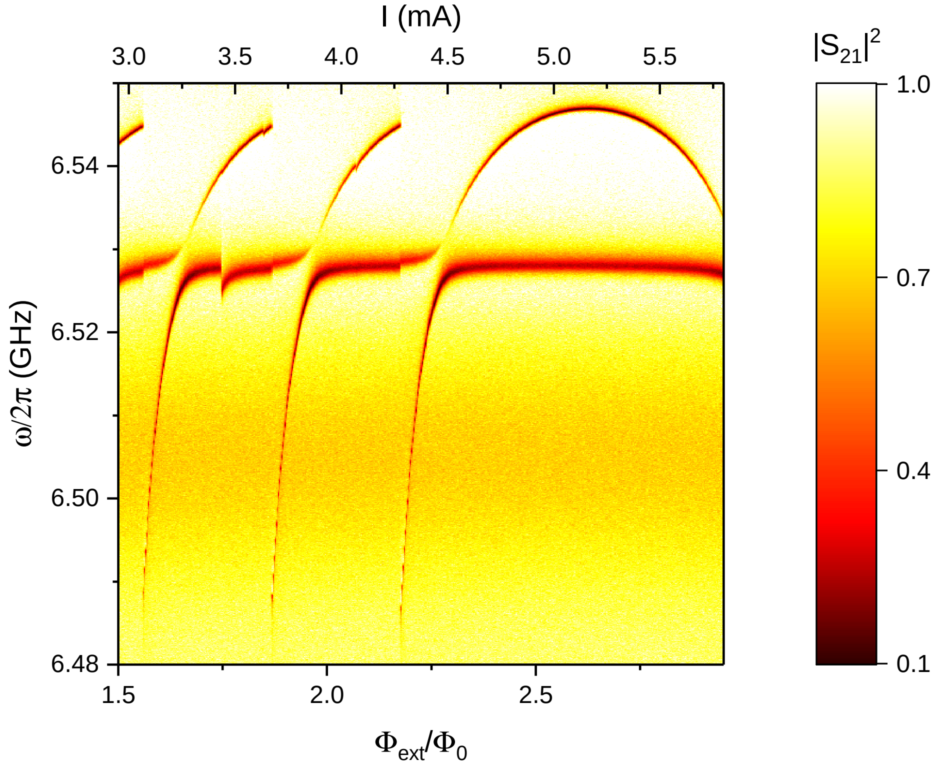

Figure 4.8: Magnetic field dependence of FTR1 on sample IM2-3. In the depicted frequency range two resonators are visible: FTR1 and FTR4. FTR4 is not tunable and appears in the spectrum at a constant frequency of $\omega_r^{FTR4} = 6.528$. FTR1 tunes with externally applied magnetic field in a small frequency range of $\Delta\omega = 65$ MHz. At 6.48 GHz, FTR1 jumps back to a higher frequency due to the influence of finite β_L. The two resonators FTR1 and FTR4 are weakly coupled via the transmission line. When FTR1 tunes through the resonance frequency of FTR4 we observe an anticrossing.

jumps.
We show a detailed analysis of the critical current and the SQUID inductance in Tab. 4.9.
As the superconducting coil which was used in order to create the magnetic field has not been calibrated in previous experiments, we have calibrated the proportionality between applied current and resulting magnetic field from the measurement data. Usually one records several periods of the tuning. The distance between two minima equals Φ_0 and allows the calibration of the magnetic field with the SQUID loop area known. As one can see in Fig. 4.8, the FTR presented here shows hysteretic behaviour and so the spacing between the minima is reduced to an unknown value. Therefore we have calibrated the coil by extrapolating the tuning of FTR1 according to Eq. (2.35) beyond the flux jumps. The resulting calibration constant for the coil in the Triton setup is $\gamma = 15\,\mu\mathrm{T/mA}$. This value should be verified in other experiments in the future.

The second tunable FTR which we have measured is situated on sample IM5-2. This sample has been measured in the "Kermit" setup. The superconducting coil used in this setup has been calibrated in Ref. [40] to be $\gamma = 44.19\,\mu\mathrm{T/mA}$. Nevertheless the magnetic field at the position of the SQUIDs can deviate in our setup from this value as we are using a different sample box. We show the magnetic field dependence of FTR3 on sample IM5-2 in Fig. 4.9 a) and b), where panel b) is a zoom into the region around the half integer flux quantum. In panels c) and d) we evaluate the total linewidth κ and the external coupling κ_{ext} as a function of the applied flux.

By reducing the Josephson junction size, here we were able to record nearly a full period without flux jumps. Outside of the depicted area flux jumps occurred, so again we were not able to record several periods for the calibration. We calibrate the coil at $\Phi_{\text{ext}} = \Phi_0/2$ by assuming that the amount of current applied to the coil to tune the resonator to its minimum equals the magnetic field $B = (\Phi_0/2)/A_{\text{loop}}$. The resulting calibration constant is $\gamma = 55\,\mu\text{T/mA}$.

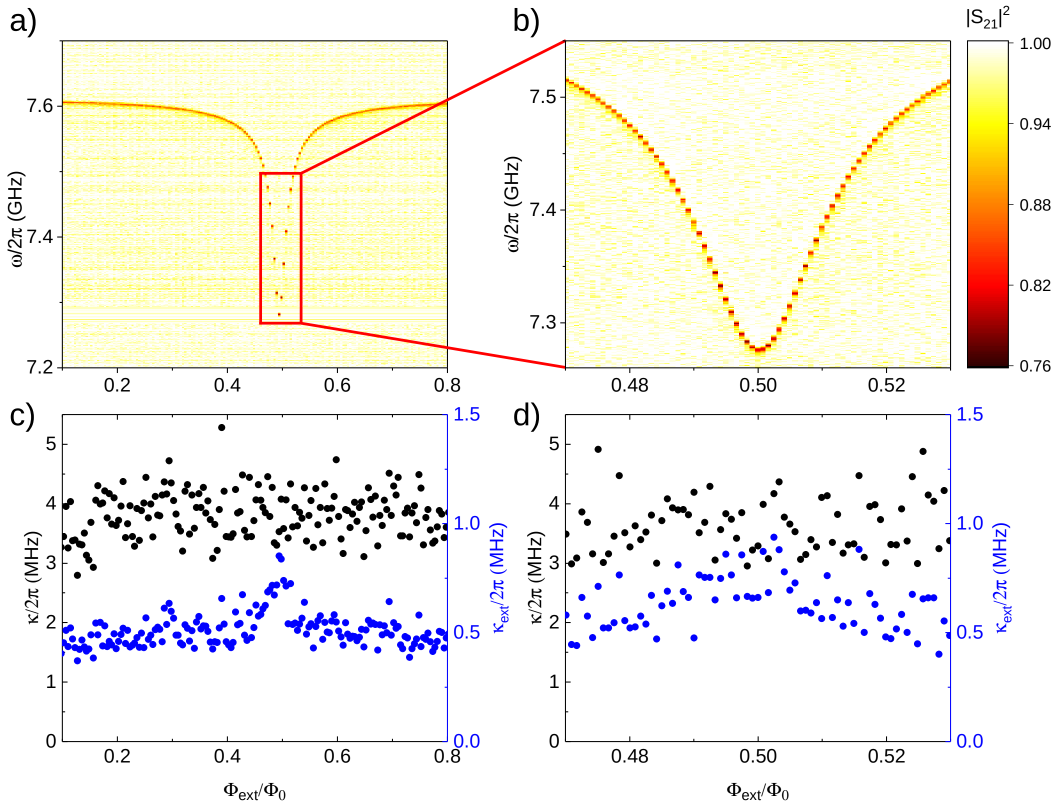

Figure 4.9: Magnetic field dependence of FTR3 on sample IM5-2. The resonator tunes with externally applied magnetic field in a frequency range of $\Delta\omega = 320\,\text{MHz}$. No flux jumps occurred in the presented region. In panel a) we depict an overview of the tuning for externally applied flux in the range between 0 and $0.8\,\Phi_{\text{ext}}/\Phi_0$. In panel b) we show a zoom into the region around the half integer flux quantum which is indicated with a red rectangle in panel a). In panels c) and d) we evaluate the total linewidth κ and the external coupling κ_{ext} as a function of the applied flux for the plots presented in a) and b) respectively.

When analysing Fig. 4.9 we see that the resonator is tunable in a frequency range between 7.28 GHz and 7.6 GHz. The close-up depicted in Fig. 4.9 b) proves that at the minimum, there

is a smooth transition and not a flux jump. The relative modulation depth $\Delta\omega/\omega_{\mathrm{r}} = 0.05$ is very small. In Sec. 2.3 we have derived that for totally symmetric Josephson junctions the relative modulation depth is 1 and with increasing asymmetry the modulation is suppressed. We have also seen in Eq. (2.39), that the influence of the asymmetry scales with the critical current. The SQUID which is embedded into FTR3 has been designed to be completely symmetric with critical currents of $I_{\mathrm{c}} = 1\,\mu\mathrm{A}$. Pictures taken with the SEM reveal that both Josephson junctions have indeed very similar junction areas and also the SQUID arms are symmetric. We measured the size of both junction areas and find $\alpha_{\mathrm{I}} < 0.1$. We use Eq. (2.39) to estimate the critical current of the SQUID. Therefore we solve Eq. (2.39) for I_{c} and insert, the measured relative modulation depth $\Delta\omega/\omega_{\mathrm{r}} = 0.05$, the estimated asymmetry parameter $\alpha_{\mathrm{I}} < 0.1$, the resonator inductance $L_{\mathrm{r}} = 0.72\,\mathrm{nH}$ from Tab. 4.9 and the geometric loop inductance $L_{\mathrm{loop}} = 24\,\mathrm{pH}$ from Tab. 4.8, and get: $I_{\mathrm{c}} > 37.4\,\mu\mathrm{A}$.
We further notice that the shape of the tuning is flat over a broad range of the applied flux. Around the half integer flux quantum the resonator tunes down steeply. In Fig. 2.8 we have plotted the expected shape of the tuning for different values of I_{c}. A comparison of the experimental results shown above with the expectation also strongly suggests that the critical current in FTR3 is high.
We will fit the shape of the FTR with Eq. (2.35) in Fig. 4.10 and indeed we will find, that the asymmetry is $\alpha_{\mathrm{I}} = 0.03$ and the critical current is $I_{\mathrm{c}} = 153\,\mu\mathrm{A}$.

To sum up, both, the estimation from the modulation depth and the fit of the tuning shape agree for FTR3 on sample IM5-2 on a small asymmetry and a high critical current. On this sample, the presented SQUID in FTR3 is the only one which is functional. Therefore we can not confirm this result with a second measurement. Contacting this SQUID in dc-configuration as shown in Sec. 4.2 was also not possible due to the small width of coplanar waveguides. For typical Josephson tunnel junctions the value of I_{c} is very high. Furthermore it matches the design parameter of $I_{\mathrm{c}} = 1\,\mu\mathrm{A}$ not at all. This result speaks strongly for the assumption that the thin SQUID arms act as a weak link and provide the Josephson inductance instead of the tunnel junction.

At this point one has to ask the question whether or not the model we have introduced in Sec. 2.3 describes the flux tunable resonators properly. We clarify this question by applying our model to data which has been published in Ref. [40] and compare the results.
The data from the reference contains two FTRs which have been designed for a critical current of $I_{\mathrm{c}} = 0.5\,\mu\mathrm{A}$. The SQUID arms have a width of 250 nm and thickness of 110 nm. We present an overview of the data together with the FTRs which we have measured in this thesis in Fig. 4.10. Black lines are the corresponding fits according to Eq. (2.35) for each FTR.
The agreement between fit and data is excellent for all FTRs. We present the corresponding fitparameters in Tab. 4.9. The critical currents obtained by the fit for Res1 and Res2 are in good agreement with the values given in Ref. [40]. We conclude that Eq. (2.35) is valid and the critical currents in our FTRs are indeed very high.

The figure of merit for further experiments however is the slope $d\omega_{\mathrm{r}}/d\Phi$ at the steepest point of

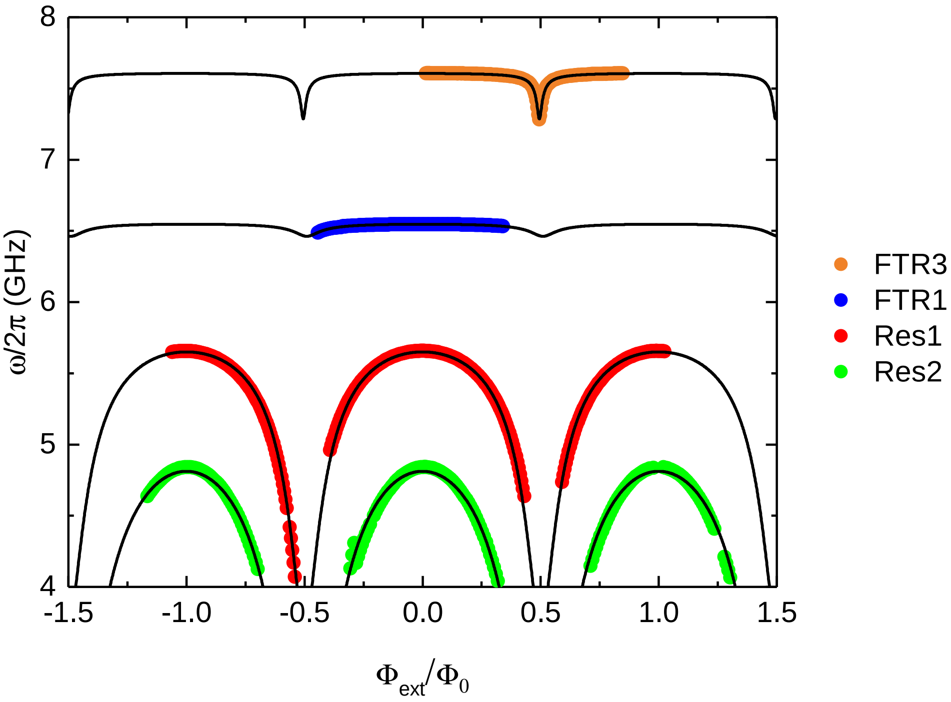

Figure 4.10: Comparison of FTRs from Ref [40] with the FTRs characterized in this thesis. All FTRs are fitted with Eq. (2.35). The agreement between fit and data is excellent for all FTRs. Although the design and the fabrication the Josephson tunnel junctions fabricated in this thesis and the ones published in [40] is very similar, the shape of the tuning curves differs strongly. The values of I_c for FTR1 and FTR3 are two orders of magnitude larger than the ones of Res1 and Res2.

	$\omega_r^0/2\pi$ (GHz)	I_c (μA)	L_r (nH)	L_{loop} (pH)	α_I	$d(\omega_r/2\pi)/d\Phi$ (GHz/Φ_0)
FTR1	6.94	88.7	0.7	40	0.15	0.75
FTR3	7.88	153.3	0.72	25	0.03	14.4
Res1	6.20	0.62	2.70	4	0.14	14.3
Res2	7.40	0.42	0.99	21	0.36	5.8

Table 4.9: Overview of the fit parameters for the FTRs shown in Fig. 4.10. ω_r^0 is a design parameter and was therefore fixed at the given value. The critical currents obtained for Res1 and Res2 are in good agreement with the values given in Ref. [40]. The slopes have been evaluated at the steepest point of each FTR in the depicted frequency range.

the accessible tuning range. We have determined the slopes by calculating the derivatives of the fits for all FTRs and present the results in Tab. 4.9. We note that Res1 and Res2 have been evaluated at $\omega_r/2\pi = 4\,$GHz. In Ref. [40] it is mentioned that Res1 and Res2 can be tuned to lower frequencies than depicted in the overview scan, however the continuous measurement data of Ref. [40] ends at 4 GHz. In Ref. [40] a slope of $60\,\mathrm{GHz}/\Phi_0$ at 3.3 GHz has been found by recording the slope in a small frequency range and a small flux range. In such a zoom the slope can be easily extracted with a linear fit. The reported slope of $60\,\mathrm{GHz}/\Phi_0$ is a real experimental

value, however, we can not include the data into the overview in Fig. 4.10 as the datasets are independent and can not be matched with respect to the magnetic flux.
We can extrapolate the fit in Fig. 4.10 to lower frequencies, but as the minimum of the tuning has not been determined in Ref. [40], the values of α_I and thus the slope at lower frequencies differ significantly for different start values in the fitting routine. The reported slope of $60\,\mathrm{GHz}/\Phi_0$ at $3.3\,\mathrm{GHz}$ was only reproducible by assuming that $\alpha_\mathrm{I} = 0$. In that case the agreement between fit and data was worse. Therefore we have evaluated the slope at $4\,\mathrm{GHz}$.

Although the relative frequency modulation of FTR3 is small, the slope is comparable to the one of Res1. The steepest point is at a flux value of $0.494\,\Phi_0$ with a slope of $d\omega_\mathrm{r}/d\Phi = 2\pi \cdot 14.4\,\mathrm{GHz}/\Phi_0$. We plug this value into Eq. (2.52) and determine the coupling strength which can be achieved with this FTR:

$$\frac{g_0}{2\pi} = 14.4\,\mathrm{GHz}/\Phi_0 \cdot 1\,\mathrm{mT} \cdot \beta \cdot 15\,\mathrm{\mu m} \cdot 43\,\mathrm{fm} = 2.9\,\mathrm{kHz} \tag{4.8}$$

This value is smaller than the maximum coupling strength we estimated in Chap. 2. This is due to the fact that the slope of the FTR is not as steep as expected and the string is a factor of 4 shorter. The FTRs with longer string-resonators did not show any frequency tuning.
In Sec. 2.7 we have seen that the hybrid system with a string length of $l = 60\,\mathrm{\mu m}$ results in an effective flux change of $\delta\Phi = 38\,\mathrm{\mu}\Phi_0$ when excited thermally at 100 mK. The short string-resonator beeing present here, creates less flux modulation and is additionally excited by less phonons ($\bar{n}_\mathrm{m} \propto 1/\Omega_\mathrm{m}$), resulting in an effective flux change of $\delta\Phi = 3.6\,\mathrm{\mu}\Phi_0$. Furthermore we have seen in Sec. 2.7 that the total flux change is distributed over the linewidth of the mechanical resonator. With the low quality factor of FTR3 reported in Tab. 4.1, the linewidth is broader than the typically assumed $\Gamma_\mathrm{m} = 10\,\mathrm{Hz}$ at mK temperatures and followingly the necessary flux resolution in units of $\Phi_0/\mathrm{Hz}^{1/2}$ is very challenging.

To get insight into the flux sensitivity of our SQUID, we analyse how the linewidth of FTR3 depends on the flux-to-frequency transfer function.
In Fig. 4.9 c) and d), we show the magnetic flux dependence of κ and κ_ext for c) the whole flux range and d) a zoom around the half integer flux quantum. While for κ no significant flux dependence can be observed, for κ_ext we observe an increase of $\Delta\kappa_\mathrm{ext}/2\pi \approx 300\,\mathrm{kHz}$ in the region where the flux-to-frequency transfer function is maximal.
With this transfer function H we translate the frequency fluctuation $\delta\omega$ into a flux fluctuation $\delta\Phi$ and find:

$$\delta\Phi = \frac{\delta\omega_\mathrm{r}}{H} = \frac{300\,\mathrm{kHz}}{14.4\,\mathrm{GHz}} \cdot \Phi_0 = 20.8\,\mathrm{\mu}\Phi_0 \tag{4.9}$$

The flux fluctuations which induced the observed linewidth broadening can be considered as noise background. With the noise being a factor of 3 bigger than the expected signal, a detection is very challenging. To state whether or not we will be able to detect the flux modulation of $\delta\Phi = 3.6\,\mathrm{\mu}\Phi_0$ we would need more information about the spectral composition of the background noise.
The fact that κ_ext showed an increase in linewidth and κ did not, suggests that the intrinsic linewidth of the MW resonator is a limitation to the flux sensitivity. In the case of a broad resonance spectrum (as given here), small fluctuations are not visible. This result again emphasises

the need of high-Q MW resonators.
We summarize the results which we have gained in this section:

- The analysis of the resonance frequencies of FTRs on three different samples has revealed that the Josephson tunnel junctions are not responsible for the frequency shift ($\omega_\mathrm{r} < \omega_\mathrm{r}^0$). Instead the frequency shift appears most likely due to the geometric inductance of the SQUID loop. The Josephson inductance in functional flux tunable resonators is consequently very small, resulting in high critical currents.
- The relative frequency modulation $\Delta\omega/\omega_\mathrm{r} = 0.05$ of FTR3 on sample IM5-2 suggests that $I_\mathrm{c} > 37.4\,\mu\mathrm{A}$, which agrees with the results obtained by fitting the shape of the tuning.
- Comparison of our FTRs with the ones published in Ref. [40] has shown that Eq. 2.35 is valid and that I_c is indeed two orders of magnitudes higher in our samples. A reduction of the Josephson junction size has not reduced the observable critical current in the FTRs. The observed I_c is much bigger than typically achieved with Josephson tunnel junctions. We conlcude that the SQUID is dominated by an additional Josephson inductance introduced by the thin SQUID arms, acting as a weak link.
  In an equivalent circuit diagram the tunnel junction and the weak link junction would be connected in each SQUID arm in series configuration. Therefore the expected total inductance would be the sum $L_\mathrm{total} = L_\mathrm{tunnel} + L_\mathrm{link}$ or in other words, one would always expect to observe the junction with the lowest I_c.
  Contradictive to this consideration, the measurements of the SQUID inductance have not shown the existance of a Josephson tunnel inductance. As the functionality of a SQUID is based on quantum interference, one could assume that the additional Josephson junction interferes with the others and creates a more complex dependency, which needs to be solved theoretically in order to understand it properly.
  Regarding the weak link, we mention, that the described effects typically appear when the dimensions of the superconductor are strongly confined to a few nm. Our strings with the smallest dimension being 80 nm are still rather large. However we assume that at some point along the string-resonator there might be some defect or impurity which can act as a spatial or electrical bottleneck.
- Contrary to the observations of high I_c in the MW regime, in a dc-configuration the observed critical currents are in the order of a few µA and correspond to the expectation of a normal Josephson tunnel junction.
- The maximum slope of FTR3 is $d\omega_\mathrm{r}/d\Phi = 2\pi \cdot 14.4\,\mathrm{GHz}/\Phi_0$ and the corresponding coupling strength is $g_0/2\pi = 2.9\,\mathrm{kHz}$. The effective flux modulation induced by the motion of the 15 µm long string resonator in a thermally excited state is in the order of $\delta\Phi = 3.6\,\mu\Phi_0$.

Tunable non-linearity

Another interesting characteristic of a FTR is its non-linearity. In analogy to the non-linearity of mechanical string-resonators discussed in Sec. 4.1, also a MW resonator shows duffing behaviour

when excited at high amplitudes, as then higher order terms become relevant. In FTRs this behaviour is enhanced by the additional non-linear inductance of the SQUIDs. Thus, by analysing the duffing behaviour, one can draw conclusions about the SQUID parameters.
In Ref. [89] the equation of motion of a duffing FTR has been derived from the Lagrangian of the MW resonator + SQUID system. In analogy to mechanical resonators we refer to the parameter in front of the cubic contribution as duffing parameter [89]:

$$\beta_\mathrm{d} = \frac{4\pi^2}{3\hbar}\frac{C'}{L'}U\,, \tag{4.10}$$

with $C' = C_\mathrm{r} + C_\mathrm{JJ}$, $1/L' = 1/L_\mathrm{r} + 1/L_\mathrm{JJ}$ and U the Kerr-non-linearity.
In Ref. [89] it has been shown that a small non-linearity corresponds to high critical currents, as $L_\mathrm{JJ} \propto 1/I_\mathrm{c}$.
From the equation of motion one can derive the transcendental equation of the duffing oscillator [89]. By solving this equation one finds a relation between the maximum amplitude and the frequency shift $(\omega_\mathrm{eff} - \omega_\mathrm{r})$:

$$A^2_\mathrm{max} = \frac{4C'}{3\beta_\mathrm{d}}\left(\omega_\mathrm{eff} - \omega_\mathrm{r}\right)\,, \tag{4.11}$$

with A_max the maximum amplitude at the cut-off frequency. We note that in an LC-circuit the physical quantity which is related to the amplitude is the electrical charge or the amount of current. The resonators are characterized in transmission measurements. When the resonance condition is met, the resonator absorbs power from the transmission-line and emits power due to internal and external losses. In a steady state this results in a finite number of electrical excitations in the resonator given by Eq. (2.13). For the following we consider the absorbed power $P_\mathrm{abs} = (1 - |S_{21}|^2) \cdot P_\mathrm{drive}$ as the uncalibrated squared amplitude ($P_\mathrm{abs} \propto I^2$).

In order to quantify the duffing behaviour of FTR3 on sample IM5-2 we have performed power sweeps with drive powers at the sample input ranging from $-100\,\mathrm{dBm}$ to $-70\,\mathrm{dBm}$ at the sweet spot and at three working points with increasing resonator slope. At the sweet spot, no duffing behaviour was observable in the given power range. At an applied flux of $\Phi_\mathrm{ext}/\Phi_0 = 0.34$ we observed the onset of the duffing behaviour at the critical drive power of $P_\mathrm{c} = -75\,\mathrm{dBm}$. With increasing applied flux, the onset of the duffing shifted to lower drive power as shown in Tab. 4.10.
In Fig 4.11 a) and b) we show the duffing curves at the working points $\omega_\mathrm{r}/2\pi = 7.548\,\mathrm{GHz}$ and $\omega_\mathrm{r}/2\pi = 7.290\,\mathrm{GHz}$ for several drive powers.

By plotting the uncalibrated squared amplitude over the frequency shift we can extract the uncalibrated duffing parameter according to Eq. (4.11) for each working point. The data including linear fits is shown in Fig. 4.11 c) and d).
At the working points of 7.592 GHz and 7.548 GHz β_d is negative, which corresponds to a shift of ω_r towards lower frequencies and a softening of the spring constant in the mechanical analogue. At the working point of 7.29 GHz however, the duffing behaviour is reversed. We observe a shift of ω_r towards higher frequencies which corresponds to a hardening of the spring constant and a positive duffing parameter β_d. We plot the behaviour of $1/\beta_\mathrm{d}$ over the applied flux in

$\frac{\omega_r}{2\pi}$ (GHz)	$\frac{\Phi_{ext}}{\Phi_0}$	$\frac{d\omega_r}{d\Phi}$ $\left(\frac{\mathrm{GHz}}{\Phi_0}\right)$	$\frac{d^2\omega_r}{d\Phi^2}$ $\left(\frac{\mathrm{GHz}^2}{\Phi_0^2}\right)$	P_c (dBm)	$\frac{1}{\beta_d}$
7.600	0	0	0	>-70	–
7.592	0.340	-0.1	-1.4	-75	$-1.6 \cdot 10^{-24}$
7.548	0.450	-1.3	-43	-85	$-3.7 \cdot 10^{-25}$
7.290	0.497	-9.8	+2264	-97	$+3.8 \cdot 10^{-26}$

Table 4.10: Analysis of the non-linearity at different working points in the whole tuning range of FTR3. At the sweetspot no non-linearities have been observed. Application of higher drive powers was not possible due to heating effects in the cryostat. At the other working points the onset of the non-linear duffing effect has been observed at the critical drive power P_c. With increasing applied flux the non-linearity increases and the critical drive power decreases. At the last working point the second derivative and the non-linearity change sign.

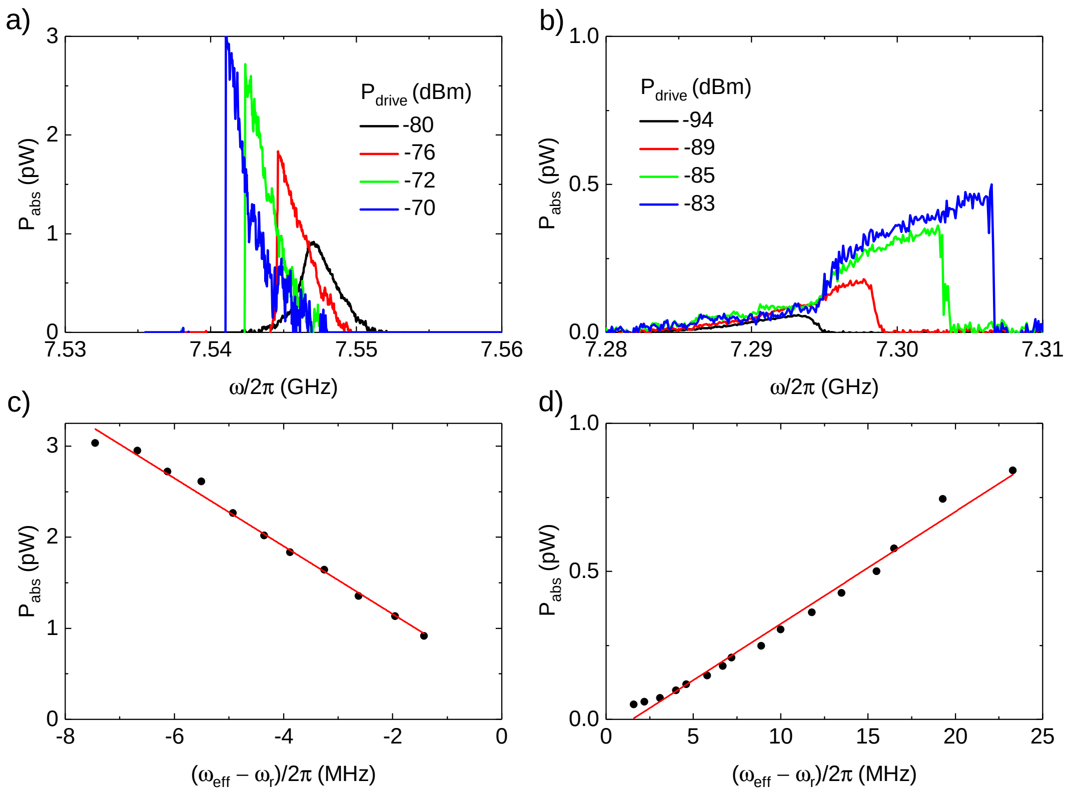

Figure 4.11: non-linear frequency response of FTR3 for several drive powers at two different working points a) $\omega_r/2\pi = 7.548$ GHz and b) $\omega_r/2\pi = 7.290$ GHz. Interestingly the change of $1/\beta_d$ from negative to positive values results in a flip of the duffing behaviour. In panel c) and d) the uncalibrated squared amplitude is plotted over the frequency shift for the measurements depicted in a) and b) respectively.

Fig. 4.12 d). For comparison we show the shape of the tuning curve $\omega_r(\Phi)$ as well as the first derivative $d\omega_r/d\Phi$ and the second derivative $d^2\omega_r/d\Phi^2$ in Fig. 4.12 c), b) and a) respectively. We observe that for a flux bias of $\Phi_{ext}/\Phi_0 = 0.5$ the value of $1/\beta_d$ approaches zero and a transition into the positive regime occurs. Simultaneously the second derivative changes sign from negative

values to positive values. In order to provide a reliable interpretation of the behaviour, more measurement data would be necessary. Nevertheless we try to understand the physical concepts. From a physical point of view we compare the duffing behaviour of mechanical and electrical resonators. In the case of the mechanical resonator the amplitude corresponds directly to the displacement of the string and it is evident that strong excitations modify the effective length of the string and hence increase both, the stress and the restoring force. This results in a hardening of the spring constant and hence an increase in frequency.
In the case of the electrical LC-resonator, we have stated above that the amplitude corresponds to the amount of charge or current. For high amplitudes, the capacitors are occupied with many charges. As the spatial dimensions of our resonators are small, effects of charge accumulations decrease the restoring force which results in a decrease of the spring constant and hence a decrease in frequency. The direction of the frequency shift is therefore determined by the fundamental physics. The experimental observation of a duffing reversal seems contradictive, however we can understand the behaviour by taking into account the non-linear Josephson inductance. By embedding a SQUID into the MW resonator we have bound the resonance frequency to the magnetic flux in the SQUID loop. Now clearly, a change of frequency due to the duffing effect results in a change of flux in the SQUID loop. The flux tunable resonator therefore has to perform work against the flux quantization. The higher the slope of the tuning shape, the less flux $d\Phi$ must be generated to perform a frequency shift $d\omega$: $d\omega = H d\Phi$, with H the frequency-to-flux transfer function. This explains that for zero applied flux where $H = 0$ the duffing behaviour is suppressed and with increasing slope the duffing behaviour increases. It seems physically reasonable that the duffing behaviour flips into the direction where the transfer function increases. We have indicated the direction of the duffing in Fig. 4.12 with red arrows. Additionally we mention that the working point which showed a positive duffing parameter is very close to the minimum of the tuning range. We remind the reader that the non-linearity of the Josephson inductance is due to the $1/\sqrt{\cos^2(x) + \alpha_\mathrm{I}^2 \sin^2(x)}$ term. Thus close to the half integer flux quantum the $\sin(x)$ term dominates the non-linearity instead of the $\cos(x)$ term, which corresponds to a change in parity and could also be a reason for change in duffing.

We summarize the results from the duffing analysis.
Although we applied strong drive powers of $-70\,\mathrm{dBm}$, FTR3 showed no non-linear effects over a broad range of flux bias from the sweet spot to $\Phi_\mathrm{ext}/\Phi_0 = 0.34$.
At this flux bias, the contribution of the non-linear term in the Josephson inductance should already be significant. As the inductance scales with $1/I_\mathrm{c}$ we conclude that a high critical current suppresses the non-linearity. This argument also holds for the shape of the frequency-flux dependence shown in Fig. 4.9.
The observed onset of duffing behaviour in FTR3 at the flux bias of $\Phi_\mathrm{ext}/\Phi_0 = 0.34$ occurs at a critical drive power of $P_\mathrm{c} = -75\,\mathrm{dBm}$, which corresponds to an average photon number of $\bar{n}_\mathrm{r} \approx 125\,000$.
We have observed that the non-linearity is in-situ tunable. At flux bias close to $\Phi_\mathrm{ext}/\Phi_0 = 0.5$ the critical photon number is reduced to $\bar{n}_\mathrm{r} \approx 820$.

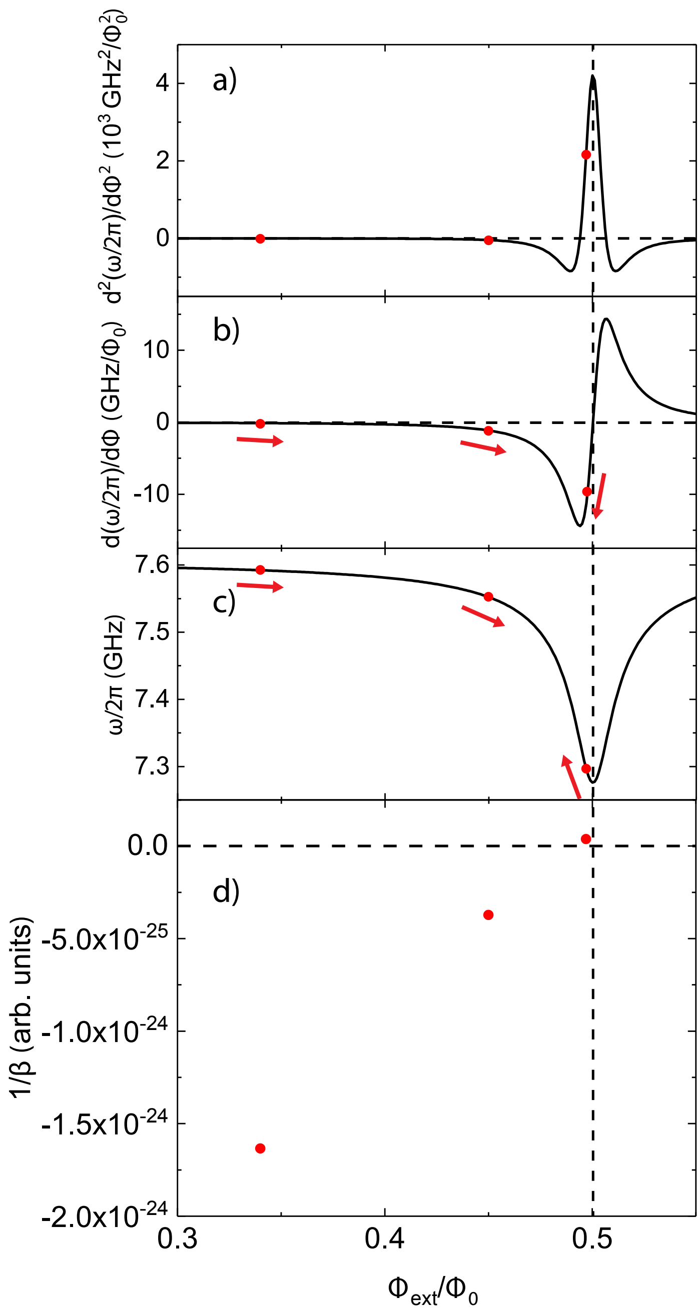

Figure 4.12: Duffing behaviour of FTR3 over a broad range of applied magnetic flux. In panels c), b) and a) we show the the shape of the resonator tuning $\omega_\mathrm{r}(\Phi_\mathrm{ext})$, the first derivative $d\omega_\mathrm{r}/d\Phi$ and the second derivative $d^2\omega_\mathrm{r}/d\Phi^2$ respectively. In panel d) we show the inverse duffing parameter $1/\beta_\mathrm{d}$. For $\Phi_\mathrm{ext}/\Phi_0 = 0.5$ the value of $1/\beta_\mathrm{d}$ approaches zero. In the measurement the values of $1/\beta_\mathrm{d}$ and $d^2\omega_\mathrm{r}/d\Phi^2$ change from the negative into the positive regime which results in a reversal of the duffing behaviour.

4.4 Two Tone Spectroscopy

Although the flux modulation induced by the mechanical string-resonator in FTR3 on sample IM5-2 is probably below the resolution limit, we have applied the technique of two tone spectroscopy introduced in Sec. 2.4.2.
Therefore we have tuned FTR3 to the steepest working point at $\omega_\mathrm{r}/2\pi = 7.35\,\mathrm{GHz}$. The setup includes a VNA and a MW source as depicted in Fig. 3.10 b). From the MW source we apply a strong drive tone with a given detuning $\Delta = \omega_\mathrm{d} - \omega_\mathrm{r}$ from the cavity resonance. With the VNA we probe the transmission through the sample. If electromechanical interaction is present we expect, referring to the theory on two tone spectroscopy introduced in Sec. 2.4.2, a peak or dip feature in the resonance spectrum of the resonator at a detuning of $\Delta = \pm\Omega_\mathrm{m}$. As the corresponding effects of EMIT and EMIA are based on interference effects, it depends on the strength of the drive and the probe power whether one observes a peak or a dip.
When we sweep the drive tone, the feature in the resonator should move as well, preserving the distance of Ω_m between drive tone and feature.

During the measurements we have increased the strength of the drive tone at the sample input to $P_\mathrm{drive} = -78\,\mathrm{dBm}$. The probe tone was at a constant value of $P_\mathrm{probe} = -93\,\mathrm{dBm}$. The number of photons in the resonator is the sum of n_drive and n_probe and depends on the detuning of the drive tone. Interestingly, even for small detunings, we did not observe duffing behaviour. This strongly supports the conclusions drawn in Sec. 4.3. The working point at $\omega_\mathrm{r} = 7.35\,\mathrm{GHz}$, where the measurements, presented here, are taken, is the steepest point in the tuning range. The first derivative takes an extremum and the second derivative is zero. This could be exactly the point where the duffing behaviour flips and eventually vanishes.
When reducing the detuning to very small values, the resonance spectrum of the FTR suddenly vanished completely. We concluded that the phonon number reached a critical value. It could eventually be possible that the current in the resonator exceeded the critical current and the SQUID switched into the voltage state. In the following we focus on the detuning range around $\Delta \approx \pm\Omega_\mathrm{m}$ and present measurement results.

We started our measurements in the red-sideband regime with $\Delta = -\Omega_\mathrm{m}$. In this regime the electromechanical interaction effectively cools the mechanical motion. This reduces the amplitude of the string-resonator, hence the flux modulation, what makes the detection difficult. We were not able to observe any interaction on the red-sideband.

On the blue-sideband however, the mechanical motion is amplified by the interaction mechanism and the flux modulation is increased. In Sec. 4.1 we estimated the mechanical frequency of the string in FTR3 at mK temperatures to be $\Omega_\mathrm{m}^\mathrm{mK}/2\pi = 15.8\,\mathrm{MHz}$. Indeed we have observed features that could origin from electromechanical interaction at detunings of $\Delta = 12.85\,\mathrm{MHz}$ and $\Delta = 14\,\mathrm{MHz}$.
At a detuning of $\Delta = 12.85\,\mathrm{MHz}$ two additional peaks appeared in the resonance spectrum. The results are depicted in comparison to the expectation from theory in Fig. 4.13.
The observed peaks did not occur reproducibly at a constant frequency instead they appeared

randomly inside the resonance spectrum. When moving the drive tone, the peaks did not show a clear dependence on the detuning. When reducing the detuning to values $\Delta < \Omega_{\mathrm{m}}$, where no electromechanical interaction should be present, more of these features appeared in the spectrum.

The theory plot corresponds to Eq. (2.47) with the actual parameters of FTR3: $\kappa/2\pi = 4\,\mathrm{MHz}$, $\kappa_{\mathrm{ext}}/2\pi = 0.5\,\mathrm{MHz}$, $\omega_{\mathrm{r}}/2\pi = 7.3533\,\mathrm{MHz}$, $g_0/2\pi = 2.9\,\mathrm{kHz}$. We assume $\Gamma_{\mathrm{m}}^{\mathrm{mK}}/2\pi = 200\,\mathrm{Hz}$ and $\Delta = \Omega_{\mathrm{m}}^{\mathrm{mK}} + 360\,\mathrm{kHz}$ which results in a small displacement of the peak from the centre of the resonance dip.

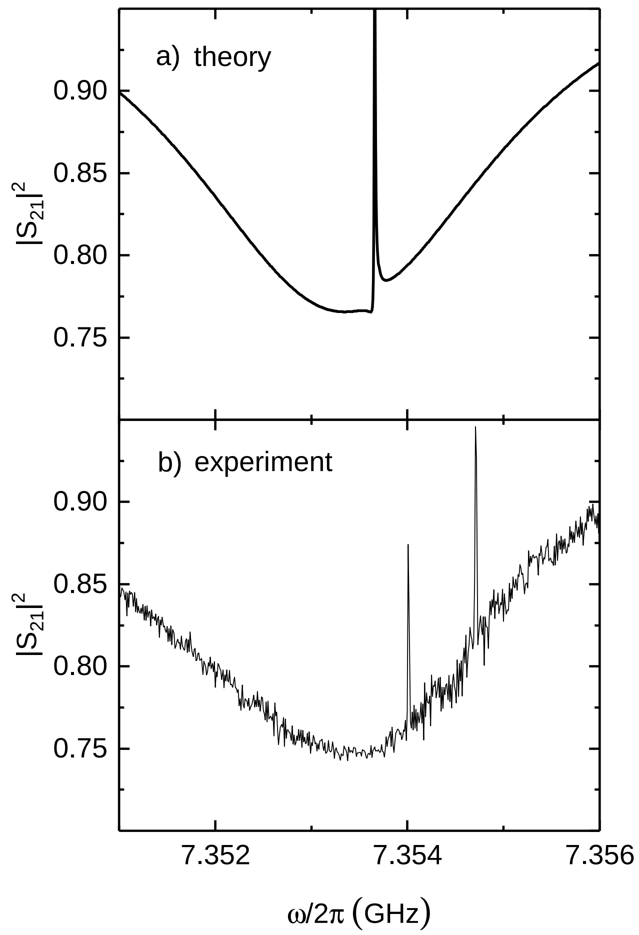

Figure 4.13: Comparison between theory in panel a) and experiment in panel b) of the power transmission spectrum of FTR3 in the presence of a strong drive tone at a detuning of $\Delta = 12.85\,\mathrm{MHz}$. The experimentally observed peaks were not reproducible at the shown positions and did not shift through the resonance dip when the drive tone was swept.

Comparing the experiment to the theory, we see, that the theoretically predicted shape of the peak resembles the observed experimental result. In the experiment we observe two peaks which can be attributed to the fact that the in-plane and the out-of-plane mode of the mechanical string-resonator vibrate at slightly different frequencies. Due to the fact that the peaks did not appear reproducibly at a given position, defined by Δ, and that they did not move with Δ, we can not conclude that the observation corresponds to the electromechanical interaction.

Furthermore we show in Fig. 4.14 frequency sweeps of the drive tone around the perfect detuning. In panel a) the experimental result, in panel b) the prediction from theory is shown.
The power transmission spectrum has been recorded with 10 times higher frequency resolution than the measurement shown in Fig. 4.13, resulting in measurement times of 100s per drive frequency. Surprisingly in this measurement the resonance dip shows a strong increase in linewidth to $\kappa \approx 8\,\mathrm{MHz}$ compared to measurement above where $\kappa \approx 4\,\mathrm{MHz}$ has been observed. However, the shape of the resonance is still symmetric and duffing behaviour is not present.
In a small region between $\Delta = 13.75\,\mathrm{MHz}$ and $\Delta = 14.1\,\mathrm{MHz}$, the depth of the resonance dip increases and the linewidth decreases. This behaviour could correspond to the phenomenon of electromechanically induced absorption explained in Sec. 2.4.2. In Fig. 4.14 each cut along the vertical axis corresponds to a power spectrum as depicted in Fig. 4.13. When moving the drive tone, we expect that the dip feature moves through the resonance as shown in Fig. 4.14 b).
The theory plot corresponds to Eq. (2.47) where both, ω_{drive} and ω_{probe} were swept, resulting in the 2D-plot. The parameters correspond to the actual parameters of FTR3: $\kappa/2\pi = 4\,\mathrm{MHz}$, $\kappa_{\mathrm{ext}}/2\pi = 0.5\,\mathrm{MHz}$, $\omega_{\mathrm{r}}/2\pi = 7.3533\,\mathrm{MHz}$, $g_0/2\pi = 2.9\,\mathrm{kHz}$. We assume $\Gamma_{\mathrm{m}}^{\mathrm{mK}}/2\pi = 200\,\mathrm{Hz}$ and $\Omega_{\mathrm{m}}^{\mathrm{mK}} = 13.5\,\mathrm{MHz}$.
Comparing theory and experiment one sees, that the dip-feature which we observed, did not move through the resonance and is much broader than expected. The broadness of the observed feature would suggest a high coupling strength, however in that case we would expect a splitting of the resonator mode as shown in Fig. 2.12 b). Analogously to the measurement shown above, here as well we can not conclude that the observed feature is due to electromechanical interaction. Due to the fact that the feature did not move with the drive tone, and that we do not observe a splitting of the resonator mode, experiment and theory can not be matched. It is especially difficult to find appropriate parameters which could reproduce the experimental result.

We summarize that the observation of electromechanic interaction remains challenging. Although the data suggests that there is some interaction, the shown measurements are not reproducible and we are not able to quantify the interaction.

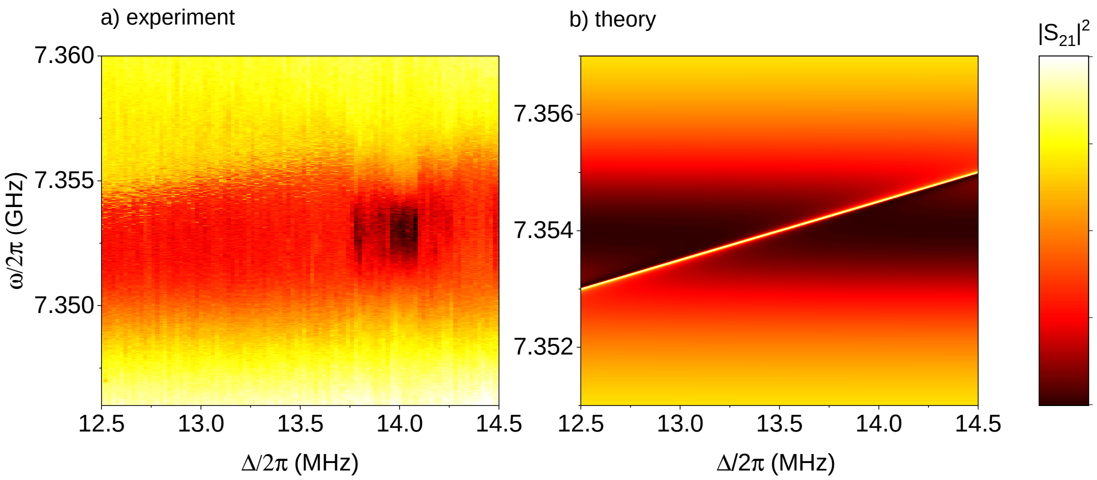

Figure 4.14: Comparison between theory and experiment of the power transmission spectrum of FTR3 in the presence of a strong drive tone. Experimental data is depicted in panel a), theory in panel b) The drive tone is swept in a range of 2 MHz around the perfect detuning $\Delta = \Omega_{\mathrm{m}}^{\mathrm{mK}}$. In a small region between $\Delta = 13.75\,\mathrm{MHz}$ and $\Delta = 14.1\,\mathrm{MHz}$ the depth of the resonance dip increases and the linewidth decreases. The shown behaviour was not reproducible.

Chapter 5

Summary and Outlook

In this thesis we have investigated the fundamental light-matter interaction between the mechanical motion of a string-resonator and a superconducting flux tunable MW resonator. The nature of the interaction mechanism is inductive. It is enabled in an electromechanical hybrid device consisting of a high quality MW resonator with an embedded dc-SQUID and an ultra high quality double clamped aluminium string-resonator, where the displacement of the string-resonator couples to the MW resonator by changing the area of the SQUID loop. We were able to fabricate a fully functional device. We characterized all components experimentally and determined the expected coupling strength according to the theory derived in Chapter 2. Further we applied the method of two tone spectroscopy which aims to quantify the electromechanical interaction. First experimental results suggest that electromechanical interaction could be present in our sample, however the results were not reproducible and a quantification of the coupling strength is still pending.

In the theoretical part of this thesis we gained, compared to previous work, deeper insight into the magnetic field dependence of FTRs and we were able to explain the experimentally observed behaviour with these new results. We calculated and compared the coupling strength for embedded string resonators and magnetic force microscopy cantilevers. We discussed the parameter space to optimize the coupling strength and fabricated hybrid devices accordingly. We analysed different types of noise sources being present in our setup, compared the magnetic flux sensitivity to state of the art devices reported in literature and finally proposed an experimental method to determine the noise floor in single-tone measurements using the frequency-noise calibration technique. Precise knowledge about the noise floor is especially important for further experiments to determine whether the restrictions in sensitivity are due to imprecision- or backaction noise.

In the experimental part we presented a procedure to fabricate the hybrid device based on an all-aluminium process. Compared to previous work, where niobium MW resonators have been used, the fabrication process has been simplified and we avoided lossy Al-Nb interfaces. Furthermore we showed successful release of the mechanical system using an isotropic etching process which avoids high acceleration voltages and reduces the risk of destroying the Josephson junctions. As the final device was fully functional, we proved that the individual fabrication

steps are not in conflict with each other.
Additionally we precharacterized mechanical string-resonators with an optical interferometer at room temperature. The best resonators have quality factors of 10 000. From results presented in previous work we expect that they increase when cooling the sample to mK temperatures. We calibrated the amplitude of the mechanical motion by analysing the duffing behaviour. We found that by using a piezo actuator the string-resonator can be excited to displacements of 2 nm, which corresponds to 40 000 zero point fluctuations. For future experiments we therefore propose to mount the sample on top of a piezo actuator, which allows excitation of higher amplitudes of the mechanical motion resulting in larger flux changes.
In dc-measurements we characterized the fabricated SQUIDs and successfully reduced the critical current of the Josephson junctions from 4 µA to 1 µA. The dc-measurements have shown that the important parameters of the SQUIDs i.e. β_L and α_I are low and the SQUID therefore should be well suited for an integration into MW resonators resulting in high tunability.
The analysis of superconducting MW resonators by power transmission spectroscopy showed that we can tailor the resonance frequencies without applying extensive numerical simulations and we found out that the best fabricated MW resonators have quality factors of 10 000. For all combinations of mechanical string-resonators and MW resonators with different frequencies the resolved sideband condition ($\Omega_\mathrm{m} > \kappa$) was easily met.
Measurements of MW resonators with embedded SQUIDs however revealed unexpected results. First of all the yield of working FTRs was low. On the final device only the FTR with thickest and shortest SQUID loop wires was flux tunable. Additionally the experimentally observed flux dependence of working FTRs did not match the SQUID parameters obtained in the dc-measurement. The shape as well as the modulation depth of the observed curve was characteristic for small Josephson inductances, i.e. large critical currents. Analysis of the non-linearity of an FTR and comparison of the SQUID inductance on different samples has revealed the same result. We have demonstrated that our theoretic model is correct by applying it to data published in previous work [40] and concluded that the thin string-resonators with dimensions well below the coherence length of superconducting aluminium act as a weak link between MW resonator and ground plane. In literature [84–87] it has been shown that such a weak link can act as Josephson junction and we therefore discussed the possibility that it interferes with the tunnel junctions and possibly dominates the system.
For further sample generations we propose to increase the width of the string-resonators to 200 nm. Although this implies an increase of the mass, hence a decrease of the zero point fluctuation and the vacuum coupling strength, we consider it as the necessary step to maintain the flux tunability of FTRs. Despite the small tuning range of the operational FTR on the final device, it yielded a steep resonator slope of $d\omega_\mathrm{r}/d\Phi = 14.4\,\mathrm{GHz}/\Phi_0$. Together with the results from the characterizations of the individual components we calculated the expected coupling strength for the functional device $g_0/2\pi = 2.9\,\mathrm{kHz}$ ($d\omega_\mathrm{r}/d\Phi = 14.4\,\mathrm{GHz}/\Phi_0$, $B_\mathrm{z} = 1\,\mathrm{mT}$, $l = 15\,\mu\mathrm{m}$, $x_\mathrm{zpf} = 43\,\mathrm{fm}$).
By performing two-tone spectroscopy we aimed to demonstrate that electromechanical interaction is present in our sample. On the blue sideband, where the mechanical motion is amplified by the drive tone, we observed peak like features in the power transmission spectrum of the FTR which are comparable to the theoretic expectation. However they did not occur reproducibly at the

same frequency and did not move with the detuning of the drive tone as expected. Furthermore we performed a frequency sweep of the drive tone in a range of 2 MHz around the perfect detuning and observed an increase in depth and an decrease in linewidth of the resonance dip in the power transmission spectrum of the FTR which could correspond to the phenomenon called "EMIA". The feature occurred at $\Delta \approx 13.8\,\mathrm{MHz}$, where we expected the mechanical resonance. However the feature did not move through the resonance dip of the FTR and was broader than expected. Additionally it was not reproducible in the available measurement time. We sum up that although the measurement data suggests that an electromechanical interaction is present in our sample, reproducible measurements are still pending.
Nevertheless we are confident that with the achievements made in this thesis, strong inductive coupling between flux tunable MW resonators and mechanical string-resonators can be demonstrated with the next generations of samples. As the coupling strength and hence the mechanically induced flux modulation scales with the externally applied magnetic field we suggest for further experiments to change from the out-of-plane direction to the in-plane direction of the SQUID loop. Thus, one can circumvent the limitation of the low critical field of thin film aluminium and increase the fundamental coupling strength as well as the magnetic flux modulation. This will bring along a significant simplification of detection and softens the demanding requirements regarding the flux resolution of the SQUID.

The resulting hybrid device will be usable with outstanding versatility. Due to the switchability of the coupling strength, the coupled string resonator is a candidate for quantum information processing. By switching the coupling off after the state transfer, the quantum mechanical state can exhibit long coherence times due to the high quality of the mechanical motion. Furthermore the device could act as a sensor for vibration in new experimental setups at the frontier of testing the quantum nature of macroscopic objects [9]. It could possibly reach the sensitivity of a quantum limited detector ($S_{\mathrm{xx}}^{1/2} = 20\,\mathrm{fm/Hz}^{1/2}$) [60]. The device is small enough to be integrated directly into the sample chamber of experiments and would allow an in-situ observation of vibrations at the sample position.

Appendix A

Appendix

Standard Fabrication Procedure

Cleaning of new Si wafers

Commercial $6 \times 10\,\mathrm{mm}^2$ Si wafers are coated with a protective layer which has to be removed.

1. Clean the silicon chip twice with aceton at 70 °C in an ultrasonic bath (Martin Walther Ultraschalltechnik: Powersonic) at level 9 for 2 minutes.
2. Rinse the silicon chip with isopropanol
3. Dry the silicon chip with the nitrogen pistol

Gold Deposition

Photoresist spin coating

1. Prebake the silicon chip at 200 °C
2. Clean surface with the nitrogen pistol
3. Deposit two drops of photoresist (AR-P 617.08) from a disposable pipette
4. Run process #10 (2min at 2000rpm) at the spin coater
5. Bake for 10 minutes at 160 °C

Electron beam lithography

We write the pattern into the photoresist using the NanoBeam Limited nB5 Electron Beam Lithography System. The sample is mounted into the sample holder, then the system is controlled remotely with the control software. The layout is defined in a patternfile the exposure dose is defined in a job file. Multiple layers with different exposure doses can be written in one run. For alignment markers and contact pads we use a dose of 6.50.
Please note that one can also control the current of the electron beam by choosing the appropriate

database. Small beam current has better resolution but is slower. For the alignment markers and contact pads we use 10 nA

Development of photresist

After exposure to the electron beam the photoresist is developed in Allresist Ar600-56.

1. 60 s in Ar600-56
2. 120 s in isopropanol at room temperature
3. stop development by rinsing with H_2O
4. dry sample with nitrogen pistol

Evaporation

For evaporation of gold the sample with the evaporation mask on top is mounted into the sample holder. The sample holder is brought into the evaporation chamber. The following parameters are used for evaporation:

1. 4 nm titanium as surfacer at a rate of 1 Å/s without tilt
2. 26 nm gold at a rate of 1 Å/s without tilt

Lift-Off

After evaporation the mask and the excess material needs to be removed. Therefore the photoresist is dissolved in aceton at 70 °C. After 15 min we use a disposable pipette to create flux. The excess material detaches from the sample together with the photoresist.

Aluminium Deposition

Photoresist spin coating

For the aluminium structures we need a double layer resist:

1. Prebake the silicon chip at 200 °C
2. Clean surface with the nitrogen pistol
3. Deposit two drops of photoresist (AR-P 617.08) from a disposable pipette
4. Run process #10 (2min at 2000rpm) at the spin coater
5. Bake for 10 minutes at 160 °C

6. Clean surface with the nitrogen pistol
7. Deposit two drops of photoresist (AR-P 679.02) from a disposable pipette

8. Run process #10 (2min at 2000rpm) at the spin coater

9. Bake for 10 minutes at 160 °C

Electron beam lithography

In the following we give the parameters of the aluminium structures:

1. Transmission line, MW resonators, ground plane and antennas
   dose = 4.95

2. SQUID structure without SQUID arms
   dose = 7.50

3. Undercut for Josephson Junctions
   dose = 1.50

4. Nanomechanical beams including SQUID arms
   dose = 9.00

We use a small beam current of $\approx 2\,\mathrm{nA}$ for josephson junctions and nanomechanical beams and $\approx 10\,\mathrm{nA}$ for the transmission line, MW resonators, ground plane and antennas.

Development of photresist

After exposure to the electron beam the double layer photoresist is developed in Allresist Ar600-56.

1. 45 s in Ar600-56

2. 120 s in isopropanol at 4 °C

3. stop development by rinsing with H_2O

4. dry sample with nitrogen pistol

Evaporation

1. 40 nm aluminium at a rate of 10 Å/s under a tilt of +17°

2. oxidation for 3000 s at valve position 45% and a flow of 5 sccm

3. 70 nm aluminium at a rate of 10 Å/s under a tilt of −17°

Lift-Off

After evaporation the mask and the excess material needs to be removed. Therefore the photoresist is dissolved in aceton at 70 °C. After 15 min we use a disposable pipette to create flux. The excess material detaches from the sample together with the photoresist.

Annealing

To create tensile stress in the mechanical string-resonators the aluminium layer is annealed in an oven at 350 °C for 30 min in vacuum.

Etching process to release the mechanical string-resonators

To release the mechanical string-resonators the sample which is coated by a mask patterned with etching windows is brought into the etching chamber of the reactive ion etching system *Oxford Instruments Plasmalab 80 Plus* (RIE). The sample is etched isotropically with the following parameters:

time	50 min
SF_6 gas flow	50 sccm
chamber pressure	50 mTorr
strike pressure	60 mTorr
DC bias minimum	10 kV
ramp rate	5 V
RF generator forward power	5 W
ICP forward power	0 W

Critical point drying after release of the mechanical string-resonators

After removal of the photresist which has protected the sample during the etching process the sample is dried in the critical point dryer (Leica EM CPD300). Following parameters are used:

	CO_2IN		Exchange		Gas OUT	
Stirring	Speed	Delay	Speed	Cycles	Heat	Speed
off	slow	120 s	1	25	slow	slow 100%

Internal and External Quality-Factors of All MW Resonators

	MWR1	FTR1	FTR2	FTR3	FTR4	MWR2
			$\omega_{\mathrm{r}}/2\pi$ (GHz)			
IM2-4	5.397	6.547	-	7.908	6.581	7.849
IM2-3	5.415	6.545	7.206	7.915	6.528	7.844
IM5-2	3.995	6.750	7.060	7.600	6.405	7.850
			$Q/1000$			
IM2-4	5.44	3.19	-	3.21	2.06	4.92
IM2-3	10.99	10.31	2.33	2.52	3.57	4.31
IM5-2	2.10	4.43	3.64	1.9	2.52	1.65
			$Q_{\mathrm{int}}/1000$			
IM2-4	12.74	9.72	-	14.43	4.81	8.20
IM2-3	15.70	52.7	5.57	2.84	12.63	15.14
IM5-2	3.59	7.01	4.60	2.11	2.99	1.94
			$Q_{\mathrm{ext}}/1000$			
IM2-4	9.50	4.74	-	4.14	3.61	12.32
IM2-3	36.75	12.81	4.01	22.68	4.99	6.01
IM5-2	5.01	12.07	17.48	12.66	16.27	12.31
			$\kappa/2\pi$ (MHz)			
IM2-4	0.99	2.05	-	2.46	3.19	1.59
IM2-3	0.49	0.63	3.09	3.14	1.82	1.82
IM5-2	1.90	1.52	1.94	4.00	2.54	4.76
			$\kappa_{\mathrm{int}}/2\pi$ (MHz)			
IM2-4	0.42	0.67	-	0.55	1.37	0.96
IM2-3	0.35	0.12	1.29	2.79	0.52	0.52
IM5-2	1.11	0.96	1.53	3.60	2.14	4.04
			$\kappa_{\mathrm{ext}}/2\pi$ (MHz)			
IM2-4	0.57	1.38	-	1.91	1.82	0.64
IM2-3	0.15	0.51	1.79	0.35	1.31	1.31
IM5-2	0.79	0.56	0.40	0.60	0.39	0.64

Table A.1: Internal, external and total quality factors and linewidths of all measured resonators on three different samples.

Bibliography

[1] B. P. Abbott, R. Abbott, T. D. Abbott, M. R. Abernathy, F. Acernese, and Ackley (LIGO Scientific Collaboration and Virgo Collaboration), "Observation of Gravitational Waves from a Binary Black Hole Merger", Phys. Rev. Lett. **116**, 061102 (2016).

[2] D. V. Martynov, E. D. Hall, B. P. Abbott, R. Abbott, T. D. Abbott, C. Adams, and Adhikari, "Sensitivity of the Advanced LIGO detectors at the beginning of gravitational wave astronomy", Phys. Rev. D **93**, 112004 (2016).

[3] S. Finkbeiner, *Proceedings of the ESSCIRC, MEMS for automotive and consumer electronics* (2013).

[4] R. Bogue, "Recent developments in MEMS sensors: a review of applications, markets and technologies", Sensor Review **33**, 300 (2013).

[5] A. K. Naik, M. S. Hanay, W. K. Hiebert, X. L. Feng, and M. L. Roukes, "Towards single-molecule nanomechanical mass spectrometry", Nature Nanotechnology **4**, 445 (2009).

[6] J. Chaste, A. Eichler, J. Moser, G. Ceballos, R. Rurali, and A. Bachtold, "A nanomechanical mass sensor with yoctogram resolution", Nature Nanotechnology **7**, 301 (2012).

[7] B. Lassagne, D. Garcia-Sanchez, A. Aguasca, and A. Bachtold, "Ultrasensitive Mass Sensing with a Nanotube Electromechanical Resonator", Nano Letters **8**, 3735 (2008).

[8] M. Cirio, G. K. Brennen, and J. Twamley, "Quantum Magnetomechanics: Ultrahigh-Q-Levitated Mechanical Oscillators", Phys. Rev. Lett. **109**, 147206 (2012).

[9] H. Pino, J. Prat-Camps, K. Sinha, B. P. Venkatesh, and O. Romero-Isart, "On-chip quantum interference of a superconducting microsphere", Quantum Science and Technology **3**, 025001 (2018).

[10] M. Aspelmeyer, T. J. Kippenberg, and F. Marquardt, eds., *Cavity optomechanics* (Springer, Berlin, 2014).

[11] T. J. Kippenberg and K. J. Vahala, "Cavity optomechanics: Back action at the mesoscale", Science **321**, 1172 (2008).

[12] K. J. Vahala, "Optical microcavities", Nature **424**, 839 (2003).

[13] M. Eichenfield, R. Camacho, J. Chan, K. J. Vahala, and O. Painter, "A picogram- and nanometre-scale photonic-crystal optomechanical cavity", Nature **459**, 550 (2009).

[14] J. D. Thompson, B. M. Zwickl, A. M. Jayich, F. Marquardt, S. M. Girvin, and J. G. E. Harris, "Strong dispersive coupling of a high-finesse cavity to a micromechanical membrane", Nature **452**, 72 (2008).

[15] K. R. Brown, J. Britton, R. J. Epstein, J. Chiaverini, D. Leibfried, and D. J. Wineland, "Passive Cooling of a Micromechanical Oscillator with a Resonant Electric Circuit", Phys. Rev. Lett. **99**, 137205 (2007).

[16] C. A. Regal, J. D. Teufel, and K. W. Lehnert, "Measuring nanomechanical motion with a microwave cavity interferometer", Nature Physics **4**, 555 (2008).

[17] A. D. O'Connell, M. Hofheinz, M.and Ansmann, R. C. Bialczak, M. Lenander, E. Lucero, M. Neeley, D. Sank, H. Wang, M. Weides, J. Wenner, J. M. Martinis, and A. N. Cleland, "Quantum ground state and single-phonon control of a mechanical resonator", Nature **464**, 697 (2010).

[18] J. D. Teufel, T. Donner, D. Li, J. W. Harlow, M. S. Allman, K. Cicak, A. J. Sirois, J. D. Whittaker, K. W. Lehnert, and R. W. Simmonds, "Sideband cooling of micromechanical motion to the quantum ground state", Nature **475**, 359 (2011).

[19] E. E. Wollman, C. U. Lei, A. J. Weinstein, J. Suh, A. Kronwald, F. Marquardt, A. A. Clerk, and K. C. Schwab, "Quantum squeezing of motion in a mechanical resonator", Science **349**, 952 (2015).

[20] F. Lecocq, J. B. Clark, R. W. Simmonds, J. Aumentado, and J. D. Teufel, "Quantum Nondemolition Measurement of a Nonclassical State of a Massive Object", Phys. Rev. X **5**, 041037 (2015).

[21] J.-M. Pirkkalainen, E. Damskägg, M. Brandt, F. Massel, and M. A. Sillanpää, "Squeezing of Quantum Noise of Motion in a Micromechanical Resonator", Phys. Rev. Lett. **115**, 243601 (2015).

[22] J. D. Teufel, T. Donner, M. A. Castellanos-Beltran, J. W. Harlow, and K. W. Lehnert, "Nanomechanical motion measured with an imprecision below that at the standard quantum limit", Nature Nanotechnology **4**, 820 (2009).

[23] J. Bochmann, A. Vainsencher, D. D. Awschalom, and A. N. Cleland, "Nanomechanical coupling between microwave and optical photons", Nature Physics **9**, 712 (2013).

[24] R. W. Andrews, R. W. Peterson, T. P. Purdy, K. Cicak, R. W. Simmonds, C. A. Regal, and K. W. Lehnert, "Bidirectional and efficient conversion between microwave and optical light", Nature Physics **10**, 321 (2014).

[25] T. A. Palomaki, J. W. Harlow, J. D. Teufel, R. W. Simmonds, and K. W. Lehnert, "Coherent state transfer between itinerant microwave fields and a mechanical oscillator", Nature **495**, 210 (2013).

[26] A. P. Reed, K. H. Mayer, J. D. Teufel, L. D. Burkhart, W. Pfaff, M. Reagor, L. Sletten, X. Ma, R. J. Schoelkopf, E. Knill, and K. W. Lehnert, "Faithful conversion of propagating quantum information to mechanical motion", Nature Physics **13**, 1163 (2017).

[27] P. D. Nation, M. P. Blencowe, and E. Buks, "Quantum analysis of a nonlinear microwave cavity-embedded dc SQUID displacement detector", Physic Review B **78**, 104516 (2008).

[28] O. Shevchuk, G. A. Steele, and Y. M. Blanter, "Strong and tunable couplings in flux-mediated optomechanics", Phys. Rev. B **96**, 014508 (2017).

[29] P. D. Nation, J. Suh, and M. P. Blencowe, "Ultrastrong optomechanics incorporating the dynamical Casimir effect", Phys. Rev. A **93**, 022510 (2016).

[30] S. Etaki, M. Poot, I. Mahboob, K. Onomitsu, H. Yamaguchi, and H. S. J. van der Zant, "Motion detection of a micromechanical resonator embedded in a d.c. SQUID", Nature Physics **4**, 785 (2008).

[31] S. Etaki, F. Konschelle, Y. M. Blanter, H. Yamaguchi, and H. S. J. van der Zant, "Self-sustained oscillations of a torsional SQUID resonator induced by Lorentz-force back-action", Nature Communications **4**, 1803 (2013).

[32] W. Weaver, S. P. Timoshenko, and D. H. Young, *Vibration Problems in Engineering* (John Wiley & Sons, Hoboken, NJ, 1990).

[33] A. N. Cleland, *Foundations of Nanomechanics* (Springer, Berlin, 2002).

[34] R. Hollaender, "Magnetostriction in nanomechanical beams", Master's thesis, Technische Universität München, Walther-Meißner Institut, Garching (2014).

[35] M. Pernpeintner, R. B. Holländer, M. J. Seitner, E. M. Weig, R. Gross, S. T. B. Goennenwein, and H. Huebl, "A versatile platform for magnetostriction measurements in thin films", Journal of Applied Physics **119**, 093901 (2016).

[36] W. Demtröder, *Experimentalphysik 1* (Springer, 2018).

[37] D. Meschde, *Gerthsen Physik* (Springer, 2015).

[38] D. J. Griffiths, *Introduction to Quantum Mechanics*, 2nd Edition (Pearson Prentice Hall, 2004), 2nd ed., ISBN 0131118927,9780131118928.

[39] A. Nayfeh and D. T. Mook, *Nonlinear Oscillations* (Wiley-VCH, Weinheim, 1995).

[40] P. Schmidt, "Inductive switchable cavity electromechanics", Master's thesis, Technische Universität München, Walther-Meißner Institut, Garching (2015).

[41] M. Pernpeintner, "Nanomechanical Hybrid Systems", Ph.D. thesis, Technische Universität München, Walther-Meißner Institut, Garching (2016).

[42] M. Göppl, A. Fragner, M. Baur, R. Bianchetti, S. Filipp, J. M. Fink, P. J. Leek, G. Puebla, L. Steffen, and A. Wallraff, "Coplanar waveguide resonators for circuit quantum electrodynamics", Journal of Applied Physics **104**, 113904 (2008).

[43] J. Goetz, F. Deppe, M. Haeberlein, F. Wulschner, C. W. Zollitsch, S. Meier, M. Fischer, P. Eder, E. Xie, K. G. Fedorov, E. P. Menzel, A. Marx, and R. Gross, "Loss mechanisms in superconducting thin film microwave resonators", Journal of Applied Physics **119**, 015304 (2016).

[44] F. Hocke, "Microwave circuit-electromechanics in a nanomechanical hybrid system", Ph.D. thesis, Technische Universität München, Walther-Meißner Institut, Garching (2013).

[45] B. S. Deaver and W. M. Fairbank, "Experimental Evidence for Quantized Flux in Superconducting Cylinders", Phys. Rev. Lett. **7**, 43 (1961).

[46] R. Doll and M. Näbauer, "Experimental Proof of Magnetic Flux Quantization in a Superconducting Ring", Phys. Rev. Lett. **7**, 51 (1961).

[47] R. Gross, "Applied superconductivity", lecture notes, Walther-Meißner-Institut, Gaching, (2013).

[48] J. Clarke and A. I. Braginski, eds., *The SQUID Handbook* (Wiley-VCH, Weinheim, 2006).

[49] A. J. Annunziata, D. F. Santavicca, L. Frunzio, G. Catelani, M. J. Rooks, A. Frydman, and D. E. Prober, "Tunable superconducting nanoinductors", Nanotechnology **21**, 445202 (2010).

[50] M. Schwarz, "Gradiometric tunable-gap flux qubits in a circuit QED architecture", Ph.D. thesis, Technische Universität München (2014).

[51] C. Girardi, URL `http://www.qsl.net/in3otd/ind2calc.html`.

[52] F. Terman, *Radio Engineers' Handbook* (McGraw-Hill Book Company, 1943).

[53] S. Pogorzalek, K. G. Fedorov, L. Zhong, J. Goetz, F. Wulschner, M. Fischer, P. Eder, E. Xie, K. Inomata, T. Yamamoto, Y. Nakamura, A. Marx, F. Deppe, and R. Gross, "Hysteretic Flux Response and Nondegenerate Gain of Flux-Driven Josephson Parametric Amplifiers", Phys. Rev. Applied **8**, 024012 (2017).

[54] M. Wallquist, V. S. Shumeiko, and G. Wendin, "Selective coupling of superconducting charge qubits mediated by a tunable stripline cavity", Phys. Rev. B **74**, 224506 (2006).

[55] M. Sandberg, C. M. Wilson, F. Persson, T. Bauch, G. Johansson, V. Shumeiko, T. Duty, and P. Delsing, "Tuning the field in a microwave resonator faster than the photon lifetime", Applied Physics Letters **92**, 203501 (2008).

[56] J. R. Johansson, G. Johansson, C. M. Wilson, and F. Nori, "Dynamical Casimir Effect in a Superconducting Coplanar Waveguide", Phys. Rev. Lett. **103**, 147003 (2009).

[57] T. Cao, *Conceptual Foundations of Quantum Field Theory* (Cambridge University Press, 2004).

[58] C. M. Wilson, G. Johansson, A. Pourkabirian, M. Simoen, J. R. Johansson, T. Duty, F. Nori, and P. Delsing, "Observation of the dynamical Casimir effect in a superconducting circuit", Nature **479**, 376 (2011).

[59] J. B. Clark, F. Lecocq, R. W. Simmonds, J. Aumentado, and J. D. Teufel, "Observation of strong radiation pressure forces from squeezed light on a mechanical oscillator", Nature Physics **12**, 683 (2016).

[60] M. Aspelmeyer, T. J. Kippenberg, and F. Marquardt, "Cavity optomechanics", Reviews of Modern Physics **86**, 1391 (2014).

[61] M. L. Gorodetksy, A. Schliesser, G. Anetsberger, S. Deleglise, and T. J. Kippenberg, "Determination of the vacuum optomechanical coupling rate using frequency noise calibration", Opt. Express **18**, 23236 (2010).

[62] F. Hocke, X. Zhou, A. Schliesser, T. J. Kippenberg, H. Huebl, and R. Gross, "Electromechanically induced absorption in a circuit nano-electromechanical system", New Journal of Physics **14**, 123037 (2012).

[63] I. Mahboob, K. Nishiguchi, A. Fujiwara, and H. Yamaguchi, "Phonon Lasing in an Electromechanical Resonator", Phys. Rev. Lett. **110**, 127202 (2013).

[64] P. Natzkin, "Superconducting Microwave Resonator Designs for Electron Spin Resonance Applications", Master's thesis, Technische Universität München, Walther-Meißner Institut, Garching (2017).

[65] D. Schwienbacher, "Circuit nano-electromechanics transmon qubits, nano-strings and resonators", Master's thesis, Technische Universität München, Walther-Meißner Institut, Garching (2016).

[66] W. Demtröder, *Experimentalphysik 2* (Springer, 2013).

[67] M. Mück, J. B. Kycia, and J. Clarke, "Superconducting quantum interference device as a near-quantum-limited amplifier at 0.5 GHz", Applied Physics Letters **78**, 967 (2001).

[68] R. H. Koch, D. J. V. Harlingen, and J. Clarke, "Quantum noise theory for the dc SQUID", Applied Physics Letters **38**, 380 (1981).

[69] C. D. Tesche and J. Clarket, "dc SQUID: Current noise", Journal of Low Temperature Physics **37**, 397 (1979).

[70] A. M. Cesidio Bianchi, "Natural and man-made terrestrial electromagnetic noise: an outlook", Annals of Geophysics (2007).

[71] A. Megrant, C. Neill, R. Barends, B. Chiaro, Y. Chen, L. Feigl, J. Kelly, E. Lucero, P. Mariantoni, M. O'Malley, D. Sank, A. Vainsencher, J. Wenner, and A. Cleland, "Planar superconducting resonators with internal quality factors above one million", Applied Physics Letters **100**, 113510 (2012).

[72] P. Schmidt, "Measuring resonator photon numbers: Transmon qubits vs. nanomechanical resonators", in preparation (2018).

[73] F. Sterr, "Optimization of Josephson Junction Nanofabrication for Superconducting Quantum Circuits", Master's thesis, Technische Universität München, Walther-Meißner Institut, Garching (2013).

[74] E. Xie, "Optimized fabrication process for nanoscale Josephson junctions used in superconducting quantum circuits", Master's thesis, Technische Universität München, Walther-Meißner Institut, Garching (2013).

[75] H. Namatsu, K. Yamazaki, and K. Kurihara, "Supercritical drying for nanostructure fabrication without pattern collapse", Microelectronic Engineering **46**, 129 (1999).

[76] G. L. Weibel and C. K. Ober, "An overview of supercritical CO2 applications in microelectronics processing", Microelectronic Engineering **65**, 145 (2003).

[77] R. Gross, "Low temperature physics 2", lecture notes, Walter Meißner Institut, Gaching, (2013).

[78] A. Sinha and T. Sheng, "The temperature dependence of stresses in aluminum films on oxidized silicon substrates", Thin Solid Films **48**, 117 (1978).

[79] R. J. Corruccini and J. J. Gniewek, *Thermal Expansion of Technical Solids at Low Temperatures: A Compilation From the Literature* (United States Government Printing Office, 1961).

[80] C. Kittel, *Introduction to Solid State Physics* (Wiley, 2004).

[81] Aluminiumoxid, material properties, URL `https://mhf-e-wiki.desy.de/Al2O3_Aluminiumoxid`.

[82] V. Semiconductors, Tech. Rep., Virginia Semiconductors, http://www.virginiasemi.com/pdf/generalpropertiesSi62002.pdf (2002).

[83] R. Gross and A. Marx, *Festkörperphysik* (Oldenbourg Wissenschaftsverlag, München, 2012).

[84] K. K. Likharev, "Superconducting weak links", Rev. Mod. Phys. **51**, 101 (1979).

[85] P. W. Anderson and A. H. Dayem, "Radio-Frequency Effects in Superconducting Thin Film Bridges", Phys. Rev. Lett. **13**, 195 (1964).

[86] C. Granata and A. Vettoliere, "Nano Superconducting Quantum Interference device: A powerful tool for nanoscale investigations", Physics Reports **614**, 1 (2016).

[87] S. Benacka, L. Bezakova, S. Gazi, S. Takacs, and J. Palaj, "Properties of long superconducting variable thickness bridges", Czechoslovak Journal of Physics B **28**, 192 (1978).

[88] M. M. Özer, J. R. Thompson, and H. H. Weitering, "Hard superconductivity of a soft metal in the quantum regime", Nature Physics **2**, 173 (2006).

[89] C. Besson, "Quantum Simulations of Many-Body Systems with Superconducting Devices", Master's thesis, Technische Universität München, Walther-Meißner Institut, Garching (2018).

Acknowledgement

I would like to thank numerous people for the great support during my year at the WMI:

First of all I would like to thank my friend Philip Schmidt for advising me and helping with all kinds of problems. Thank you for your support, your patience in every situation and of course your strong motivation to push this project forward. You showed me that putting extra effort into something always pays off, in one way or an other. I wish you all the best for future samples and a successful PhD project.

Further I would like to thank all the people who contributed to this project and supported me:

- Prof. R. Gross for giving me the opportunity to write my thesis at the Walther-Meißner-Institut.
- Hans Hübl for letting me work in your group, for your support and for all the inspiring discussions and explanations. You found a good path between supervising my work and giving me the opportunity to work on my own, developing my own ideas and to find my own solutions.
- Stefan Pogorzalek for your helpful ideas regarding the tunability of JPAs.
- Christian Besson for helping me to understand the duffing behaviour of MW resonators and for adapting your Mathematica file to my needs.
- Daniel Schwienbacher for providing fruitful ideas and especially for helping me with problems at the NanoBeam.
- My office colleagues Lisa Rosenzweig, Daniel Arweiler and Florian Löffler for bringing life, fun and cake into our office.
- Thomas Brenninger and all the technical staff at the WMI for their outstanding efforts to keep all the instruments running despite the construction works during the last year.
- All the students and employees at the WMI who created a very enjoyable atmosphere.

I also would like to thank my family for their support during my entire studies. Sabine, thank you for helping me with difficult integrals and motivating me whenever I came up with confusing problems.

Last but not least I would like to thank my girlfriend Anna for giving me a hug when I needed one and being always there for me.

Thanks a lot to everyone!

Eidesstattliche Erklärung

Hiermit erkläre ich, dass ich die vorliegende Arbeit eigenständig und ohne fremde Hilfe angefertigt habe. Textpassagen, die wörtlich oder dem Sinn nach auf Publikationen oder Vorträgen anderer Autoren beruhen, sind als solche gekennzeichnet.

Christoph Utschick
München, den April 10, 2018